JGERI
Journal of Green Energy
Research and Innovation
ISSN: 3041-9018

Journal of Green Energy Research and Innovation

Volume 3, Issue 1, Winter 2026

PUBLISHER
Arak University

Journal of Green Energy Research and Innovation (JGERI)

Publisher: **Arak University**

Director-in-Charge: **Dr. Ali Asghar Ghadimi**

Editor-in-Chief: **Prof. Gevork B. Gharehpetian**

Deputy Editor: **Dr. Abolghasem Daeichian**

Managing and Executive Editor**: Dr. Mahyar Abasi**

Coverage area: **International**

Journal Type: **Scientific and technical**

Scientific Rank (Iran MSRT): **B**

Language: **English**

Frequency: **Quarterly**

Review Time: **4-8 Weeks**

Publication Type: **Electronic**

Open Access: **Yes**

Licensed by: **CC BY-NC 4.0**

Policy: **Peer-Reviewed**

DOI**: 10.61186/jgeri**

E-mails: **jgeri@araku.ac.ir**

Website: **https://jgeri.araku.ac.ir/**

Address: **Department of Electrical Engineering, Faculty of Engineering, Arak University, Arak, Iran.**

P.O. Box: **38156-8-8349**

Tel: **086-32625099**

Editorial Board

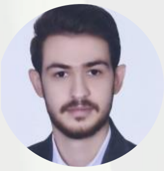

About Journal

JGERI is an international, open-access, and free-of-charge journal in the field of green and renewable energies, published quarterly, only electronically, in cooperation with the Renewable Energy Research Institute (**RERI**) of Arak University and Iranian Association of Electrical and Electronics Engineers (**IAEEE**). Articles accepted and published by **JGERI** are in three formats: research articles, review articles, and applied articles. **JGERI** accepts manuscripts that provide results of scientific achievements in a very wide scope of fundamental, engineering, and industrial research focusing on green energy.

The following articles are acceptable:

- **Research articles** are expected to present innovative solutions, new concepts, or creative ideas that can help solve existing or emerging technical challenges in the field of green and renewable energy.
- **Review articles** are expected to provide enlightening and specialized reviews, trainings, or case studies on an important topic, timely and widely in the field of green and renewable energies.
- **Applied articles** are expected to share the results of the industry's valuable experiences in dealing with challenging technical issues, developing/adopting new standards, applying new technologies or solving complex problems in the field of green and renewable energies. These articles can have a significant impact on the strategic plans of the industry in the coming years.

Aims and Scope

JGERI is interested on the qualified international multidisciplinary research results related to all aspects of green energy. The scope of **JGERI** is very broad, and welcomes original, novel fundamental and engineering research. We also publish reviews and industrial reports of green energy and its impact on the eco-environment.

We welcome research papers that focus on, but are not limited to, the following areas:

- Policies and Strategies for Green Energy Systems
- Fundamental And Industrial Applications for Green Energy Systems
- Energy Conversion, Control Techniques, and Grid Interactive Systems for Green Energy Systems
- Environmental Impacts of Energy Technologies and Pollution Control
- Materials And Catalysis for Green Energy Systems
- Green Energy Consumption
- Artificial Intelligence, Machine Learning, and Computational Methods in Green Energy Systems
- Public Awareness and Education for Green Energy Systems
- Solar Energy and Photovoltaic
- Wind Energy
- Hydrogen Energy and Energy Storage
- Biofuel and Bioenergy
- Utilization of Green Energies in the Structure of Power Systems
- Development of Manufacturing Technology for Green Energy Production Tools
- Electricity Market in the Presence of Green Energies
- The Effects of Green Energy Production on Power Quality of the Power System
- Impact of Expansion Planning of Power Systems on the Development of Green Energy Generation
- Operation of Green Energy-Based Microgrids
- Control and Protection of Power Systems in Networks Equipped with Green and Renewable Generation
- Energy Management in Networks Consisting of Green Energies
- Studies on the Technology of Hybrid Vehicles Based on Green Energy Fuels
- The Future Perspective of the Electricity Industry in the Presence of Production-Based Technologies and Green Energy-Based Consumers
- Green Energy Storage Technologies
- Communication Infrastructures and Protocols and Internet in Green Energy-Based Power Systems
- Cyber Security and Defense Activities in the Field of Green Energy Management

Each manuscript will go through a rigors peer-review process. you can visit our Guide for Authors page for information on preparing your manuscript.

Guide for Authors

1. Important points and rules for manuscript submission and publication

-Submitting a manuscript to a journal means that the manuscript is not under review or has not been published anywhere in any other language before.
-The submission of the manuscript for publication by the author, implicitly or explicitly, implies the approval of the organization or body where the author works and has used its affiliation.
-By submitting the manuscript, all authors officially declare their agreement to grant the copyright of the manuscript in case of acceptance to Arak University and **JGERI**. However, the authors are responsible for all the contents published in the manuscript, and the journal is only a reviewer and publisher.
- All authors are required to declare any actual or potential conflicts of interest, including financial, personal, or relationships with individuals or organizations that could affect their work.
- Each of the authors must declare their contribution and role in the manuscript on the Title Page to the journal. The statement of approval of all authors and their role in the manuscript is the responsibility of the corresponding author.
- Authors should note that all manuscripts sent to **JGERI** are checked with Authenticate's CrossCheck software to analyze the authenticity of the content. In this analysis, the overlap and similar texts presented in the submitted manuscripts will be determined.
- **JGERI** makes its manuscripts open to access after publication and there is no charge (APC) for reviewing and publication of manuscripts, and readers can download and use the articles for free.
- All authors, if they had financial support in conducting research related to this manuscript, should briefly state their role. If financial source(s) have no role in the results of the research published by the article, this should also be mentioned by the authors.
- Acknowledgments to individuals and institutions can be mentioned in a separate section at the end of the manuscript before References, and they must not be included as footnotes or in any other form. In this section, it is recommended to mention the names of those who have collaborated during the research (such as those helping in the language correctness aspect of the manuscript, assisting in writing the manuscript or proofreading it, and other cases).
- Non-commercial use of the manuscript will be governed by the Creative Commons Attribution-NonCommercial 4.0 International License, which is currently available at the link (https://creativecommons.org/licenses/by-nc/4.0/). This certificate allows others to use the authors' work in a non-commercial way and utilize it in their research work, although in the new work, they need to acknowledge the authors and mention its non-commercial nature.

2. Initial submission of the manuscript

Submission to this journal is online and you will be accompanied in all the steps of creating a user account and uploading files. All correspondence, including notification of the editor's decision and request for revision, will be made via email. To submit your manuscript, just click on the **Submit Manuscript** option on the journal page. Then, click on **Register** to create an author account. A message will be sent to your email containing your username and password. Then, log in to the manuscript submission system on the Users login page, where you need to enter the username and password and submit your new manuscript. Once you are logged in, you can change your password by clicking on My Home in the top menu. For the next time, just log in to your account. Please include the names, addresses, and email addresses of at least three potential academic reviewers with the paper. Please include reviewers' names and their academic rank, affiliation, and contact information (mail address is mandatory). However, only the editor has the right to decide on the use of suggested reviewers. All the submitted manuscripts undergo the process of plagiarism check with IThenticate software and the review process begins. According to the journal policy, there is a difference between the requirements for initial and revised submission files. Required files for initial submission include three files: **JGERI_Main_Manuscript**, **JGERI_Form_for _Copyright_Transfer_Statement and Conflict_ of_ Interest_ Disclosure** and **JGERI_Cover_Letter**, all three of which must be sent to the journal in PDF format. You can use the links below to download the requirements and suggestions files of these three files.

- JGERI_Guideline_for_Main_Manuscript
- JGERI_Guideline_for_Cover_Letter
- JGERI_Form_for_Copyright_Transfer_Statement and Conflict_ of_ Interest_ Disclosure

3. Submission of the revised manuscript

If the submitted manuscript, after going through the initial review process, is evaluated by the officials and reviewers of the journal and a decision is made to make corrections and revisions in the form of minor or major, the authors are obliged to make the corrections and prepare the response letter to the reviewers within the time specified by the journal. Three files must be sent to the journal at this stage: WORD and PDF files of the revised manuscript (changes should be highlighted), PDF file of the response to the reviewers (including the comments and responses of each of the reviewers separately), Title Page and Authorship file in WORD format (containing two main forms: Title Page and Authorship). The link to download the necessary files along with their requirements and instructions is given below. Points raised in the file **JGERI_Revised_Manuscript** must be followed for compiling the revised manuscript. The authors are obliged to submit the revised file in PDF and WORD format to the journal. Also, different parts of the file **JGERI_Form_for_Title_Page_ and_ Authorship** needs to be completed and signed by the corresponding author, but **JGERI_Response_to_the_Reviewers_Comments** is suggested by the journal and it is not necessary to follow all the points of that file. It should be noted that all the stages of page layout and editing in the form of final publication are the responsibility of the journal. In the completion stages of this process, the cooperation of the authors is needed, and we will inform you at each stage. Thus, the minimum requirements for file compilation are provided in the template file.

- JGERI_Guideline_for_Revised_Manuscript
- JGERI_Form_for_Title_Page_ and_ Authorship
- JGERI_Guideline_for_Response_to_the_Reviewers_Comments

4. After the final acceptance of the manuscript

After announcing the final acceptance of the manuscript (reviews may happen several times), the files **JGERI_Revised_Manuscript** and **JGERI_Form_for_ Title_Page_ and_ Authorship** will be sent to the paging unit for page layout and final editing. After the final acceptance announcement, the authors will be asked to send a graphic abstract included in a single file. Then, the process of compilation of the manuscript will be completed by the journal and finally, the proof version of the manuscript will be sent to the authors. The authors are obliged to check the proof file completely and report to the journal if they find any ambiguity or error in the final file. In some cases, along with the final proof file of the manuscript, there may be a series of errors and ambiguities in the manuscript, which are sent to the author in the form of comments along with the proof version of the manuscript. The corresponding author is obliged to clarify and resolve these problems and ambiguities in the specified time.

5. After publication on the journal's website

After announcing the initial acceptance, the information of the article without its content will be indexed in the Articles in the Press section of the website. After including the article in the issue selected by the journal, the desired article will be indexed in the Current Issue unit along with Vol., No., and pp. Also, the electronic file of the article can be introduced in all scientific references through the DOI link. The important point is that, after acceptance and indexing, the names of the authors cannot be changed, that is, it will not be possible to add, delete, or change the order of the names of the authors and their organizational affiliations.

Cooperative Publication Organization

Renewable Energy Research Institute of Arak University
http://araku.ac.ir/web/riren

Iranian Association of Electrical and Electronics Engineers
https://iaeee.ir/

Iranian Wind Energy Association
https://www.irwea.org/fa/

Indexing Databases and Social Networks

Iran MSRT: https://journals.msrt.ir/home/detail/21538/

Magiran: https://www.magiran.com/magazine/8484

Google Scholar: https://scholar.google.com/citations?user=47bsJFoAAAAJ&hl=en

Linkedin: https://www.linkedin.com/in/jgeri-arak-university-0818872b9

Academia:https://independent.academia.edu/JournalofGreenEnergyResearchandInnovationJGERI

MyScineceWork: https://www.mysciencework.com/profile/j.green.energy.res.innov.jgeri

Contents

Article Title and Authors **Page No.**

Journal of
Green Energy
Research and Innovation

Investigating the Impact of Soil Models on GPR in Wind Turbines Grounding Systems Across Various Geographical Regions

Omid Heydari , Hassan Moradi, Shahram Karimi, Hamdi Abdi

Highlights

- **Regional Dependence: GPR spikes in high-resistivity soils (desert, frozen) but remains low in water-saturated coastal areas.**
- **Model Efficiency: Multi-layer soil models drastically reduce predicted GPR in harsh regions (~63.5%) but offer minimal gains in coastal zones (~13.5%).**
- **Critical Reduction: In frozen terrain, realistic three-layer modeling cut peak GPR from ~2.2 MV to ~0.8 MV compared to uniform assumptions.**
- **Key Takeaway: Effective wind turbine grounding demands region-specific soil data rather than generic uniform models.**

Graphical Abstract

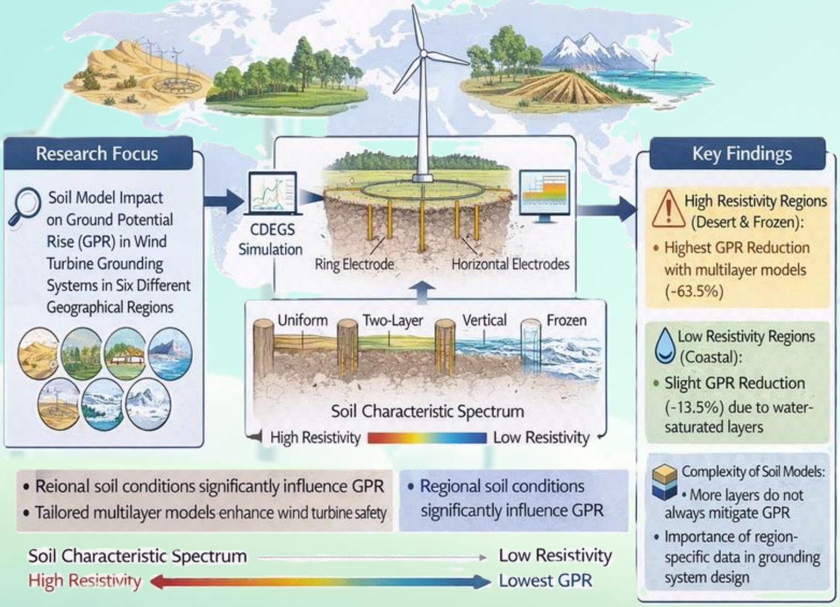

Use your device to scan and read the article online

Citation
O. Heydari, H. Moradi, S. Karimi, and H. Abdi, "Investigating the Impact of Soil Models on GPR in Wind Turbine Grounding Systems Across Various Geographical Regions," *Journal of Green Energy Research and Innovation*, vol. 3, no. 1, pp. 1-15, 2026.

https://doi.org/10.61882/jgeri.3.1.1

Online ISSN: 3041-9018

Journal of Green Energy Research and Innovation

Journal Homepage: www.jgeri.araku.ac.ir

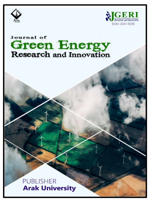

Investigating the Impact of Soil Models on GPR in Wind Turbines Grounding Systems Across Various Geographical Regions

Omid Heydari , Hassan Moradi [*] , Shahram Karimi , Hamdi Abdi

Department of Electrical Engineering, Faculty of Engineering, Razi University, Kermanshah, 6714414971, Iran

ARTICLE INFO

Keywords:
Wind turbine Grounding System,
Soil modeling,
Lightning CDEGS software,
Geographical areas.

Article History:
Received: 18 July 2025;
Revised: 14 August 2025;
Accepted: 31 August 2025.

Article type:
Research Article

* ***Corresponding authors***
E-mail address
ha.moradi@razi.ac.ir (H. Moradi)

ABSTRACT

Grounding systems in wind turbines are critical for lightning protection and managing GPR. This study investigates the influence of different soil models (uniform, two-layer, and three-layer) on GPR across six distinct geographical regions: desert, forest, agricultural, mountainous, coastal, and frozen. Simulations were performed using the CDEGS software on a standard grounding system comprising a ring electrode, horizontal electrodes, and vertical electrodes. The results reveal a strong dependence of GPR on soil characteristics and regional conditions. In desert regions, the high resistivity of dry soil significantly increases GPR, whereas in coastal areas, water-saturated layers markedly reduce GPR. In frozen regions, surface layer freezing substantially elevates GPR despite lower resistivity in deeper layers. The study demonstrates that increasing the complexity of the soil model (i.e., the number of layers) does not necessarily mitigate GPR, underscoring the need for region-specific data in grounding system design. Numerical results show the largest peak GPR for the uniform model in the frozen region during winter ($\approx$2,197,587 V), reduced to 802,833.2 V with the three-layer model ($\approx$63.5% reduction). Overall, in high-resistivity regions (desert, mountainous, frozen), multilayer models yield substantial GPR reductions, whereas in coastal areas, changes in the soil model cause only minor decreases ($\approx$13.5%). These findings highlight the importance of tailoring grounding system designs to geographical conditions, potentially enhancing the safety and efficiency of wind turbines against lightning strikes.

1. Introduction

Wind turbines, as a major source of large-scale renewable energy, are installed across a wide range of geographic environments from deserts and mountainous regions to coastal, agricultural, and frozen areas. Lightning strikes can induce substantial GPR (Ground Potential Rise), contact voltages, and step voltages, adversely affecting sensitive electrical equipment and personnel safety. Therefore, mitigation of GPR and optimization of the earthing network are critical practical issues for wind farm reliability.

Numerous studies have shown that soil resistivity and its layered profile strongly influence transient earth impedance and peak GPR; assuming homogeneous soil can lead to inaccurate estimates and suboptimal designs [1,2]. Accurate characterization of soil and attention to layered profiles are therefore essential for reliable prediction of surface potentials and voltages [1,3].

Several studies have shown that soil electrical properties and their possible frequency dependence can influence transient responses and peak GPR values [1,3]. Djaborebbi et al. employed transient approaches such as TLM and highlighted the importance of accurate simulation methods for representing transient current distribution and potentials [4]. Visacro et al. pointed out that certain soil electrical characteristics can affect transient analyses; these findings suggest that accounting for soil properties is useful when comparing regions with different resistivities [5]. Field measurements and numerical analyses indicate that multilayer soil models (two- or three-layer horizontal profiles) significantly improve the prediction of overall earth resistance and contact/step voltages compared to uniform models, particularly when surface and sub-surface layers differ in resistivity.

Common practice combines Wenner resistivity measurements and inversion/optimization methods (e.g., Sunde formula + genetic algorithms) to extract realistic layered profiles for simulation [3,6]. Transient GPR analysis commonly employs industry-grade packages such as CDEGS/SES, combined with numerical solvers (FEM/PEEC—COMSOL, XGSLab) and ATP/EMTP or PSCAD for system transient interaction. The combination of field data and accurate numerical modeling is the accepted approach for robust earthing design [7,8].

Recent research on energy management and smart distribution networks, including Virtual Power Plants (VPPs), Electric Springs (ES), and demand response programs, has demonstrated that coordinated resource-and-load management can substantially improve network performance indices (voltage profile, losses, flexibility, and reliability). Although these works do not directly address earthing design, their system-level approach supports the use of realistic soil models and regional analysis for infrastructure and protection decisions [9-11].

Wang et al. have shown that techno-economic co-design of local storage systems (including hydrogen storage) and smart EV charging can substantially affect off-grid planning outcomes; these results underline the importance of incorporating local site characteristics (including soil properties) into engineering analyses when assessing equipment safety and operational performance [12].

Oboudi et al. demonstrate that reliability-constrained transmission expansion planning with simultaneous load and renewable forecasting can improve operational and reliability indices; these findings emphasize the need to couple system-level planning studies with accurate local site modeling (e.g., GPR estimation using realistic soil profiles) [13].

Zadehbagheri et al., focusing on resiliency under extreme weather events, show that optimal placement and sizing of Virtual Power Plants can enhance network resilience; such resiliency-driven planning suggests that higher-level strategies should also account for site-level protections and designs (including grounding and GPR considerations at critical sites) [14].

Naghibi et al. demonstrate that optimal sizing and siting of integrated renewable energy systems (including hydrogen technologies) can significantly improve distribution network technical indices; these outcomes reinforce the need to consider the interaction between system-level planning and local physical parameters (such as soil conditions and resulting GPR effects) [15].

Table 1 summarizes the most relevant studies in the field of wind turbine grounding systems and similar infrastructures, comparing them in terms of study type, soil modeling approach, simulation tools, and geographical coverage. The comparison highlights that the present study adopts a systematic, multi-regional evaluation of soil models (uniform, two-layer, and three-layer), which has been rarely addressed comprehensively in previous works.

Table 1. Comparison of previous works with the present study based on application domain, soil modeling approach, and analysis scope.

No.	Reference	Year	Main focus/method	Scope/example geographic coverage	Main limitation	How current work differs/advantages
1	[1] Alipio et al.	2020	Transient response and low-frequency performance analysis of wind farm earthing	Case studies on wind farms	Often limited to single or few turbines; focus on waveforms and frequency dependence	We perform a systematic 1L/2L/3L comparison across six geographic regions with fixed electrode geometry and waveform to isolate the soil effect.
2	[6] Alipio et al.	2021	GPR due to direct lightning; emphasis on frequency-dependent parameters	Wind farm cases	Emphasis on frequency dependence and waveform analysis; limited regional comparison	Our study focuses on soil profile impacts across regions, complementing waveform-focused analyses.
3	[5] Alipio et al.	2019	Effect of frequency-dependent soil parameters on lightning response	General	Focus on frequency-dependent modeling (high complexity)	We compare 1L/2L/3L models while controlling other variables to highlight layering effects.
4	[4] Djaborebbi et al.	2021	Transient modeling (TLM) of earthing system response	Numerical studies	Focus on numerical method; limited multi-region coverage	The present work uses CDEGS with regional profiles and a multi-region comparison.
5	[3] Sabiha & Elkalashy	2018	Field Wenner measurements + Sunde inversion + genetic algorithm for profile extraction	Field case study	Site-specific study; no broad geographic comparison	We adopt similar profile extraction methods but apply them to six regions and run CDEGS simulations for each.
6	[7] CDEGS documentation	2023	Industrial-grade modeling of layered soils and earthing systems	Global/industrial	Powerful tool, but requires field data for validation	We use CDEGS as our main simulation platform and feed it with regional soil profiles to enhance the validity.
7	[9] Yao et al.	2023	Energy management: VPP & Electric Springs in SDN	Distribution network (IEEE-69 example)	Focus on energy management/operational metrics rather than earthing design	These references demonstrate system-level methods; we cite them to justify the need for realistic soil models and system-aware analysis.
8	[12] Wang et al.	2025	Stochastic sizing/optimization for hydrogen-based systems (future directions)	Example planning studies in the literature	Focus on planning/optimization; different domain but related methodology	We cite these works in limitations/future work to motivate resilience and H2-integration extensions.
9	[14], [15]	2024–2025	VPPs, resilience, and integrated-energy planning	Distribution / active DN	Emphasis on resilience/planning	These provide pathways for future expansions discussed in "Dedicated Limitations".

Despite substantial existing work, important gaps remain: (i) a lack of systematic, comparative studies of single-, two-, and three-layer soil models across multiple geographic regions; and (ii) limited guidance for engineers on where multilayer modeling is practically necessary. The present study addresses these gaps by providing a systematic comparison across six distinct geographic types [1,6].

The objective of this study is to systematically investigate the effect of three soil models (1L/2L/3L) on GPR in six geographical regions.

Its innovation can be the systematic comparison of 1L/2L/3L in six regions and pure focus on soil effect while keeping electrode geometry and lightning surge as fixed parameters.

Simulations were also performed using CDEGS software modules and considering fixed geometric parameters (R = 15 m ring, 1 m burial, four horizontal 20 m, and four vertical 10 m).

Figure 1 illustrates the overall framework of the present study in graphical abstract form, comprising six geographic regions (desert, forest, agricultural, mountainous, coastal, and frozen), three soil models (uniform, two-layer, and three-layer), and simulations performed using the CDEGS software with fixed electrode geometry and a constant lightning waveform. Outputs include the comparison of GPR across all scenarios to assess the influence of soil modeling under different regional conditions.

The organization of the paper is as follows: after the current section or the introduction of the paper as the first section, the following sections are discussed in detail as follows: Section 2) Numerical Modeling and Simulation Framework, Section 3) Research Methodology, Section 4) Results and Discussion, Section 5) Dedicated Limitations, and Section 6) Conclusion.

In Section 2, the computational theory of this study and the software used are reviewed, and in Section 3, the simulation method and requirements, study cases, and scenarios are specified, and in Section 4, the simulation results and outputs are discussed. In Section 5, the limitations considered and the assumptions used in this study are also discussed, and it will also be explicitly mentioned that system resilience analyses, integration of hydrogen energy systems, and the investigation of extreme climate events are suitable future options. Finally, in Section 6, the conclusions related to this study are drawn.

2. Numerical Modeling and Simulation Framework

2.1. Maxwell's Equations and Numerical Solution Methods

To determine electromagnetic fields at any point in space, Maxwell's equations must be solved throughout that domain. Solving Maxwell's equations enables precise modeling of grounding system behavior under lightning strikes. These fundamental equations consist of four integral forms: 1) Gauss's law for electric fields, 2) Gauss's law for magnetic fields, 3) Faraday's law, and 4) Ampere-Maxwell law. Typically expressed as partial differential equations (Equations 1.1 to 1.4), they are solved analytically in simple cases. However, when addressed computationally, numerical methods for solving differential equations become indispensable.

$$\nabla . \mathbf{D} = \rho_v \qquad (1.1)$$

$$\nabla \times \mathbf{E} = -\frac{\partial \mathbf{B}}{\partial t} \qquad (1.3)$$

$$\nabla . \mathbf{B} = 0 \qquad (1.2)$$

$$\nabla \times \mathbf{H} = -\frac{\partial \mathbf{D}}{\partial t} + \mathbf{J} \qquad (1.4)$$

Various numerical methods exist for solving integral or differential equations, each tailored to specific applications. For time- and frequency-domain problems, two- or three-dimensional scenarios, and differential or integral formulations, techniques such as FEM (Finite Element Method), FDTD (Finite-Difference Time-Domain), MoM (Method of Moments), and FIT (Finite Integration Technique) have been developed and refined to yield optimal solutions. Simulation software addressing such equations typically employs one or more of these methods or combinations thereof [16,17].

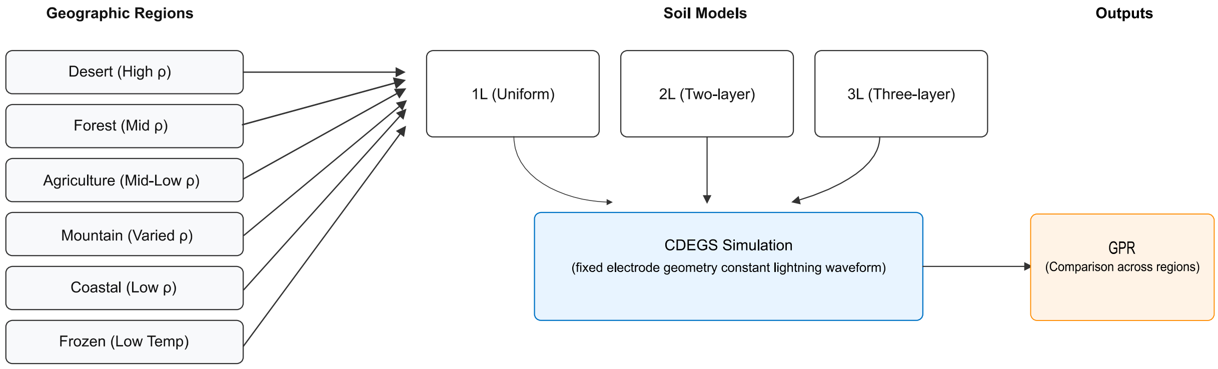

Figure 1. Graphical abstract of the present study.

2.2. Method of Moments (MoM)

The MoM is a robust numerical technique for solving integral equations derived from Maxwell's equations, widely applied in electromagnetic field analysis, particularly for computing current distributions in conductive structures. It is especially effective for analyzing high-frequency phenomena, such as electromagnetic interference and lightning effects in complex systems like grounding grids.

Maxwell's equations govern the behavior of electromagnetic fields in a medium. In steady-state or quasi-steady-state problems within conductive media, the electric scalar potential $\varnothing(\mathrm{r})$ at point r due to current density $J(r')$ is computed via the integral Equation (2):

$$\varnothing(\mathrm{r}) = \int_V G(r,r').J(r')dV' \tag{2}$$

where $G(r,r')$ is the Green's function, which models the medium's characteristics, such as soil resistivity ρ. For a homogeneous medium with electrical conductivity $\sigma = \frac{1}{\rho}$, the Green's function is defined as Equation (3):

$$G(r,r') = \frac{1}{4\pi\sigma|r-r'|} \tag{3}$$

In multilayered media, such as soils with multiple layers, the Green's function incorporates reflection terms to account for boundaries between layers with differing electrical properties, as Equation (4):

$$G(r,r') = \frac{1}{4\pi\sigma_1|r-r'|} + \sum_{k=1}^{\infty} R_k \cdot \frac{1}{4\pi\sigma_k|r-r_k'|} \tag{4}$$

where, σ_k is the conductivity of the k-th layer, and R_k are the reflection coefficients.

To implement the MoM, conductive structures (e.g., grounding grids) are discretized into N small segments, each assumed to carry a constant current I_n. The potential at an observation point r_m is then calculated as Equation (5):

$$\varnothing(r_m) = \sum_{n=1}^{N} I_n \int_{S_n} G(r_m, r')dS' \tag{5}$$

where, S_n represents the area or length of the n-th segment. By enforcing boundary conditions, such as constant potential on conductor surfaces or current continuity, a system of linear equations is established in Equation (6):

$$\mathrm{Z} \cdot \mathrm{I} = \mathrm{V} \tag{6}$$

where, Z is the impedance matrix with elements as shown in Equation (7):

$$Z_{mn} = \int_{S_m} \int_{S_n} G(\mathbf{r}_m, \mathbf{r}_n')\, dS_n'\, dS_m, \tag{7}$$

V is the vector of applied potentials or boundary conditions, and **I** is the vector of unknown currents $\{I_1, I_2, \dots, I_N\}$.

For high-frequency applications, the impedance matrix includes inductive and capacitive effects, giveny by Equation (8):

$$Z_{mn} = R_{mn} + j\omega L_{mn} + \frac{1}{j\omega C_{mn}} \tag{8}$$

where, R_{mn}, L_{mn}, and C_{mn} denote the resistance, inductance, and capacitance between segments (m) and (n), respectively. These parameters are derived from Maxwell's equations, incorporating magnetic and electric field interactions (Equations 9.1 and 9.2):

$$L_{mn} = \frac{\mu}{4\pi} \int_{S_m} \int_{S_n} \frac{1}{\mid \mathbf{r}_m - \mathbf{r}_n' \mid}\, dS_n'\, dS_m \tag{9.1}$$

$$C_{mn} = \epsilon \int_{S_m} \int_{S_n} \frac{1}{\mid \mathbf{r}_m - \mathbf{r}_n' \mid}\, dS_n'\, dS_m, \tag{9.2}$$

where, μ is the magnetic permeability and ϵ is the permittivity of the medium.

The system of equations, given by Equation (6), is solved using numerical techniques, such as direct methods (e.g., Gaussian elimination) or iterative methods (e.g., conjugate gradient). This solution yields the current distribution, facilitating the calculation of electromagnetic fields, potentials, and derived quantities like GPR or touch voltages.

The Method of Moments is especially adept at modeling intricate conductor geometries and analyzing high-frequency effects where inductive and capacitive interactions are pronounced, thereby playing a pivotal role in grounding system analysis [18].

2.3. CDEGS

Current Distribution, Electromagnetic Fields, Grounding, and Soil Structure Analysis (CDEGS) is a comprehensive software suite designed for precise analysis of electromagnetic phenomena, including grounding system behavior under high-frequency transients such as lightning, switching, and electromagnetic pulses. As a numerical electromagnetic analysis (NEA) tool, CDEGS solves Maxwell's equations in their full-wave form, leveraging the MoM. It accounts for all electromagnetic coupling modes, including conduction (via metallic elements, coatings, and soil), magnetic induction, and capacitive effects [7].

CDEGS includes modules such as RESAP, MALT, TRALIN, HIFREQ, FCDIST, MALZ, SPLITS, and FFTSES, which compute conductor currents and electromagnetic fields in arbitrary networks above or below ground under normal, fault, lightning, or transient conditions. It also models simple and multi-component conductors and buried cable systems in complex soil structures. In this study, grounding system simulations were conducted using CDEGS, with outputs post-processed via Python code [19].

2.4. *Connection of CDEGS with Maxwell's Equations and MoM*

Maxwell's equations in the frequency domain ($\nabla \times E = -j\omega B$) form the basis of calculations in HIFREQ, as MoM converts these equations into integral form for each frequency.

The Green's functions (G(r, r')), which model reflections in multi-layered soils, are derived from solving the Helmholtz equation $(\nabla^2 + k^2)G = -\delta$, which is derived from Maxwell's equations [20].

FFTSES, by transforming between time and frequency domains, enables the use of MoM in HIFREQ for analyzing lightning transients, which would be highly complex without this transformation, as directly solving Maxwell's equations in the time domain is challenging.

2.5. *Ground Potential Rise*

GPR occurs when substantial electrical current enters the ground. During lightning strikes or short circuits in high-voltage transmission lines, the voltage at the grounded point increases based on current magnitude and grounding system resistance, termed GPR. IEEE Std 80 recommends criteria such as grounding resistance (typically below 10 ohms) and touch/step potentials, often assuming uniform soil. In this study, GPR serves as the primary performance metric for grounding systems, as analyzing its waveform in both time and frequency domains offers comprehensive insights into system behavior under lightning conditions [21].

3. Methodology

In this research, simulations were conducted using the CDEGS software. This software was selected for its robust capabilities in modeling grounding systems, analyzing lightning effects, and supporting multilayered soil models. Within the software, the precise geometry of the grounding system, boundary conditions such as soil layer depths, and lightning-related input parameters were meticulously defined.

For this study, the lightning wave was modeled using the FFTSES module, while soil and grounding system configurations were established using the HIFREQ module in CDEGS. Following simulation execution, GPR outputs at the lightning injection point were obtained, and peak values were extracted using Python code, facilitating final analysis and comparison across various scenarios.

3.1. *Lightning Wave Modeling*

A typical lightning current waveform is considered, which strikes various ring and mesh grounding systems of wind turbines in two-layer soils with different resistivities. The resulting voltage rises, specifically the GPR, are calculated and analyzed to identify suitable ring and mesh configurations in various scenarios. For simulating the lightning current with parameters (Equations 10.1 to 10.3) and coefficients of the modeling function (Equations 11.1 to 11.3), a double-exponential time function is used, as shown in Equation (12), where the unit of current $I(t)$ is in amperes [22] :

$$\alpha = \frac{0.69}{T_2} \tag{11.1}$$

$$T_1 = \text{ rise time} \tag{10.1}$$

$$\beta = \frac{2.2}{T_1} \tag{11.2}$$

$$T_2 = \text{ pulse duration} \tag{10.2}$$

$$I_0 = \frac{I_p}{1 + ((\frac{\alpha}{\beta})(\ln\frac{\alpha}{\beta} - 1))} \tag{11.3}$$

$$I_p = \text{ peak amplitude} \tag{10.3}$$

$$I(t) = I_0(e^{-\alpha t} - e^{-\beta t}) \tag{12}$$

For the scenarios under consideration, parameters of a typical lightning strike were set as $T_1 = 3.4\ \mu s$, $T_2 = 13.5\ \mu s$, and $I_p = 28.51553\ kA$ [22]. Using Equations (10) and (11), the parameters for Equation (12) were computed as $\alpha = 5111.11\ s^{-1}$, $\beta = 594594.6\ s^{-1}$, and $I_0 = 30\ kA$. The lightning waveform parameters and the double-exponential coefficients are listed in Table 2. Step-by-step calculations for α, β, and I_0 are provided in Appendix A.

3.2. *Grounding System Configuration Modeling*

The grounding system comprises three electrode types: the lightning connection electrode, the electrode linking the geometric center to the main grounding electrodes, and the main grounding electrodes themselves. The lightning connection electrode, a vertical conductor, extends from 0.1 meters above ground to 1 meter below ground at the configuration's geometric center. The connecting electrode links this center to the main grounding electrodes, which form the wind turbine's grounding system.

Table 2. Lightning waveform parameters and computed double-exponential coefficients (used in simulations).

Parameter	Symbol	Value
Rise time	T_1	3.4 µs
Pulse duration	T_2	13.5 µs
Peak amplitude	I_p	28.51553 kA
Double-exponential α	α	5,111.11 s^{-1}
Double-exponential β	β	594,594.6 s^{-1}
I_0 (model constant)	I_0	30 kA

To investigate the impact of soil models on GPR, a standard grounding system was employed, consisting of a ring electrode with a 15-meter radius buried at a 1-meter depth, four 20-meter horizontal electrodes, and four 10-meter vertical electrodes penetrating to an 11-meter depth to assess deeper soil layer effects. Designed per IEEE Std. 80, this configuration aims to minimize grounding resistance and optimize GPR. All components of the grounding system used in simulations, including the ring electrode, the horizontal and vertical electrodes, the lightning connection rod, and the connecting conductor, are modeled as bare copper conductors with a cross-sectional radius of 0.0067056 m (no coating or insulation). This makes the conductor material and geometry consistent across all simulation elements.

Figure 2 illustrates the configuration of the extended ring grounding system with additional horizontal and vertical electrodes. Table 3 shows the identical grounding configuration applied across all simulations. It should be noted that the same grounding configuration (R = 15 m ring + 4 × 20 m horizontal + 4 × 10 m vertical) was used for all regions and scenarios (see Table 3). This methodological choice isolates the pure effect of soil-model variation (1L/2L/3L) on GPR by keeping electrode geometry and lightning waveform constant. The chosen configuration corresponds to commonly used earthing arrangements for wind turbine foundations and aligns with practical industry guidance (e.g., IEC recommendations on wind turbine lightning protection).

3.3. Soil Modeling

Three soil models were utilized. First, the uniform model assumes a homogeneous soil layer with constant electrical parameters. Second, the two-layer horizontal model divides soil into two layers, each with distinct thickness and electrical properties. Third, the three-layer horizontal model stratifies soil into three layers with varying thicknesses, with electrical properties based on real regional characteristics.

Figure 3 shows the side view of the three-layer soil model, where $\boldsymbol{l_1}$, $\boldsymbol{l_2}$, and $\boldsymbol{l_3}$ denote the thicknesses of the top, middle, and bottom layers, respectively, and $\boldsymbol{l_{Burial}}$ is the burial depth of the ring and horizontal electrodes. Additionally, $\boldsymbol{\rho_1}$ and $\boldsymbol{\epsilon_{r_1}}$are the resistivity and relative permittivity of the top layer, $\boldsymbol{\rho_2}$ and $\boldsymbol{\epsilon_{r_2}}$ for the middle layer, and $\boldsymbol{\rho_3}$ and $\boldsymbol{\epsilon_{r_3}}$for the bottom layer. To accurately model soil electrical behavior in CDEGS simulations, electrical parameters, including resistivity, relative permittivity, and layer thicknesses, were determined for six geographical regions (desert, forest, agricultural, mountainous, cold, and coastal) and seasons (summer and winter, except coastal areas with uniform seasonal conditions). These representative values, based on typical soil properties, environmental conditions (humidity, temperature, composition), and scientific/industrial standards, effectively simulate real-world soil behavior [23].

3.3.1. General Explanation of Parameters

- Relative Permeability: Set to 1 for all models, as the soils lack significant magnetic properties, consistent with electrical geology studies.
- Resistivity: Dependent on humidity, temperature, mineral composition, and structure, ranging from thousands of ohm-meters in dry soils to tens in moist or saline soils.
- Relative Permittivity: Influenced by moisture and composition, with higher values in wet soils (due to water's permittivity of ~80) and lower values (2-5) in dry soils.
- Layer Thickness: Determined by geological heterogeneity and moisture/frost penetration, with surface layers typically thinner (e.g., 3 meters for the first layer, 4 meters for the second, and infinite for the third), aligning with common multilayer models.

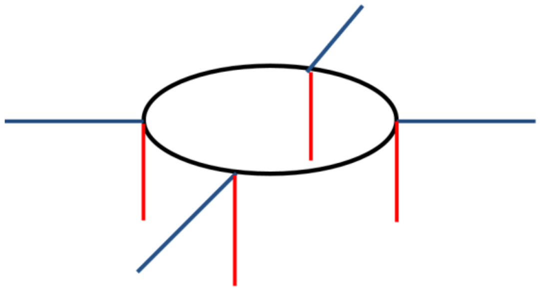

Figure 2. An extended loop grounding system configuration with additional horizontal and vertical electrodes.

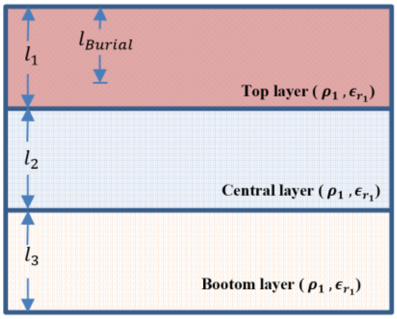

Figure 3. Three-layer soil model (side view).

Table 3. Grounding geometry in all scenarios.

Parameter	Value
Ring radius (R)	15 m
Ring burial depth	1 m
Number/length of horizontal electrodes	4 × 20 m
Number/length of vertical electrodes	4 × 10 m (depth penetration to 11 m considered in some cases)
Lightning injection point	Geometric center (0.1 m above ground) connected via a vertical rod to 1 m below ground
Electrode material	Bare copper (all electrodes, including lightning connection rod)
Electrode cross-section radius	0.0067056 m

3.3.2. Justification of Values for Each Region

a. Desert Areas

- Summer: High resistivity (4000 ohm-meters, uniform model) reflects extreme dryness, consistent with 1000-5000 ohm-meters for dry soils. Low permittivity (2) indicates minimal moisture. Multilayer models show reduced resistivity in deeper layers (2000, 1000 ohm-meters), suggesting conductive layers or slight moisture.
- Winter: Resistivity drops to 3600 ohm-meters due to potential rainfall, though soil remains dry.

b. Forest Areas

- Summer: Moderate resistivity (300 ohm-meters) reflects moisture and organic content, aligning with 100-500 ohm-meters for forest soils. High permittivity (20) confirms moisture. Deeper layers (800, 200 ohm-meters) indicate compositional shifts.
- Winter: Resistivity rises to 4000 ohm-meters due to surface freezing, with permittivity (3) reflecting reduced moisture.

c. Agricultural Areas

- Summer: Resistivity (3000 ohm-meters) suggests drier conditions, with permittivity (5) indicating moderate moisture. Deeper layers (800, 400 ohm-meters) suggest groundwater.
- Winter: Resistivity drops to 200 ohm-meters due to rainfall/irrigation, with permittivity (25) confirming water presence.

d. Mountainous Areas

- Summer: High resistivity (5000 ohm-meters) reflects rocky, dry soil, consistent with 1000-10000 ohm-meters. Permittivity (4) indicates dryness. Deeper layers (2000, 800 ohm-meters) suggest geological variations.
- Winter: Resistivity increases to 7000 ohm-meters due to freezing, with permittivity (3) aligning with cold conditions.

e. Cold Areas

- Summer: Resistivity (6000 ohm-meters) reflects dryness and low temperatures. Deeper layers (2000, 800 ohm-meters) show reduced resistivity.
- Winter: Resistivity rises to 8000 ohm-meters due to severe freezing, with permittivity (3) indicating low moisture.

f. Coastal Areas

- Summer and Winter: Low resistivity (100 ohm-meters) reflects high moisture and salinity, consistent with 2-100 ohm-meters. Permittivity (25) confirms water presence. Deeper layers (200, 50 ohm-meters) reflect salinity/moisture variations.

In conclusion, soil electrical parameters in Table 4 were selected as representative values based on geological, environmental, and reported data, accurately modeling soil behavior across diverse conditions. For practical applications, collecting region-specific soil data is recommended for enhanced precision.

For all soil models in this study, the relative permeability (p.u.) of the soil is assumed to be 1.

3.4. Assumptions

To simplify the modeling process, several assumptions were adopted. First, the frequency dependence of soil electrical parameters and soil ionization phenomena is excluded. Second, the grounding system is assumed fixed, comprising a ring electrode with horizontal and vertical extensions. Third, the soil model is limited to horizontal layers, excluding more complex configurations such as vertical, spherical, or exponential layers. These assumptions align with common practices in similar studies but do not encompass all real-world conditions. Additionally, all electrodes (mesh, ring, and connecting) are assumed to be copper. Implications are discussed in Section 5.

4. Results and Discussion

In the simulation of the case studies, the lightning wave under investigation is applied over a time range of 0 to 50 microseconds. The injection point of the lightning wave and the observation point for the GPR voltage are located 0.1 meters above the ground surface at the center of the xy-plane. The lightning wave is connected from the injection point to the geometric center of the grounding system via a vertical rod. All electrodes are made of copper with a radius of 0.0067056 meters, and their relative permittivity and relative permeability are assumed to be 1. Additionally, all electrodes used are bare, without any coating or insulation.

This section presents the results of simulations conducted using the CDEGS software to evaluate GPR in wind turbine grounding systems under lightning strikes. For each geographical region, GPR time-domain plots and bar charts of peak GPR values are provided for summer and winter seasons (except for the coastal region, where seasonal conditions are assumed uniform). The analysis focuses on the influence of soil models (uniform, two-layer, and three-layer) on GPR and identifies regional and seasonal patterns.

The grounding-system response to a lightning impulse is a time-domain transient containing rich temporal information (peak, time-to-peak, slope, frequency content). For engineering assessment of GPR, presenting the full time-domain waveform and extracting peak values is the most directly relevant approach. Statistical visualizations (e.g., boxplots) are valuable for summarizing distributions. For this study, which focuses on isolating soil-model effects under fixed electrode geometry and representative regional profiles, time-domain plots together with peak-comparison bar charts offer clearer engineering interpretation. A comprehensive statistical analysis (means, standard deviations, energy metrics) is being prepared as a follow-up study and will be reported separately (see Section 5: Limitations & Future Work).

Table 4. Thickness and electrical parameters of soil in various geographical regions and seasons for uniform, two-layer, and three-layer models.

Region type	Season type	Soil model	Soil Layer	Thickness (Meter)	Resistivity (Ohm-Meter)	Relative Permittivity (p.u.)
Desert Areas	Summer	Uniform Soil	Total layer	∞	4000	2
		Two-Layered Soil	Top Layer	3	4000	2
			Bottom Layer	∞	2000	5
		Three-Layered Soil	Top Layer	3	4000	2
			Central Layer	4	2000	5
			Bottom Layer	∞	1000	10
	Winter	Uniform Soil	Total layer	∞	3600	2
		Two-Layered Soil	Top Layer	3	3600	2
			Bottom Layer	∞	1800	5
		Three-Layered Soil	Top Layer	3	3600	2
			Central Layer	4	1800	5
			Bottom Layer	∞	900	10
Forest Areas	Summer	Uniform Soil	Total layer	∞	300	20
		Two-Layered Soil	Top Layer	3	300	20
			Bottom Layer	∞	800	15
		Three-Layered Soil	Top Layer	3	300	20
			Central Layer	4	800	15
			Bottom Layer	∞	200	30
	Winter	Uniform Soil	Total layer	∞	4000	3
		Two-Layered Soil	Top Layer	3	4000	3
			Bottom Layer	∞	1000	10
		Three-Layered Soil	Top Layer	3	4000	3
			Central Layer	4	1000	10
			Bottom Layer	∞	500	25
Agricultural Areas	Summer	Uniform Soil	Total layer	∞	3000	5
		Two-Layered Soil	Top Layer	3	3000	5
			Bottom Layer	∞	800	15
		Three-Layered Soil	Top Layer	3	3000	5
			Central Layer	4	800	15
			Bottom Layer	∞	400	25
	Winter	Uniform Soil	Total layer	∞	200	25
		Two-Layered Soil	Top Layer	3	200	25
			Bottom Layer	∞	100	40
		Three-Layered Soil	Top Layer	3	200	25
			Central Layer	4	100	40
			Bottom Layer	∞	500	20
Mountain Areas	Summer	Uniform Soil	Total layer	∞	5000	4
		Two-Layered Soil	Top Layer	3	5000	4
			Bottom Layer	∞	2000	10
		Three-Layered Soil	Top Layer	3	5000	4
			Central Layer	4	2000	10
			Bottom Layer	∞	800	20
	Winter	Uniform Soil	Total layer	∞	7000	3
		Two-Layered Soil	Top Layer	3	7000	3
			Bottom Layer	∞	3000	6
		Three-Layered Soil	Top Layer	3	7000	3
			Central Layer	4	3000	6
			Bottom Layer	∞	1000	15
Cold Areas	Summer	Uniform Soil	Total layer	∞	6000	5
		Two-Layered Soil	Top Layer	3	6000	5
			Bottom Layer	∞	2000	12
		Three-Layered Soil	Top Layer	3	6000	5
			Central Layer	4	2000	12
			Bottom Layer	∞	800	18
	Winter	Uniform Soil	Total layer	∞	8000	3
		Two-Layered Soil	Top Layer	3	8000	3
			Bottom Layer	∞	3000	8
		Three-Layered Soil	Top Layer	3	8000	3
			Central Layer	4	3000	8
			Bottom Layer	∞	1500	12
Coastal Areas	Summer / Winter	Uniform Soil	Total layer	∞	100	25
		Two-Layered Soil	Top Layer	3	100	25
			Bottom Layer	∞	200	80
		Three-Layered Soil	Top Layer	3	100	25
			Central Layer	4	200	80
			Bottom Layer	∞	50	40

As observed in Figures 4, 5, 6, and 7, in the desert region, characterized by dry soil and high resistivity, the use of multilayer soil models significantly reduces peak GPR. In summer, the peak GPR for the uniform (single-layer) model is 1,107,882 V, which decreases to 701,091.7 V (a 36.7% reduction) with the two-layer model and further to 504,517.4 V (a 28.1% reduction relative to the two-layer model) with the three-layer model. In winter, the peak GPR decreases from 998,236.5 V in the uniform model to 633,778.6 V in the two-layer model (a 36.5% reduction) and then to 461,419.5 V in the three-layer model (a 27.2% reduction relative to the two-layer model). This trend indicates a consistent reduction in peak GPR with an increasing number of layers in both seasons. This reduction is attributed to the better distribution of lightning current into deeper layers with lower resistivity in multilayer models.

As shown in Figures 8, 9, 10, and 11, in the forest region, seasonal conditions markedly influence GPR behavior. In summer, the peak GPR for the uniform model is 222,271.8 V, the lowest value observed. This increases to 265,347.7 V (a 19.4% increase) with the two-layer model and decreases to 234,135.3 V (an 11.8% reduction relative to the two-layer model) with the three-layer model. In winter, however, the peak GPR for the uniform model rises sharply to 1,107,012 V, decreasing to 454,773 V (a 58.9% reduction) with the two-layer model and further to 370,819.8 V (an 18.5% reduction relative to the two-layer model) with the three-layer model. These results suggest that the uniform model performs best in summer, while the three-layer model excels in winter. This variation is attributed to changes in soil moisture and its effect on resistivity. As depicted in Figures 12,13, 14, and 15, in the agricultural region, the peak GPR in summer for the uniform model is 832,480.2 V, decreasing to 379,717.1 V (a 54.4% reduction) with the two-layer model and to 365,533 V (a 3.7% reduction relative to the two-layer model) with the three-layer model. In winter, the peak GPR for the uniform model is 189,255.2 V, reducing to 173,916.2 V (an 8.1% reduction) with the two-layer model and increasing slightly to 182,653.6 V (a 5.0% increase relative to the two-layer model) with the three-layer model.

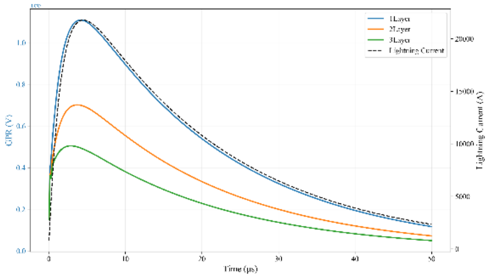

Figure 4. Lightning wave and GPR graphs in desert areas and the summer season for horizontal soil models: uniform, two-layer, and three-layer.

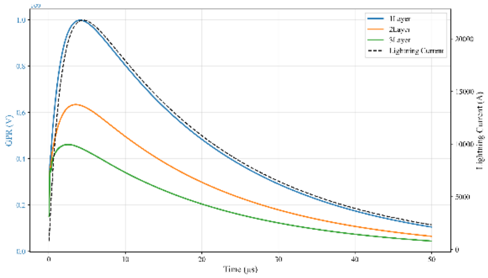

Figure 5. Lightning wave and GPR graphs in desert areas and winter season for horizontal soil models: uniform, two-layer, and three-layer.

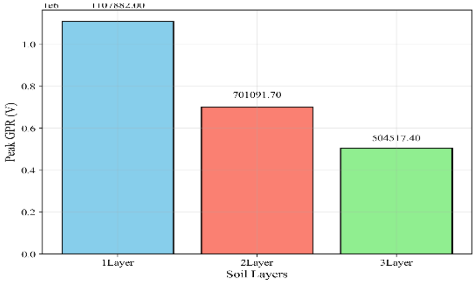

Figure 6. GPR peak bar graph in desert areas and summer season for horizontal soil models: uniform, two-layer, and three-layer.

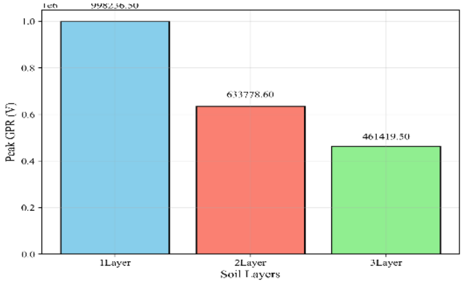

Figure 7. GPR peak bar graph in desert areas and winter season for horizontal soil models: uniform, two-layer, and three-layer.

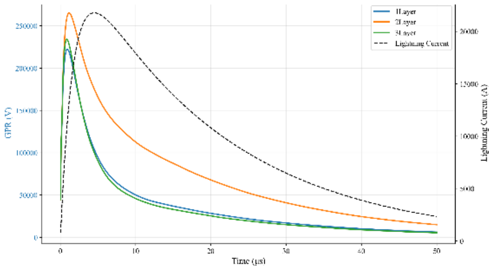

Figure 8. Lightning wave and GPR graphs in forest areas and summer season for horizontal soil models: uniform, two-layer and three-layer.

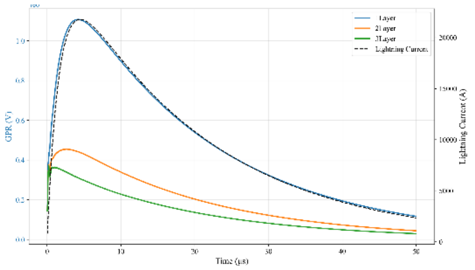

Figure 9. Lightning wave and GPR graphs in forest areas and winter season for horizontal soil models: uniform, two-layer, and three-layer.

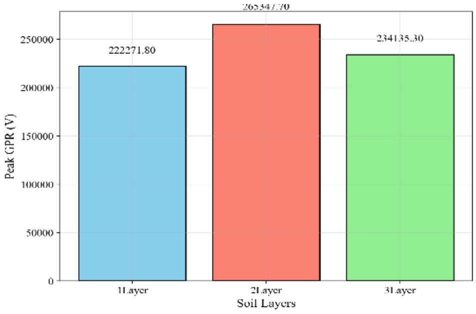

Figure 10. GPR peak bar graph in forest areas and summer season for horizontal soil models: uniform, two-layer, and three-layer.

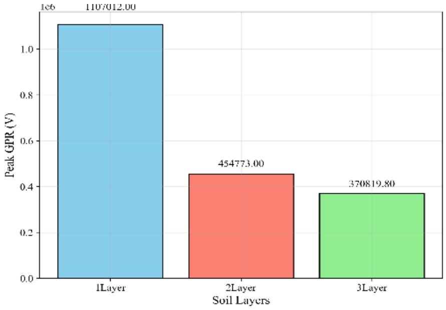

Figure 11. GPR peak bar graph in forest areas and winter season for horizontal soil models: uniform, two-layer, and three-layer.

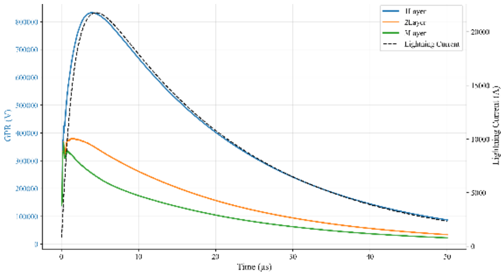

Figure 12. Lightning wave and GPR graphs in agricultural areas and the summer season for horizontal soil models: uniform, two-layer, and three-layer.

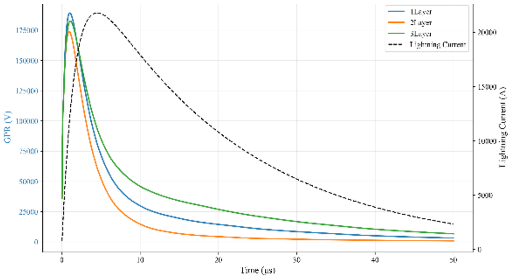

Figure 13. Lightning wave and GPR graphs in agricultural areas and winter season for horizontal soil models: uniform, two-layer, and three-layer.

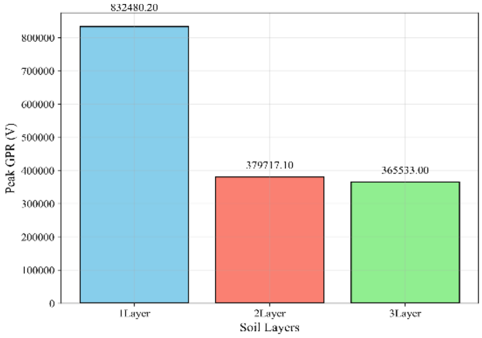

Figure 14. GPR peak bar graph in agricultural areas and the summer season for horizontal soil models: uniform, two-layer, and three-layer.

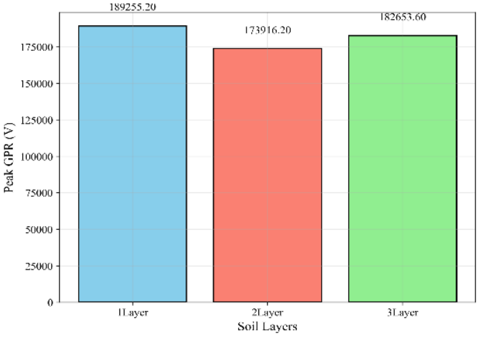

Figure 15. GPR peak bar graph in agricultural areas and winter season for horizontal soil models: uniform: two-layer, and three-layer.

These findings indicate that the three-layer model yields the lowest peak GPR in summer, while the two-layer model performs best in winter. This variable behavior is linked to differences in agricultural soil properties, including moisture and electrical conductivity, across seasons. As illustrated in Figures 16, 17, 18, and 19, in the mountainous region, the peak GPR in summer for the uniform model is 1,376,495 V, decreasing to 750,228.4 V (a 45.5% reduction) with the two-layer model and to 481,227.2 V (a 35.9% reduction relative to the two-layer model) with the three-layer model. In winter, the peak GPR for the uniform model is 1,925,471 V, reducing to 1,093,948 V (a 43.2% reduction) with the two-layer model and to 625,582.2 V (a 42.8% reduction relative to the two-layer model) with the three-layer model. These results demonstrate that increasing the number of layers consistently reduces peak GPR in both seasons, with the three-layer model exhibiting the best performance. This reduction is attributed to the heterogeneity of mountainous soil and the presence of deeper layers with lower resistivity.

As presented in Figures 20, 21, 22, and 23, in the frozen region, the peak GPR in summer for the uniform model is 1,643,587 V, decreasing to 791,952.5 V (a 51.8% reduction) with the two-layer model and to 504,409.4 V (a 36.3% reduction relative to the two-layer model) with the three-layer model. In winter, the peak GPR for the uniform model is 2,197,587 V, reducing to 1,139,922 V (a 48.1% reduction) with the two-layer model and to 802,833.2 V (a 29.6% reduction relative to the two-layer model) with the three-layer model. These results highlight the superiority of the three-layer model in both seasons, linked to the high-resistivity frozen surface layer and lower-resistivity deeper layers in multilayer models.

As shown in Figures 24 and 25, in the coastal region, where seasonal conditions are assumed uniform, the peak GPR for the uniform model is 137,727.1 V, decreasing to 119,138.5 V (a 13.5% reduction) with the two-layer model and slightly increasing to 119,162.4 V (a negligible 0.02% increase relative to the two-layer model) with the three-layer model. These results indicate that the two-layer model provides the lowest peak GPR, though the difference between the two- and three-layer models is minimal. This behavior is attributed to the water-saturated soil and low resistivity in coastal regions, where changes in the soil model have a limited impact on GPR.

In other words, in coastal areas, the topsoil is typically low-resistivity (e.g., ≈100 Ω·m) due to moisture and salinity and has high permittivity. Intermediate layers can exhibit relatively higher resistivity due to evaporation-driven processes or sediment layers, while deeper layers may become saturated with saline groundwater and again show much lower resistivity (e.g., the [100 | 200 | 50] Ω·m profile). In such three-layer configurations, a deep, very conductive layer enables easier current penetration to depth and reduces the overall effective grounding resistance, which explains why GPR does not necessarily increase and may instead reduce slightly. Numerical checks (mesh/refinement and convergence in CDEGS) were performed and did not indicate modeling instability artifacts; hence, the observed behavior is consistent with plausible coastal hydrogeological profiles.

Figure 26 provides a comprehensive overview of peak GPR across all geographical regions, seasons, and soil models. The highest peak GPR is observed in the frozen region in winter with the uniform model (2,197,587 V), while the lowest is in the coastal region with the two-layer model (119,138.5 V). In regions with high soil resistivity (desert, mountainous, and frozen), increasing the number of layers consistently reduces peak GPR, with the three-layer model performing best. For instance, in the frozen region in winter, peak GPR decreases from 2,197,587 V in the uniform model to 802,833.2 V in the three-layer model (a 63.5% reduction), the largest percentage reduction observed. In contrast, in the coastal region, changing the soil model results in only a 13.5% reduction in peak GPR.

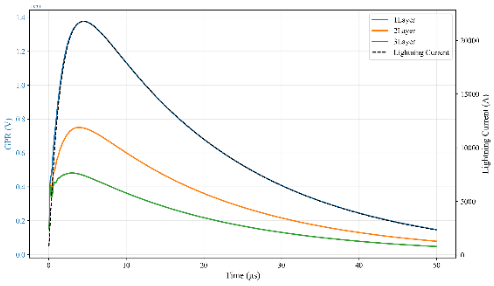

Figure 16. Lightning wave and GPR graphs in mountainous areas and the summer season for horizontal soil models: uniform, two-layer, and three-layer.

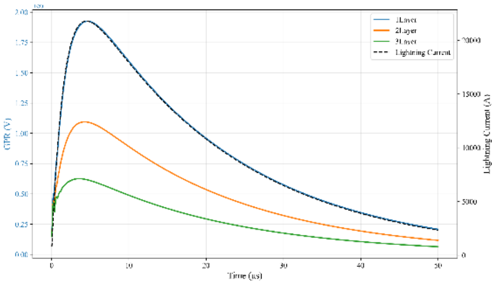

Figure 17. Lightning wave and GPR graphs in mountainous areas and winter season for horizontal soil models: uniform, two-layer, and three-layer.

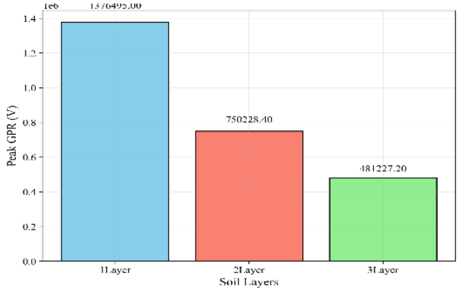

Figure 18. GPR peak bar graph in mountainous areas and the summer season for horizontal soil models: uniform, two-layer, and three-layer.

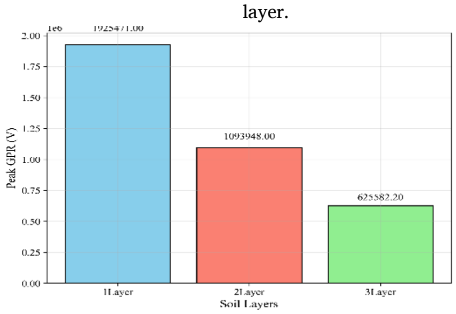

Figure 19. GPR peak bar graph in mountainous areas and winter season for horizontal soil models: uniform, two-layer, and three-layer.

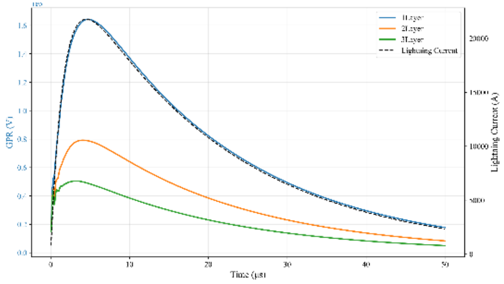

Figure 20. Lightning wave and GPR graphs in frozen areas and summer season for horizontal soil models: uniform, two-layer, and three-layer.

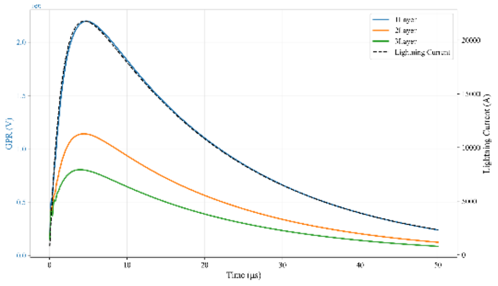

Figure 21. Lightning wave and GPR graphs in frozen areas and winter season for horizontal soil models: uniform, two-layer, and three-layer.

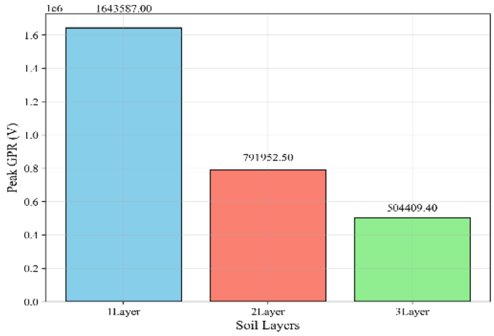

Figure 22. GPR peak bar graph in frozen areas and summer season for horizontal soil models: uniform, two-layer, and three-layer.

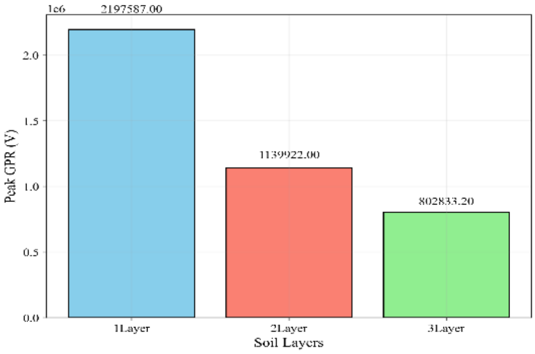

Figure 23. GPR peak bar graph in frozen areas and winter season for horizontal soil models: uniform, two-layer, and three-layer.

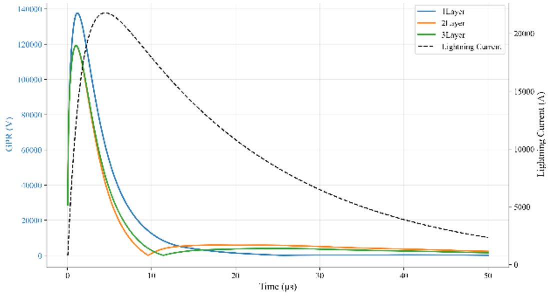

Figure 24. Lightning wave and GPR graphs in coastal areas and summer/winter season for horizontal soil models: uniform, two-layer, and three-layer.

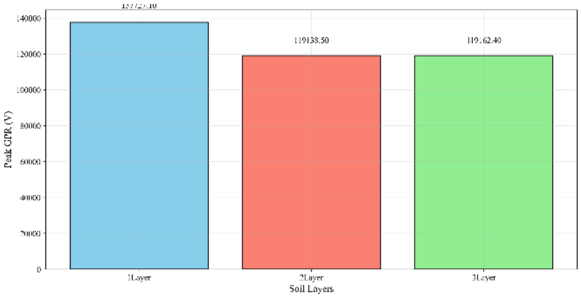

Figure 25. GPR peak bar graph in coastal areas and summer/winter season for horizontal soil models: uniform, two-layer, and three-layer.

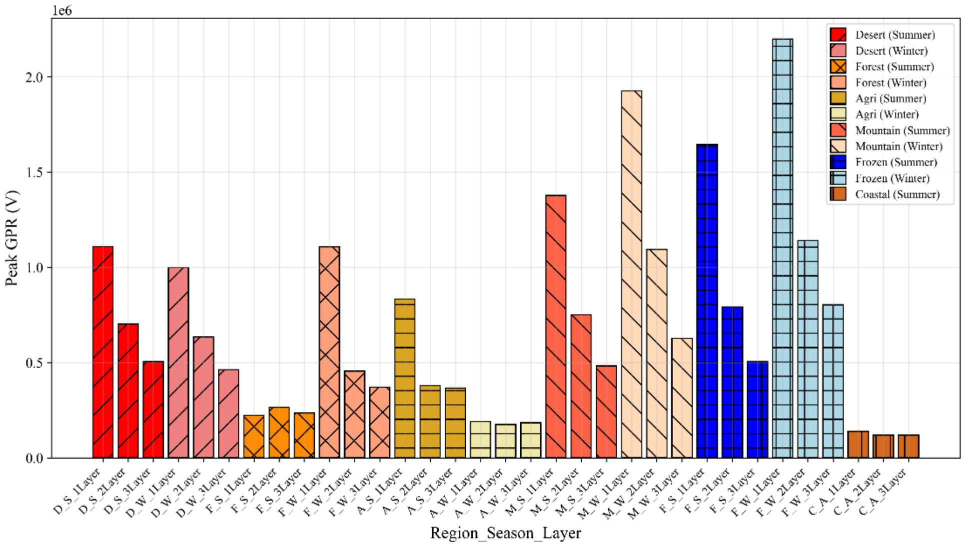

Figure 26. Comparison of peak GPR voltage for all geographical regions, seasons, and soil models.

In forest and agricultural regions, patterns vary. In the forest region, the uniform model in summer (222,271.8 V) and the three-layer model in winter (370,819.8 V) yield the lowest peak GPR values. In the agricultural region, the three-layer model in summer (365,533 V) and the two-layer model in winter (173,916.2 V) perform best. These findings suggest that soil model selection should account for regional and seasonal conditions, as increasing the number of layers does not always reduce GPR.

The results of this study emphasize the importance of using real soil data in designing wind turbine grounding systems. In dry and frozen regions, multilayer modeling can significantly enhance safety, whereas in coastal regions, simpler models may suffice. Engineers and designers should select appropriate soil models based on regional and seasonal characteristics to ensure optimal lightning protection.

5. Limitations and Future Work

This section lists the principal methodological limitations that may affect the generality of findings and outlines recommended future research:

a. Neglect of frequency-dependent soil parameters: Soil electrical properties were treated as frequency-independent to isolate pure layering effects. Previous works indicate that frequency dependence can affect transient responses, particularly in high-resistivity soils [3,6]. Frequency-dependent modeling is recommended for targeted follow-up studies.

b. Exclusion of soil ionization: Ionization effects near conductors under strong impulses can alter local conductivity and current paths [17]. Modeling ionization requires nonlinear approaches and experimental calibration and was therefore excluded here.

c. Horizontal-layer assumption only: Horizontally layered soil models are the most common and practical representation for many field sites and are widely used in earthing studies. Nonetheless, vertical inhomogeneities, channels, or localized anomalies would require 3D or non-horizontal modeling to capture accurately. The rationale is discussed in Section 3.3.

d. Fixed electrode geometry and lightning waveform: Geometry and waveform were kept constant across regions to isolate soil-model effects; while appropriate for systematic comparison, practical design should consider geometric variations and interconnection effects.

e. Parameter uncertainty: Soil parameters used are representative; full uncertainty/sensitivity analysis is recommended as a follow-up.

f. Suggested extensions: Future work should include (i) frequency-dependent and ionization-inclusive modeling, (ii) 3D non-horizontal soil heterogeneity studies, (iii) comprehensive statistical analysis (means, stds, energy metrics), and (iv) field campaigns for validation.

See Assumptions (Section 3.4) for modeling choices.

6. Conclusion

This study used CDEGS simulations to investigate the influence of soil modeling choices (1L/2L/3L) on Ground Potential Rise (GPR) for wind turbine earthing systems across six geographic regions. Key findings are:

- In high-resistivity regions (desert, mountainous, frozen), multilayer soil models yield substantial reductions in peak GPR (example: frozen region, winter, peak reduced from ≈2,197,587 V to ≈802,833.2 V with the 3-layer model, ≈63.5% reduction).
- In conductive regions such as coastal areas, soil-model changes have a limited impact on peak GPR (≈13.5% reduction); thus, simpler models may suffice for preliminary design in such locales.
- Increased soil-model complexity does not guarantee GPR reduction in all cases; outcomes depend strongly on local layer resistivities, thicknesses, and seasonal conditions.

Practical implication: Engineers should incorporate site-specific soil data and seasonal variability when designing wind turbine earthing; multilayer characterization is particularly important in high-resistivity environments.

Limitations and future work: Frequency-dependent soil properties, soil ionization effects, and vertical/non-horizontal heterogeneity were not included (see Section 5). A comprehensive statistical study (means, standard deviations, energy-based metrics) is underway as a follow-up to strengthen quantitative comparisons.

Appendix A: Calculation of double-exponential parameters

For transparency and reproducibility, the computation of the double-exponential model parameters used in Equation (12) is presented here. The assumed lightning parameters (as in [22]) are:

$$T_1 = 3.4\ \mu\text{s}, T_2 = 13.5\ \mu\text{s}, \text{I}_p = 28.51553\ \text{kA}$$

The relations used (Equations 11.1 to 11.3) are:

$$\alpha = \frac{0.69}{T_2}$$

$$\beta = \frac{2.2}{T_1}$$

$$I_0 = \frac{I_p}{1 + (\frac{\beta}{\alpha})(\ln\frac{\alpha}{\beta} - 1)}$$

Substituting numbers gives:

$$\alpha = \frac{0.69}{13.5\ \times\ 10^{-6}} \approx\ 5111.11\ s^{-1}$$

$$\beta = \frac{2.2}{3.4\ \times\ 10^{-6}} \approx\ 594594.6\ s^{-1}$$

Using the formula for I_0 yields $I_0\ \approx 30\ kA$. These numeric values were applied in the CDEGS simulations (see Section 3.1).

References

[1] R. Alipio, M. T. Correia de Barros, M. A. O. Schroeder, and K. Yamamoto, "Analysis of the Lightning Impulse and Low-Frequency Performance of Wind Farm Grounding Systems," *Electric Power Systems Research*, vol. 180, 106068, 2020.

[2] Y. Hu, Z. Liu, et al., "A New Grounding Resistance Reduction Method for Wind Turbines by Grounding Grid Connection in Limited Areas," *Frontiers in Energy Research*, vol. 10, 2022.

[3] N. A. Sabiha and N. I. Elkalashy, "Evaluation of Grounding System Design for Wind Farm Using COMSOL," *International Journal of Applied Engineering Research*, vol. 13, no. 6, pp. 4124–4132, 2018.

[4] A. Djaborebbi, B. Zegnini, and D. Mahi, "Analysis of the Performance of Grounding Grids Buried in Heterogeneous Soil Under Impulse Current," *Indonesian Journal of Electrical Engineering and Computer Science*, vol. 22, no. 1, 571, 2021.

[5] R. Alipio, D. Conceição, et al., "A Comprehensive Analysis of the Effect of Frequency-Dependent Soil Electrical Parameters on the Lightning Response of Wind-Turbine Grounding Systems," *Electric Power Systems Research*, vol. 175, 105927, 2019.

[6] R. Alipio, M. Guimarães, L. Passos, D. Conceição, and M. T. C. de Barros, "Ground Potential Rise in Wind Farms Due to Direct Lightning," *Electric Power Systems Research*, vol. 194, 107110, 2021.

[7] S. E. S. Technologies, "CDEGS: Current Distribution, Electromagnetic Fields, Grounding and Soil Structure Analysis," Safe Engineering Services & Technologies (SES)

[8] E. Software, "Wind Farm Earthing Design and Modelling Guide (technical guide)," Elek.

[9] M. Yao, Z. Moradi, S. Pirouzi, M. Marzband, and A. Baziar, "Stochastic Economic Operation of Coupling Unit of Flexi-Renewable Virtual Power Plant and Electric Spring in the Smart Distribution Network," *IEEE Access*, vol. 11, pp. 75979–75992, 2023.

[10] R. B. Navesi, A. F. Naghibi, H. Zafarani, H. Tahami, and S. Pirouzi, "Reliable Operation of Reconfigurable Smart Distribution Network with Real-Time Pricing-Based Demand Response," *Electric Power Systems Research*, vol. 241, 111341, 2025.

[11] J. Zhang, H. Wu, E. Akbari, L. Bagherzadeh, and S. Pirouzi, "Eco-Power Management System with Operation and Voltage Security Objectives of Distribution System Operator Considering Networked Virtual Power Plants with Electric Vehicles Parking Lot and Price-Based Demand Response," *Computers and Electrical Engineering*, vol. 121, 109895, 2025.

[12] R. Wang, E. Akbari, L. Bagherzadeh, and S. Pirouzi, "Stochastic Economic Sizing of Hydrogen Storage-Based Renewable Off-Grid System with Smart Charge of Electric Vehicles According to Combined Hydrogen and Power Model," *Journal of Energy Storage*, vol. 108, 115171, 2025.

[13] M. H. Oboudi, H. Hamidpour, M. Zadehbagheri, S. Safaee, and S. Pirouzi, "Reliability-Constrained Transmission Expansion Planning Based on Simultaneous Forecasting Method of Loads and Renewable Generations," *Electrical Engineering*, vol. 107, no. 1, pp. 1141–1161, 2024.

[14] M. Zadehbagheri, M. Dehghan, M. Kiani, and S. Pirouzi, "Resiliency-Constrained Placement and Sizing of Virtual Power Plants in the Distribution Network Considering Extreme Weather Events," *Electrical Engineering*, vol. 107, no. 2, pp. 2089–2105, 2024.

[15] A. F. Naghibi, E. Akbari, S. Shahmoradi, S. Pirouzi, and A. Shahbazi, "Stochastic Economic Sizing and Placement of Renewable Integrated Energy System with Combined Hydrogen and Power Technology in the Active Distribution Network," *Scientific Reports*, vol. 14, no. 1, 2024.

[16] R. Guizán, I. Colominas, J. París, I. Couceiro, and F. Navarrina, "Numerical Analysis and Safety Design of Grounding Systems in Underground Compact Substations," *Electric Power Systems Research*, vol. 203, 107627, 2022.

[17] B. Nekhoul, B. Harrat, A. Boutadjine, and M. Melit, "A Simplified Numerical Modeling of the Transient Behavior of Grounding Systems Considering Soil Ionization," *Electric Power Systems Research*, vol. 211, 108182, 2022.

[18] M. R. Alemi, S. H. H. Sadeghi, and H. Askarian-Abyaneh, "A Marching-On-In-Time Method of Moments for Computation of Transient Potential Rise of Grounding Grids Exposed to Lightning Strikes," *IEEE Transactions on Electromagnetic Compatibility*, vol. 65, no. 5, pp. 1484–1491, 2023.

[19] Q. Ma, J. Xie, et al., "Analysis of Grounding Impedance Spectrum Based on CDEGS with Different Soil Characteristics," *2022 IEEE International Conference on High Voltage Engineering and Applications (ICHVE)*, pp. 1–4, 2022.

[20] Y. Dan, Z. Zhang, et al., "A Novel Segmented Sampling Numerical Calculation Method for Grounding Parameters in Horizontally Multilayered Soil," *International Journal of Electrical Power & Energy Systems*, vol. 126, 106586, 2021.

[21] A. Taher, A. Said, T. Eliyan, and A. Hafez, "Analysis and Mitigation of Ground Grid Lightning Potential Rise," *Transactions on Electrical and Electronic Materials*, vol. 21, no. 3, pp. 305–314, 2020.

[22] O. Kherif, S. Chiheb, M. Teguar, A. Mekhaldi, and N. Harid, "Time-Domain Modeling of Grounding Systems' Impulse Response Incorporating Nonlinear and Frequency-Dependent Aspects," *IEEE Transactions on Electromagnetic Compatibility*, vol. 60, no. 4, pp. 907–916, 2018.

[23] N. A. Sabiha, M. Alsharef, et al., "Assessment of Grounding Grid for Enhancing Wind Turbine Service Sustainability," *Ain Shams Engineering Journal*, vol. 12, no. 1, pp. 577–589, 2021.

Declaration of competing interest

The authors declare that they have no known competing financial interests or personal relationships that could have appeared to influence the work reported in this paper. The ethical issues, including plagiarism, informed consent, misconduct, data fabrication and/or falsification, double publication and/or submission, redundancy, have been completely observed by the authors.

Bibliography

Omid Heydari was born in 1988 in the city of Ilam, Iran. He received his Bachelor's degree in Electrical Engineering from the Islamic Azad University of Arak in 2011, followed by a Master's degree in Power Electrical Engineering from the University of Ilam in 2017. Since 2019, he has been a Ph.D. student in Electrical Engineering at Razi University, Kermanshah, Iran. His academic interests are mainly focused on research and development in the field of lightning protection systems, particularly for electrical equipment such as wind turbines. His research activities aim to improve the reliability and protection of power and renewable energy systems against lightning-related hazards.
Email: omid96833@gmail.com
ORCID: 0009-0009-9236-8702
Contribution Statement: Conceptualization, Data curation, Formal analysis, Investigation, Methodology, Software, Validation, Writing - original draft.

Dr. Hassan Moradi Cheshmehbeigi is an Associate Professor in the Department of Electrical Engineering at the Faculty of Engineering, Razi University, Kermanshah, Iran, where he has been a faculty member since 2011. He was born in Kermanshah, Iran, in 1979 and completed his Ph.D. in Electrical Engineering at Shahid Beheshti University, Tehran, Iran, earning his degree in 2011 before joining Razi University's academic staff. At Razi University, Dr. Moradi teaches undergraduate and graduate courses and actively conducts research in key areas of electrical engineering, with particular emphasis on power systems, electrical machines, power electronics, microgrids, and advanced control strategies for modern energy systems. His research contributions include numerous peer-reviewed journal and conference publications focused on topics such as microgrid stability and control, HVDC systems, electromagnetic design of electric machines, power converter control, and energy system optimization, reflecting his extensive engagement with both theoretical and applied aspects of electrical engineering. Dr. Moradi's work has been widely cited in the academic community, and he collaborates with researchers nationally and internationally to advance innovative solutions in power and energy engineering.
Email: ha.moradi@razi.ac.ir
ORCID: 0000-0002-4802-6117
Contribution Statement: Data curation, Funding acquisition, Investigation, Supervision, Writing-review & editing.

Dr. Shahram Karimi is an Assistant Professor in the Department of Electrical Engineering, Faculty of Engineering, Razi University, Kermanshah, Iran. He was born in Kermanshah, Iran, in 1972. He received his Bachelor's degree in Electrical Engineering from the University of Tabriz in 1995, followed by a Master's degree from Sharif University of Technology, Tehran, in 1997. He earned his Ph.D. in Electrical Engineering from Université Henri Poincaré (Nancy I), France, in 2008. After completing his doctoral studies, he joined Razi University, where he has been actively involved in teaching and research in the field of electrical engineering. His main research interests include power systems analysis and control, microgrids, voltage and frequency control, power quality, renewable energy integration, FACTS devices, and fault-tolerant power converters. Dr. Karimi has published numerous research papers in reputable national and international journals and conferences and has contributed significantly to the development of advanced control and optimization methods for modern power and energy systems.
Email: shahramkarimi@razi.ac.ir
ORCID: 0000-0002-6649-5646
Contribution Statement: Conceptualization, Formal analysis, Project administration, Resources, Supervision, Writing-review & editing.

Hamdi Abdi was born in Paveh, Iran, in July 1973. He received the B.Sc. degree from Tabriz University, Tabriz, Iran, in 1995, and the M.Sc. and Ph.D. degrees from Tarbiat Modares University, Tehran, Iran, in 1999 and 2006, respectively, all in electrical engineering. He is currently a Full Professor in the Department of Electrical Engineering, Razi University, Kermanshah, Iran. His research interests include power system operation and planning, smart energy systems, uncertainty management, and energy hub.
Email: hamdiabdi@razi.ac.ir
ORCID: 0000-0002-7625-0036
Contribution Statement: Conceptualization, Funding acquisition, Methodology, Supervision, Validation, Writing-original draft.

Journal of
Green Energy
Research and Innovation

Investigating Energy Consumption Reduction Strategies and Their Effect on the Renewable Electricity Price: A Case Study of a Climate-Compatible Villa in Saman, Iran

Narges Loghmani

Highlights

- **Combining all energy efficiency measures reduced the Net Present Cost of the off-grid solar system by 79.5%, dropping it from $947,243 to approximately $194,000.**
- **Upgrading to a VRF HVAC system provided the largest single cost reduction at 63.1%, significantly outperforming insulation or window upgrades.**
- **The optimal integrated scenario increased the return on investment by 146% while reducing annual carbon emissions by roughly 130 tons.**
- **This study proves that prioritizing building energy efficiency before sizing renewable systems is crucial for cost-effective off-grid electrification.**

Graphical Abstract

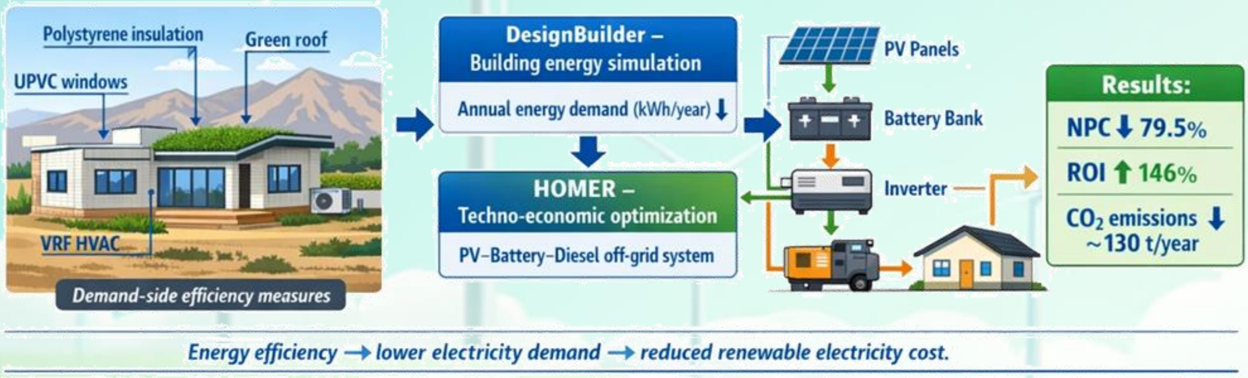

Use your device to scan and read the article online

Citation
N. Loghmani, "Investigating Energy Consumption Reduction Strategies and their Effect on the Renewable Electricity Price: A Case Study of a Climate-Compatible Villa in Saman, Iran," Journal of Green Energy Research and Innovation, vol. 3, no. 1, pp. 16-30, 2026.

https://doi.org/10.61882/jgeri.3.1.16

Journal of Green Energy Research and Innovation 3.1 (2026) 16-30

Online ISSN: 3041-9018

Journal of Green Energy Research and Innovation

Journal Homepage: www.jgeri.araku.ac.ir

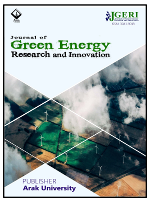

Investigating Energy Consumption Reduction Strategies and Their Effect on the Renewable Electricity Price: A Case Study of a Climate-Compatible Villa in Saman, Iran

Narges Loghmani [*]

Department of Architecture and Urban Planning, Technical and Vocational University (TVU), Tehran, Iran.

ARTICLE INFO

Keywords:
Net present cost,
Optimized scenario,
Renewable electricity price,
Reducing energy consumption,
Climate-compatible villa.

Article History:
Received: 18 May 2025;
Revised: 17 August 2025;
Accepted: 03 September 2025.

Article type:
Research Article

* ***Corresponding author***
E-mail address
nloghmani@tvu.ac.ir (N. Loghmani)

ABSTRACT

The main objective of this study is to evaluate the impact of building energy efficiency measures on the cost of solar electricity in a climate-compatible villa located in the suburbs of Saman, Chaharmahal and Bakhtiari Province, Iran. Enhancing building energy efficiency while lowering the cost of renewable electricity generation is particularly vital in Iran's off-grid residential sector, where growing energy demand and dependence on fossil fuels necessitate sustainable, climate-compatible solutions. A baseline case and five optimization scenarios were modeled using DesignBuilder (v6.1.0.6) to estimate annual energy consumption, followed by techno–economic–environmental assessment of an off-grid solar–battery–diesel generator system using HOMER (v2.81). Results show that the net present cost (NPC) of the baseline system is $947,243, with cost reductions of 17.6%, 5.4%, 22.7%, 63.1%, and 79.5% achieved through polystyrene insulation, green roof, UPVC windows, VRF HVAC, and all measures combined, respectively. The optimal integrated scenario also reduces annual emissions by ~130 tons and increases the return on investment (ROI) by 146%. This work uniquely couples building-level energy efficiency modeling with techno–economic–environmental optimization of a hybrid off-grid PV– Battery–Diesel generator system, quantifying for the first time how demand-side measures propagate into key renewable electricity cost metrics in off-grid residential contexts. These findings highlight the substantial economic and environmental benefits of combining building optimization strategies with renewable energy deployment in off-grid residential applications.

1. Introduction

The residential sector in Iran alone accounts for approximately 28% of the country's total energy consumption (Figure 1) [1], with the majority of this energy supplied from fossil fuel sources [2]. This dependency not only increases greenhouse gas emissions and exacerbates environmental challenges but also places a significant economic burden on the national energy sector. In a context where fuel price fluctuations, depletion of fossil resources, and international commitments to reduce pollutants have become pressing concerns, transitioning toward energy-efficient buildings and the utilization of renewable energy (RE) has emerged as a strategic necessity for Iran. This necessity is further underscored by socio-economic trends, as population growth and the growing demand for recreational living during weekends and holidays in pleasant off-grid regions continue to drive energy use upward. Consequently, enhancing efficiency, reducing energy consumption, and decreasing reliance on the national grid have become particularly important. Achieving energy independence in off-grid buildings typically involves two complementary strategies: (i) reducing energy consumption through building optimization and energy management, and (ii) meeting the remaining demand using renewable sources such as solar and wind power.

Building on this second strategy, the use of RE sources, particularly solar photovoltaic (PV) and wind power, is a top priority in off-grid regions due to their modularity, scalability, and independence from fuel supply chains. The share of RE production, comprising hydropower, wind, solar, biomass, and geothermal energy, in net-zero energy buildings has been widely examined in previous studies [3-5]. As shown in Figure 2, wind energy accounts for 24% and solar PV for 40% of the supply mix, both of which are highly adaptable for decentralized and residential-scale deployment, making them particularly attractive for off-grid applications. Their complementary seasonal and diurnal profiles, solar PV producing peak output during the day and wind often contributing more at night or in colder months, enhance system reliability. Multiple studies confirm that hybrid renewable energy systems, combining two or more sources, achieve a lower levelized cost of electricity (LCOE) and improved supply stability compared to single-source configurations [6]. This supports the multi-source integration approach adopted in the present study to ensure both economic viability and long-term resilience in off-grid villas.

Complementary to the deployment of renewable energy technologies, effective demand-side management and building energy optimization are equally critical to ensuring the technical, economic, and environmental sustainability of off-grid systems. In parallel with expanding renewable generation, managing energy consumption effectively is essential to achieving energy independence, especially in regions where grid access is unavailable or limited. Energy consumption in Iran has been rising steadily in recent years, driven by population growth, economic expansion, and industrial development [8,9]. Advanced energy monitoring, through real-time tracking and analysis of consumption, enables the identification of inefficiencies and targeted interventions [10,11]. Complementary measures such as high-performance wall and roof insulation, green roofs, double-glazed UPVC windows, intelligent lighting controls, and variable refrigerant flow (VRF) systems significantly reduce thermal losses and improve overall building efficiency [12-15].

The upward trend in total energy and electricity consumption from 2011 to 2021 is shown in Figure 3, accompanied by steady growth in renewable electricity generation from wind, hydro, and solar sources. While this indicates progress toward cleaner energy, the current pace of renewable deployment remains insufficient to meet the country's rapidly growing demand. As illustrated in Figure 4, wind and solar energy production have both expanded significantly since 2013, with solar showing particularly strong growth after 2017. This complementary generation pattern reinforces the technical and economic rationale for hybrid RE systems, directly aligning with the multi-scenario analysis conducted in this study.

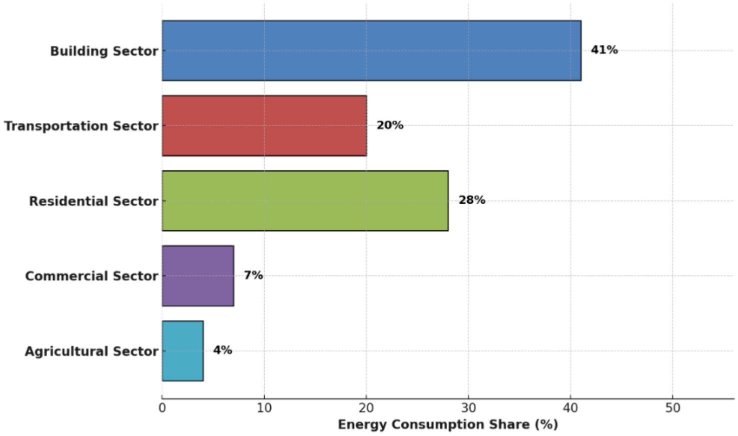

Figure 1. Energy consumption share of various sectors in Iran [2].

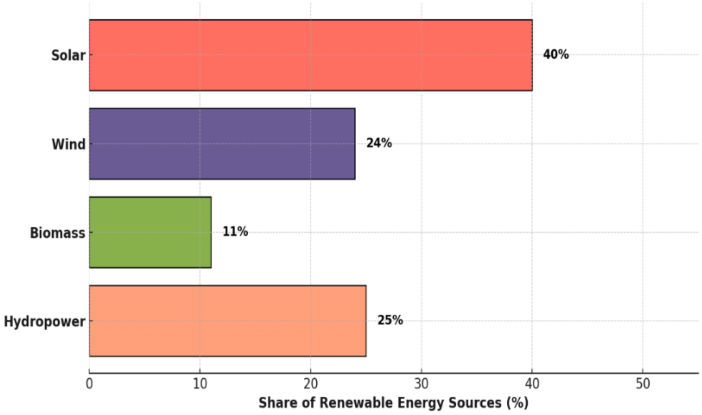

Figure 2. Share of RE sources in power supply in off-grid areas [7].

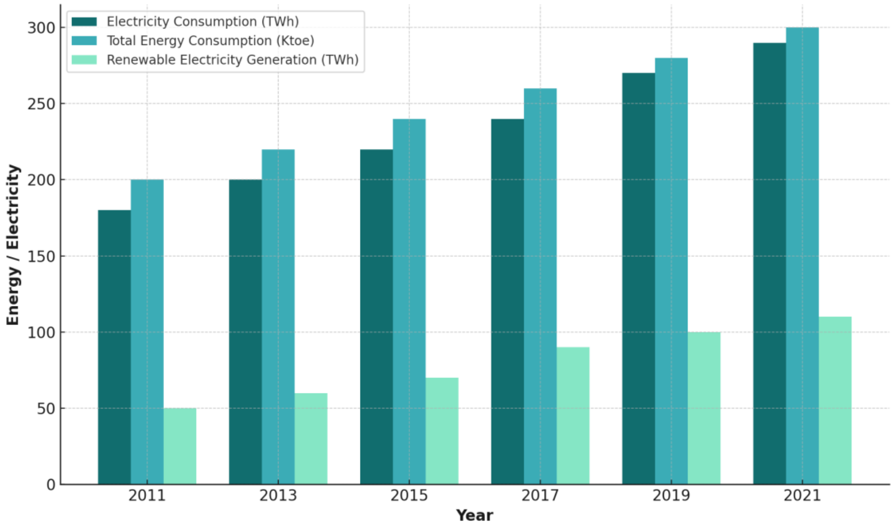

Figure 3. Growth in energy consumption, electricity generation, and the share of renewable electricity production in Iran from 2011 to 2021 [16].

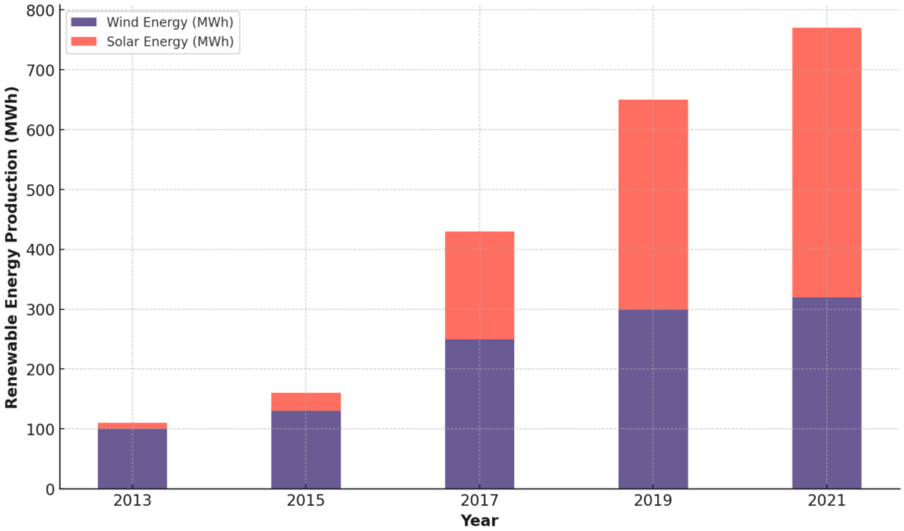

Figure 4. Growth of wind and solar energy in Iran from 2013 to 2021 [16].

A review of existing studies reveals that the use of appropriate materials and construction techniques has a significant impact on a building's energy performance [17-21]. According to the literature review focused on off-grid building energy, categorized in Table 1 based on location, energy sources, methodology, findings, and distinction from the present study, it is evident that no previous research has been conducted on reducing the cost of renewable electricity through physical optimization of an off-grid building. The physical optimizations investigated in this study include external envelope insulation, double-glazed windows, smart control of electrical and thermal systems, and the implementation of green roofs.

Taken together, prior studies consistently report the advantages of hybrid configurations for off-grid applications and the effectiveness of envelope/operational measures in curbing building demand [3-5, 12-15, 22-30]. However, a gap remains regarding how building-level optimizations quantitatively translate into renewable electricity cost metrics (e.g., NPC, LCOE, ROI) in off-grid villas. The present work directly addresses this gap by coupling DesignBuilder-based demand reductions with HOMER-driven techno–economic–environmental analysis, thereby linking envelope/operation measures to electricity cost and emissions outcomes.

2. Study location

In the present work, the cost of RE supply is initially estimated for a sample villa located in the suburbs of Saman city, near the historical Zaman Khan Bridge, in an off-grid condition. This site lies within the jurisdiction of Chaharmahal and Bakhtiari Province, situated in western Iran (Figure 5). Saman, with a population of 14,192 in the year 2016, is located at coordinates 32.45˚N and 50.91˚E. This city is known for its tourism appeal and is situated 22 km northeast of Shahrekord [31]. Passive strategies such as south-facing skylight windows, wall materials adapted to the local climate, and earth-sheltered architectural techniques were employed in the base case design. Subsequently, optimization strategies were applied, and the renewable electricity supply cost was re-evaluated to estimate the potential cost reduction in energy provisioning. As shown in the classification presented in Figure 5, Saman County is located in a relatively cold region. However, based on the Köppen climate classification, and as referenced in Table 2, Saman has a Mediterranean climate characterized by one warm month with an average temperature above 25˚C and one cold month with an average of around 0˚C [32].

Table 1. Analysis of existing research on energy management, reduction, and optimization in off-grid villa homes.

Reference	Location	Renewable energy type	Methodology	Findings	Different from the present work
Zebra et al. [22], 2021	Mozambique	PV, Wind Turbines (WT)	Review-PESTEL	A hybrid system combining RE sources and a DG provided the best scenario.	Different geographical location, no energy optimization performed, different methodology, and objective
Zhang et al. [23], 2022	Various climate zones	Combined Heat and Power (CHP), PV, Solar Thermal Collectors (STC), WT, Battery Energy Storage (BES), and Thermal Energy Storage (TES)	Multi-Objective Genetic Algorithm (MOGA)	MOGA is used to determine the optimal combination of distributed energy resources and the size of each component to minimize system cost and CO2 emissions for various locations.	Different geographical location, no energy optimization performed, different methodology
Pulido et al.[24], 2019	Netherlands	PV, BES, Fuel cell (FC)	DEMkit	A 30 kW solar PV system with a 45 kWh sea salt battery and a 15 kWh glycerol FC operating year-round can remain completely off-grid.	Different geographical location, no energy optimization performed, different methodology, no use of physical tools for solar cost reduction
Cao et al. [25], 2022	China	PVT solar panels, thermal storage tanks, WT, Absorption chiller, Heat pump (HP)	TRNSYS	The highest and lowest unit product cost of the system for January and July were $32.77/GJ and $8.38/GJ, respectively.	Different geographical location, no energy optimization performed, thermal insulation not examined, different objective
Kim et al. [26], 2019	South Korea	PV, STC, HP, TES	TRNSYS	Increasing the solar fraction of the proposed system leads to a primary energy saving of up to 73% compared to a centralized heat pump system.	Different geographical location, no energy optimization performed, different methodology, building envelope optimization not considered
Vichos et al. [27], 2022	Greece	REs, Hydrogen storage	HOMER PRO	The use of RE and energy storage is recommended for maximum energy efficiency.	Different geographical location, no energy optimization performed, different methodology
Muh & tabet [28], 2019	Cameroon	REs	HOMER PRO	A small-scale PV/DG/Hydro/BES, with an energy cost of $0.443/kWh, is identified as the most economically viable system for southern Cameroon.	Different geographical location, no energy optimization performed, different methodology, different objective
Suresh et al. [29], 2020	India	Biogas, Biomass, PV, WT, FC, BES	HOMER	The energy cost is $0.163/kWh.	Different geographical location, no energy optimization performed, different methodology, different objective
Odou et al. [30], 2020	Benin	PV, Diesel generator (DG), BES	HOMER	A hybrid PV/DG/BES (150 kW/62.5 kVA/ 637 kWh) is the most cost-effective optimized system.	Different geographical location, no energy optimization performed, different methodology, different objective
Present work, 2025	Iran	PV, DG, BES	HOMER	A reduction in total NPC (79.5%) and a decrease in CO2 emissions (130 tons/year) compared to the baseline scenario.	-

Table 2. Geographical and Climatic Characteristics of Saman City [32].

Item	Description
Country / Province	Iran / Chaharmahal and Bakhtiari
Distance to provincial capital (Shahrekord)	20 km
Geographical coordinates	50.9117˚ E, 32.4514˚ N
Elevation above sea level	1,996 m
Köppen climate classification	Csa
The coldest month and the recorded temperatures	January holds the record as the coldest month, with an average high temperature of 4.3 ˚C and an average low of -3.8 ˚C.
Warmest Month and Recorded Temperatures	July holds the record as the warmest month, with an average high temperature of 31.6 ˚C and an average low of 18.2 ˚C.

To provide a better understanding of the examined villa's layout, various sectional views of the villa are presented in Figure 6. One noteworthy point is the use of earth-sheltered architecture, a climate-responsive design technique commonly employed in cold regions. It should be noted that the present study is conceptual in nature and based on a hypothetical case study; no physical construction has been carried out. The building is designed for residential use and intended to be occupied throughout the year.

3. Methodology

For modeling and energy analysis of the building in this study, DesignBuilder software was employed. This software allows users to first model the building using architectural plans (base scenario). Then, by applying various building materials (2 scenarios), window configurations (1 scenario), and modifications to occupancy and usage patterns (1 scenario), it is possible to perform detailed energy analyses.

In addition to the base scenario, which is based on climate-adaptive architectural recommendations, five optimization scenarios were investigated:

- Scenario 1: Application of polystyrene insulation in the external envelope of the building.
- Scenario 2: Implementation of a green roof to assess its impact on energy performance.
- Scenario 3: Use of UPVC double-glazed windows to evaluate their effect on thermal losses.
- Scenario 4: Installation of a VRF HVAC system to enhance energy efficiency.
- Scenario 5: A combined scenario integrating all four previous optimizations to assess their cumulative effect.

Figure 7 presents the solar resource input data required by HOMER software for evaluating solar power potential. It also illustrates the software outputs. HOMER, developed by the U.S. National Renewable Energy Laboratory (NREL), is used for the simulation and optimization of hybrid RE systems, ranking configurations based on comprehensive financial analysis [33,34].

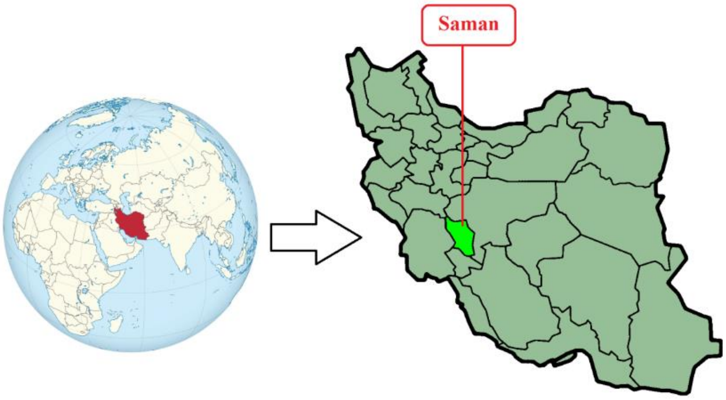

Figure 5. Geographical location of the study area.

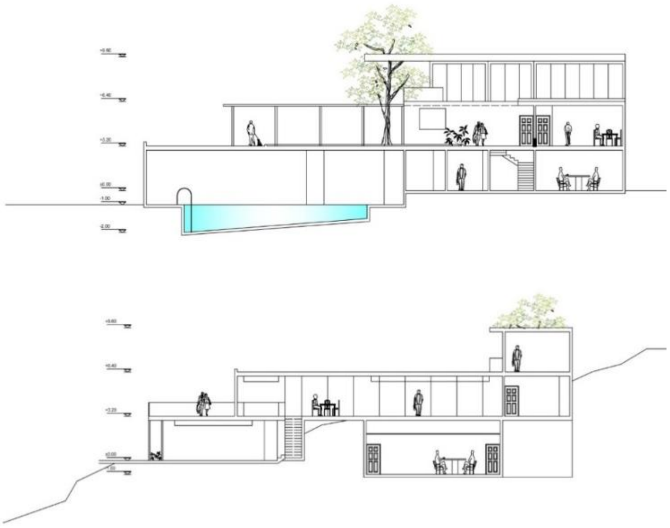

Cross-sections A_A

Cross-sections B_B

Figure 6. Southern and Eastern cross-sections of the investigated building.

The governing equations used in the software, including the power output of PV cells, diesel generator efficiency, BES performance equation, and economic calculations, are presented in Table 3. The schematic of the system investigated in this study is presented in Figure 8. For backup in emergencies, BES storage and a diesel generator are employed, to supply electricity to a residential villa [41].

Table 3. Governing Equations for the Investigated System.

Reference	Parameter	Equation
[35]	Power output from PV cells	$P_{PV} = Y_{PV} \,.\, f_{PV} \,.\, \frac{\overline{H}_T}{\overline{H}_{T,STC}}$
[36]	DG efficiency	$\eta_{gen} = \frac{3.6\ P_{gen}}{\dot{m}_{fuel} .\, LHV_{fuel}}$
[37]	BES performance	$P_{batt,max} = \frac{Min(P_{batt,kbm\ or\ mcr\ or\ mcc})}{\eta_{batt,c}}$
[38]	Net present cost (NPC) calculation	$total\ NPC = \frac{C_{ann,total}}{\frac{i(1+i)^N}{(1+i)^N - 1}}$
[39]	Cost of electricity per kWh	$COE = \frac{C_{ann,total}}{E_{load\ served}}$
[40]	ROI	$\mathrm{ROI} = \frac{\text{cumulative nominal cash flow of (final year} - \text{zero year)}}{\text{lifetime} \times \text{zero year cumulative nominal cash flow}}$

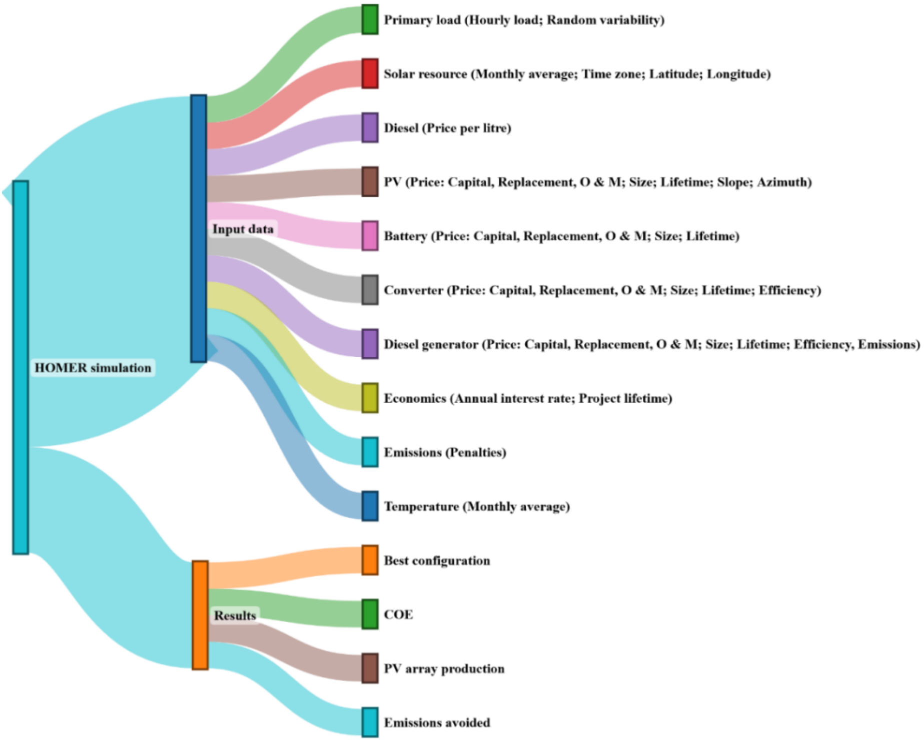

Figure 7. Input and output parameters diagram from HOMER software.

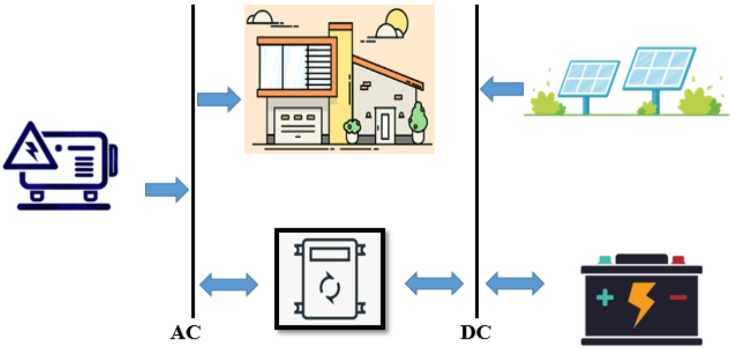

Figure 8. Schematic Diagram of the System Investigated in the Present Study.

In a RE system, management of surplus electricity, capacity factor, and electrical losses is critically important. Optimizing these factors can significantly enhance system efficiency and reduce costs, ultimately resulting in more sustainable and economically viable energy production.

Surplus electricity refers to the electrical energy that remains after meeting the consumers' demand. It can be either fed into the grid or stored in energy storage systems. In RE systems, this is particularly significant because power generation from sources such as solar and wind is variable and may at times exceed demand.

The capacity factor is defined as the ratio of actual energy produced to the maximum possible output at the rated capacity of the equipment. It reflects the efficiency and productivity of RE systems.

Electrical losses refer to the energy lost during the transmission and distribution of electricity due to resistance in wires and equipment. These losses may result from various factors, including conductor resistance, equipment quality, and unbalanced loads.

4. Input data

The simulation requires a comprehensive set of technical, cost, and climatic inputs to ensure accurate modeling. Table 4 summarizes the key equipment specifications and associated economic parameters, including capital, replacement, and operating costs, as well as performance characteristics such as lifetime, efficiency, and derating factors.

In addition to these equipment-specific data, Figure 9 presents the monthly average global horizontal radiation (GHI) and clearness index for the study site. The annual average GHI is 5.06 kWh/m^2/day, while the clearness index averages 0.59, indicating a generally favorable solar resource with minor seasonal variability. Higher GHI values are observed from May to August, coinciding with peak system generation potential, whereas lower values occur during winter months, which can impact battery depth-of-discharge cycles and diesel generator utilization.

The cost of diesel fuel was set at $0.006 per liter [44], the project lifetime at 25 years, and the real annual interest rate at 18%. Emission penalties were included to internalize environmental costs: $3.10/ton CO_2, $57/ton CO, $560/ton SO_2, and $184/ton NO_x [45]. These values directly influence the economic optimization performed by HOMER.

Figures 10 through 15 display the hourly electricity demand profiles for the baseline and five optimization scenarios. These profiles incorporate stochastic variability, modeled with a 15% daily and 20% hourly randomness factor [46], to account for real-world fluctuations in residential load.

- Figure 10 (Baseline): The demand profile shows high winter peaks exceeding 150 kW, primarily due to electric heating loads, and moderate summer loads. This pattern reflects poor building envelope performance and inefficient HVAC systems.
- Figure 11 (Scenario 1 – Polystyrene Insulation): Peak winter demand is reduced to approximately 120 kW, indicating substantial thermal load reduction from improved wall and roof insulation. Summer demand remains largely unchanged, as cooling loads are not directly impacted.
- Figure 12 (Scenario 2 – Green Roof): Similar winter demand reduction is observed, with an additional slight decrease in summer cooling demand due to enhanced roof thermal resistance and heat rejection.
- Figure 13 (Scenario 3 – UPVC Windows): Both winter and summer peaks are moderately reduced compared to the baseline, owing to minimized air infiltration and improved thermal performance of the glazing.
- Figure 14 (Scenario 4 – VRF HVAC): This scenario yields the largest winter demand reduction among single-measure cases, dropping peak loads to around 80 kW. The high seasonal efficiency of VRF systems significantly decreases both heating and cooling electricity requirements.
- Figure 15 (Scenario 5 – All Measures Combined): The integrated scenario produces the most pronounced demand reduction, with peaks rarely exceeding 35 kW in winter and under 15 kW in summer. This combination of measures results in optimal thermal performance and minimized HVAC energy use.

By analyzing these demand profiles in conjunction with the solar resource data, HOMER's optimization algorithm determines the optimal sizing of PV, BES, and DG components. Lower and more stable demand patterns (as in Scenario 5) reduce PV capacity requirements, extend battery life, and minimize diesel operation, thereby lowering both net present cost (NPC) and lifecycle emissions.

Table 4. Required Simulation Data for HOMER.

Equipment	Price ($)			Size (kW)	Technical information
	Capital	Replacement	Operating and Maintenance		
PV [42]	350	350	10	0-800	Lifetime: 25 years, Derating factor: 80%, Slope = Azimuth [222]
BES [42]	174	174	5	0-1000	Type: Trojan T-105, Lifetime: 845 kWh
Converter [42]	138	138	10	0-800	Lifetime: 15 years, Efficiency: 95%
DG [43]	200	200	0.5	0-800	Lifetime: 15000 hr, Efficiency: 31% CO factor: 6.5 g/L, Destination of fuel Carbon: $CO_2 =$ 99.5% , $CO = 0.4\%$

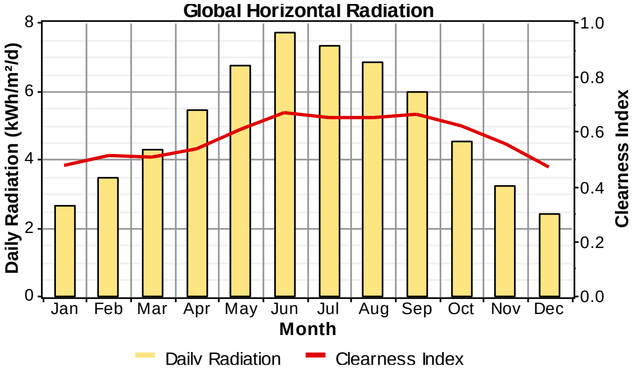

Figure 9. Monthly Average Solar Irradiance.

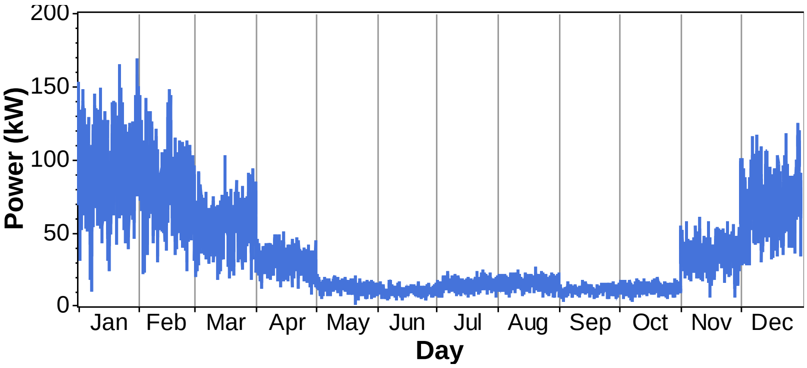

Figure 10. Annual Electricity Consumption Profile for the Base Scenario.

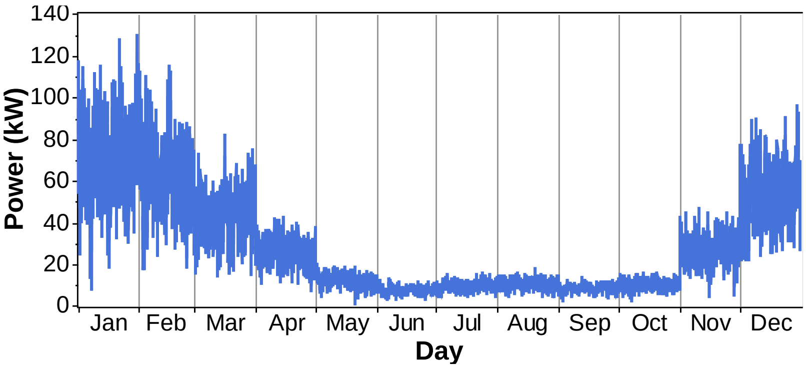

Figure 11. Annual Electricity Consumption Profile for Scenario 1.

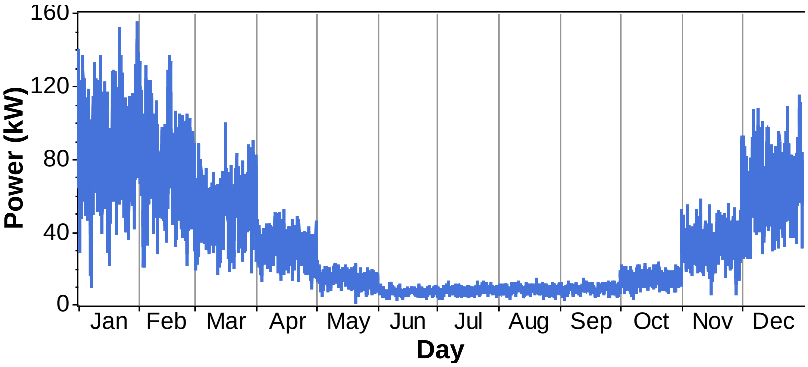

Figure 12. Annual Electricity Consumption Profile for Scenario 2.

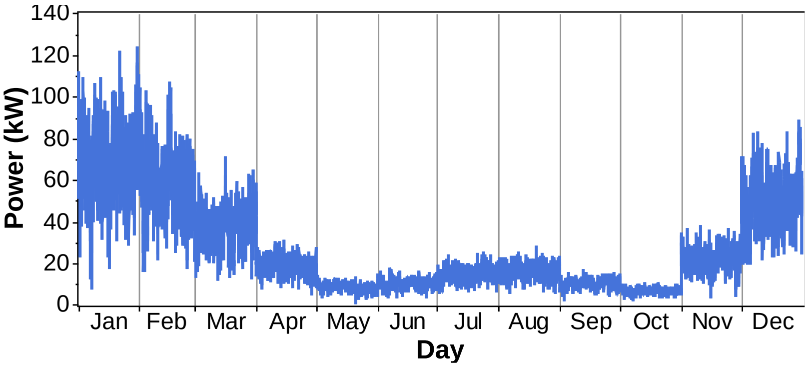

Figure 13. Annual Electricity Consumption Profile for Scenario 3.

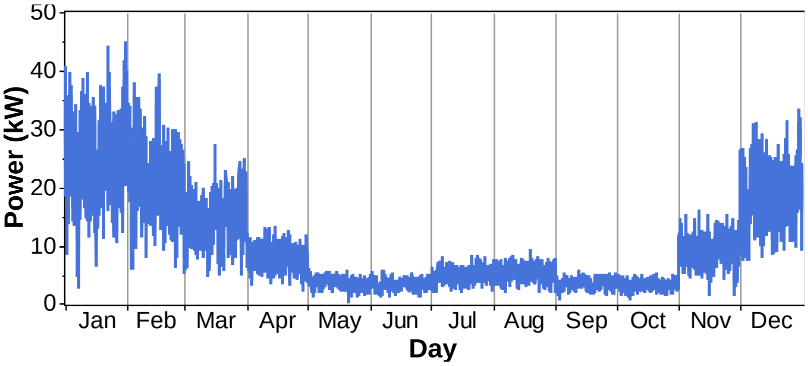

Figure 14. Annual Electricity Consumption Profile for Scenario 4.

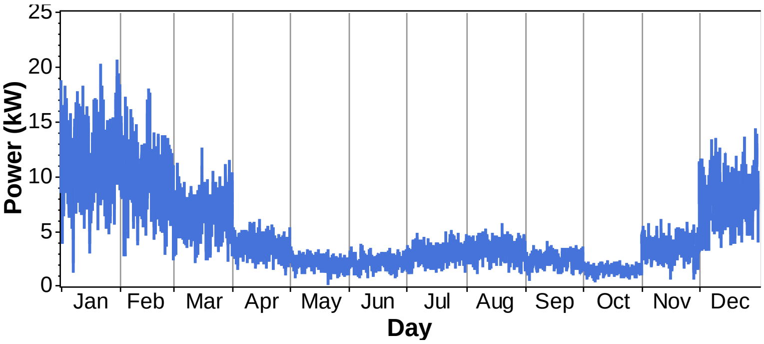

Figure 15. Annual Electricity Consumption Profile for Scenario 5.

5. Results

The simulation results for the base case of the climate-responsive villa (the selected case study), along with the four energy improvement scenarios and the optimized case (combined Scenario 1 to 4), are presented in Table 5. The analysis shows that the diesel generator and power converter capacities are identical in all scenarios, set at 100 kW, while the primary differences lie in the number of PV panels and batteries. The lowest PV capacity, at 100 kW, and the lowest number of batteries, at 30 units, both occur in Scenario 5, the optimized configuration.

From an economic perspective, an interesting observation is that as the demand for electricity decreases, the total NPC decreases; however, the cost per kWh of generated electricity increases. In other words, the higher the electricity demand, the lower the unit cost of electricity. The highest total NPC occurs in the base scenario, while the highest unit electricity cost appears in Scenario 5. Through the implemented optimizations (Scenarios 1–5), the NPC is reduced from $947,243 to a range of $896,305–$193,796, while the cost of electricity per kWh increases from $0.557 to a range of $0.557–$0.867. This scale effect is consistent with HOMER-based case studies in off-grid settings, where greater effective demand and hybridization typically yield lower LCOE due to improved asset utilization [29,30].

Present results confirm this trend: while demand-side measures compress NPC substantially, unit costs can rise when fixed components are amortized over a smaller annual energy throughput, a nuance often underemphasized in purely supply-side studies. The magnitudes and directionality of these improvements accord with prior building-scale studies on envelope upgrades and efficient HVAC, which document significant reductions in heating/cooling loads and total energy use [12-15]. By explicitly propagating these demand reductions into a hybrid off-grid sizing/dispatch model (HOMER), the present results extend this line of work to quantify downstream impacts on NPC, LCOE, and ROI.

Regarding renewable electricity generation, depending on the number of PV panels, annual production ranges from 157,483 to 629,930 kWh, covering 77% to 97% of the total electricity demand. As the system is off-grid, a significant amount of surplus electricity is generated annually, the highest being 434,096 kWh/year in Scenario 3, and the lowest being 115,181 kWh/year in Scenario 5. The share of surplus electricity ranges from 44.4% to 71.1%, with Scenario 5 showing the lowest and the base scenario showing the highest surplus. On high-solar days, a significant portion of this surplus electricity could be utilized for auxiliary applications such as hydrogen production through electrolysis, which could further enhance the system's overall energy autonomy and economic value. This observation is in line with studies that integrate power-to-hydrogen pathways in off-grid or net-zero contexts, where surplus PV is routed to electrolysis to enhance autonomy and provide seasonal storage [11,34,41]. Our findings thus reinforce the sector-coupling potential reported in the literature and indicate a practical avenue for valorizing surplus generation in high-irradiance periods.

The capacity factor for the PV system remains at 18% across all scenarios. The highest capacity factors for the diesel generator, inverter, and rectifier are 16.5% (base), 22.1% (base), and 3.1% (Scenario 2), respectively. In Scenarios 1 and 3, the rectifier is used minimally, resulting in a zero capacity factor.

Losses in the BES, inverter, and rectifier systems are also analyzed. The lowest BES losses, at 3,460 kWh/year, occur in Scenario 5 due to the reduced number of batteries. Fewer batteries not only lower initial investment costs but also reduce storage-related energy losses by limiting the number of charge/discharge cycles, as seen in the substantially lower BES loss values in Scenario 5 compared to all other configurations. The highest BES losses, at 19,789 kWh/year, are observed in the base scenario, which uses 1,000 batteries, the highest among all configurations. Inverter and rectifier losses, which are directly related to their capacity factors, fall within 2,062–10,169 kWh/year and 6–1,450 kWh/year, respectively.

In terms of emissions, which result from the operation of the diesel generator, lower energy demand leads to lower emissions. The highest total emissions, at around 136 tons/year, occur in the base case, while the lowest, at 6.3 tons/year, occur in Scenario 5. The generator operating hours, which correlate with diesel fuel consumption, range from 1,786 hours/year (base) to 150 hours/year (Scenario 5).

A particularly important and unexpected result relates to the diesel generator dispatch strategy. In the base scenario, Scenario 2, and Scenario 4, the generator operates in cycle charging mode, while in Scenarios 1, 3, and 5, it operates in load following mode. In cycle charging mode, the generator runs at full capacity and stores surplus power in batteries, increasing rectifier activity and consequently its losses, clearly observed in the results. In load following mode, the generator only produces as much electricity as needed, avoiding excess generation and BES charging, thus minimizing the need for rectifier operation. In Scenario 5, the load following dispatch strategy allows the diesel generator to operate only when strictly necessary, preventing unnecessary charging of the battery bank. This operational behavior is visible in Figure 16, where generator activity is minimal despite fluctuations in load and PV generation, resulting in both reduced operating hours and lower associated emissions. Such behavior is consistent with HOMER-driven analyses in off-grid hybrids, where load-following logic curtails unnecessary charging cycles, shortens generator operating hours, and reduces associated emissions compared to cycle-charging regimes [29,30]. The pattern observed here (minimal generator activity in Scenario 5) corroborates these operational advantages.

Analysis of the ROI, a key financial indicator in RE studies, shows that Scenario 5, which combines all optimizations, has the best performance, with an ROI of 434%, equivalent to a payback period of 0.234 years. The least favorable scenario in terms of ROI is Scenario 1, with 267%.

Figure 16 illustrates the system performance in Scenario 5, identified as the most technically, economically, and energy-efficient configuration, during the first week of January. As shown, on days with high solar radiation and sufficient BES charge, or when the electricity demand is low, the diesel generator is either not used or minimally engaged. On January 4 and 5, due to low solar radiation and insufficient BES charge, the diesel generator operates at approximately 30 kW to meet demand. The sequential supply of demand is evident in the figure: during daylight, PV production is prioritized; in the absence of solar generation, the system switches to battery discharge, and only when the battery state of charge drops below the threshold does the diesel generator engage. This layered dispatch minimizes fuel consumption and emissions. Figure 16 also illustrates the sequential supply of demand, PV priority during daylight, followed by battery discharge, and DG engagement only below a SOC threshold, which is a canonical feature of efficient off-grid hybrid operation reported in the literature [27,29,30]. This layered dispatch underpins the low DG hours and emissions achieved in the optimized scenario.

Table 5. Simulation Results for Different Scenarios.

	Equipment								Capacity factor (%)			
Scenario	PV (kW)	DG (kW)	BES	Converter (kW)	NPC ($)	LCOE ($/kWh)	PV production (kWh/yr)	Excess electricity (kWh/yr)	PV	DG	Inverter	Rectifier
Base	300	100	1000	100	947243	0.557	472447	274091	18	16.5	22.1	2.9
Polystyrene	400	100	1000	100	780205	0.582	629930	428265	18	7.68	20.3	0
Green roof	300	100	1000	100	896305	0.572	472447	285534	18	14.9	21.1	3.1
UPVC	400	100	1000	100	732224	0.586	629930	434096	18	6.38	19.7	0
VRF	200	100	700	100	349401	0.742	314965	229090	18	1.52	9.3	0.9
Optimized	100	100	300	100	193796	0.867	157483	115181	18	0.51	4.5	0.3

Table 5 continued

	Losses (kWh/year)			Emission (kg/year)						
Scenario	EBS	Inverter	Rectifier	CO2	CO	SO2	NOx	ROI (%)	Dispatch strategy	DG (hour)
Base	19789	10169	1318	132582	327	266	2920	288	CC	1786
Polystyrene	13383	9376	7	69151	171	139	1523	267	LF	1180
Green roof	19278	9749	1450	119983	296	241	2643	291	CC	1621
UPVC	13279	9090	6	58148	144	117	1281	270	LF	1013
VRF	8052	4275	400	13359	33	26.8	294	208	CC	219
Optimized	3460	2062	137	6122	1501	1203	135	434	LF	150

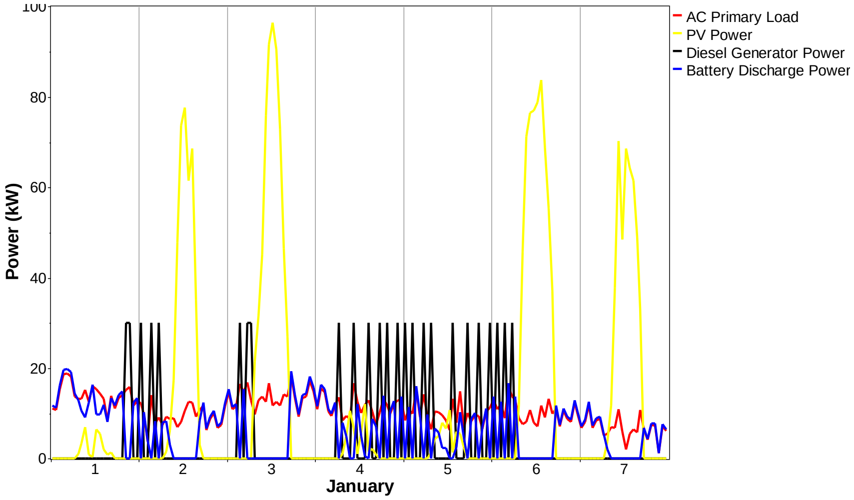

Figure 16. System Performance in Scenario 5 During the First Week of January.

6. Discussion

The primary objective of this study was to quantitatively assess how building-level energy efficiency measures influence the techno–economic–environmental performance of an off-grid solar–battery–diesel generator system in a climate-compatible villa. The findings strongly support this objective by demonstrating that demand-side optimizations, such as advanced insulation, efficient glazing, green roofing, and VRF-based HVAC, can substantially reduce the net present cost, lower emissions, and improve ROI compared to the baseline configuration. These outcomes confirm the initial hypothesis that integrated building optimization strategies not only reduce energy demand but also enhance the cost-effectiveness and environmental performance of renewable energy systems in off-grid residential applications. Additionally, the observed trade-off between reduced total costs and increased unit electricity costs in low-demand scenarios provides a nuanced refinement to the initial assumptions, highlighting the importance of balancing demand reduction with optimal capacity utilization in system design.

The results of this study offer several practical implications for stakeholders involved in off-grid and hybrid renewable energy deployment. For policymakers, the demonstrated potential of combining building envelope improvements and high-efficiency HVAC systems with a hybrid PV–DG–BES configuration, yielding up to 79.5% reduction in total NPC and approximately 130 tons/year reduction in emissions, provides strong justification for targeted policy instruments such as subsidies, tax incentives, and low-interest financing schemes that jointly address demand- and supply-side optimization.

For grid operators and energy planners, although the analysis focuses on an off-grid case, operational strategies such as load-following dispatch and surplus PV utilization for hydrogen production are transferable to weak-grid and microgrid contexts, where they can reduce generator runtime, improve asset utilization, and enhance system resilience under high renewable penetration. For building designers, developers, and EPC contractors, the quantified linkage between building-level energy optimization and renewable electricity cost metrics (LCOE, ROI) enables more informed investment decisions, demonstrating that optimal sizing of PV arrays and battery storage not only prevents over-dimensioning but also reduces storage-related losses while increasing energy autonomy in remote locations. Finally, a cross-cutting insight emerges: while demand-side measures substantially reduce total system costs, they may also increase unit electricity cost when fixed-capacity components are amortized over a smaller annual energy throughput, highlighting the importance of integrated techno–economic optimization in design practice.

The findings of this study have broader implications that extend beyond the specific case of the climate-responsive villa examined. For grid operators, the results indicate that implementing building-level energy efficiency measures can reduce the required capacity of distributed generation or off-grid systems, thereby alleviating stress on generation and storage infrastructure, improving peak load management, and enhancing network resilience. For policymakers, the study provides both quantitative and qualitative evidence to support the formulation of incentives, building standards, and supportive programs that facilitate the effective integration of renewable energy in the residential sector, particularly in remote or rural areas. For researchers, the integrated framework employed, combining consumption modeling via DesignBuilder with techno–economic–environmental assessment using HOMER, is adaptable to various climates, load profiles, and technologies (e.g., hybrid wind–solar systems or hydrogen production scenarios) and can serve as a decision-support tool at different scales. Overall, the model is transferable to regions with diverse energy resource profiles, subsidy policies, and levels of grid connectivity, making it suitable for international comparative studies and the strategic design of energy transition pathways across varied contexts.

7. Future works

This study, while offering valuable insights into the techno–economic–environmental impacts of building energy efficiency measures in off-grid PV–battery–diesel systems, is subject to several limitations.

First, the analysis relies on simulation-based results from DesignBuilder and HOMER, which assume idealized operational conditions, fixed component efficiencies, and static economic parameters; real-world performance may deviate due to degradation, partial shading, equipment downtime, or fluctuating fuel prices [47,48].

Second, the study focuses on a single case study in the climate of Saman, Chaharmahal and Bakhtiari Province, Iran; the generalizability of the results to other climates, building typologies, and load profiles requires additional validation [49,50].

Third, the surplus electricity utilization pathway (e.g., hydrogen production) was discussed conceptually but not modeled in detail; including techno–economic modeling of such sector-coupling strategies could provide more precise estimates of benefits [51,52].

Finally, the study did not perform an uncertainty analysis for key input parameters such as PV yield, diesel price volatility, or battery degradation rate, which could influence the robustness of the reported NPC, LCOE, and ROI values [53,54].

Future research should address these limitations by incorporating experimental validation [55], expanding the scope to multiple climate zones and hybrid configurations [56,57], modeling surplus utilization pathways in detail [58], and applying sensitivity/uncertainty analysis to strengthen the reliability of the conclusions [59,60].

Future work could adapt the causality analysis methodologies presented in [61-63] to the energy domain, enabling a clearer attribution of the effects of individual building optimization measures on system sizing, cost, and emissions. Approaches from [61] and [62] could help model non-linear and probabilistic relationships between demand reduction strategies and hybrid system performance, while techniques from [63] could improve robustness by accounting for uncertainty in climatic and load variations. Integrating these methods with the current DesignBuilder–HOMER framework would provide deeper, more generalizable insights for off-grid energy system planning.

Future research could integrate the current off-grid building optimization framework with advanced Distribution Network Expansion Planning (DNEP) methodologies to simultaneously assess demand-side and supply-side impacts. Multi-objective optimization approaches that explicitly incorporate uncertainties in electricity price and load demand, as demonstrated in [64-66], could enable more comprehensive scenario evaluation. The inclusion of risk-based performance metrics such as flexibility and robustness, as introduced in [64,65], would further allow assessment of the resilience of off-grid systems under fluctuating renewable resources and demand profiles. Moreover, adopting integrated planning of medium-voltage (MV) and low-voltage (LV) networks in the presence of distributed generators and renewable sources, as developed in [66], could facilitate joint evaluation of technical and economic impacts across multiple infrastructure layers. Finally, the comprehensive review of DNEP challenges and future trends in [67] highlights promising directions such as incorporating energy storage systems, refining solution techniques for non-linear/non-convex problems, and modelling stakeholder conflicts, all of which could be adapted to expand the scope and applicability of the present model.

8. Conclusions

Implementing effective strategies to reduce energy consumption not only helps protect the environment but also enhances the sustainability and reduces the energy costs of residential buildings. Despite their significance, the direct influence of these strategies on lowering the cost of renewable electricity has not been thoroughly studied. The present study addresses this gap by examining the impact of four energy-saving strategies on the cost of a solar system in a climate-adaptive villa located in Saman, Chaharmahal and Bakhtiari Province, Iran. The energy analysis of these strategies and the evaluation of the solar system's performance were carried out using DesignBuilder v6.1.0.6 and HOMER v2.81, respectively. The energy simulations in DesignBuilder span one year, while HOMER provides a 25-year energy-economic-environmental analysis. Six scenarios were investigated in total: Scenario 1, a climate-responsive design without optimization; Scenario 2, applying polystyrene insulation to the envelope; Scenario 3, implementing a green roof; Scenario 4, installing UPVC windows; Scenario 5, incorporating a VRF air conditioning system; and Scenario 6, which combines Scenarios 2 to 5. This study confirms the economic and environmental value of implementing energy-saving strategies in climate-adaptive buildings and provides a practical foundation for future decision-making in this domain.

- The solar PV capacity in the off-grid system was 400 kW in Scenarios 2 and 4, 300 kW in Scenarios 1 and 3, 200 kW in Scenario 5, and the lowest, 100 kW, in Scenario 6.

- In all scenarios, a 100 kW diesel generator was used as a backup power source, remaining constant across all configurations.

- The number of batteries used was 1,000 units in Scenarios 1 through 4, 700 units in Scenario 5, and only 300 units in the most optimized case, Scenario 6.

- The total NPC of the solar system ranged from $947,243 in Scenario 1 (the base case) to $193,796 in Scenario 6 (the optimized case), indicating a significant reduction in total system cost with energy-saving strategies.

- The cost of electricity increased as energy demand decreased, ranging from $0.557/kWh in Scenario 1 to $0.867/kWh in Scenario 6, highlighting the inverse relationship between total electricity consumption and the unit cost of renewable electricity.

- The solar system was capable of supplying between 77% and 97% of the total electricity demand across the scenarios, with surplus electricity generation ranging from 44.4% to 71.1% of total output, a notable consequence of off-grid system design.

- Annual system losses were also considerable, varying from 31,276 kWh in Scenario 1 to just 5,659 kWh in Scenario 6, driven primarily by the number of batteries and inverter utilization.

- Emissions from diesel generator operation ranged from approximately 136.1 tons/year in the base scenario to as low as 6.3 tons/year in the fully optimized Scenario 6, showing a strong correlation between system design and environmental performance.

- The optimal generator dispatch strategy varied by scenario: Scenarios 1, 3, and 5 followed a cycle charging strategy, while Scenarios 2, 4, and 6 followed a load following approach, which significantly influenced both generator usage and energy losses.

References

[1] O. Rahmani, S. Rezania, et al., "An Overview of Household Energy Consumption and Carbon Dioxide Emissions in Iran," *Processes*, vol. 8, no. 8, 994, 2020.
[2] A. I. Hassane, D. H. Didane, et al., "Comparative Analysis of Hybrid Renewable Energy Systems for Off-Grid Applications in Chad," *International Journal of Renewable Energy Development*, vol. 11, no. 1, pp. 49–62, 2021.
[3] H. Omrany, R. Chang, et al., "A Bibliometric Review of Net Zero Energy Building Research 1995–2022," *Energy and Buildings*, vol. 262, 111996, 2022.
[4] A. Guerello, S. Page, G. Holburn, and M. Balzarova, "Energy for Off-Grid Homes: Reducing Costs Through Joint Hybrid System and Energy Efficiency Optimization," *Energy and Buildings*, vol. 207, 109478, 2020.
[5] A. Ahmed, T. Ge, et al., "Assessment of the Renewable Energy Generation Towards Net-Zero Energy Buildings: A Review," *Energy and Buildings*, vol. 256, 111755, 2022.
[6] P. G. Munro, and S. Samarakoon, "Off-Grid Electrical Urbanism: Emerging Solar Energy Geographies in Ordinary Cities," *Journal of Urban Technology*, vol. 30, no. 2, pp. 127–149, 2022.
[7] B. Abdullah, and S. Ameen, "Off-Grid Photovoltaic System for a Villa at AVRO City in Duhok," *Al-Rafidain Engineering Journal (AREJ)*, vol. 28, no. 1, pp. 14–23, 2023.
[8] M. T. Castro, J. D. A. Pascasio, L. L. Delina, P. H. M. Balite, and J. D. Ocon, "Techno-Economic and Financial Analyses of Hybrid Renewable Energy System Microgrids in 634 Philippine Off-Grid Islands: Policy Implications on Public Subsidies and Private Investments," *Energy*, vol. 257, 124599, 2022.
[9] H. Sadeghi, D. Toghraie, M. Moazzami, M. M. Rezaei, and M. Dolatshahi, "Integrated Long-Term Planning of Conventional and Renewable Energy Sources in Iran's Off-Grid Networks," *Renewable Energy*, vol. 182, pp. 134–162, 2022.
[10] A. Mirzakhani, and I. Pishkar, "Finding the Best Configuration of an Off-Grid PV-Wind-Fuel Cell System with Battery and Generator Backup: A Remote House in Iran," *Journal of Solar Energy Research*, vol. 8, no. 2, pp. 1380–1392, 2023.
[11] P. Guo, F. Musharavati, and S. M. Dastjerdi, "Design and Transient-Based Analysis of a Power to Hydrogen (P2H2) System for an Off-Grid Zero Energy Building with Hydrogen Energy Storage," *International Journal of Hydrogen Energy*, vol. 47, no. 62, pp. 26515–26536, 2022.
[12] J. Riahi Zaniani, S. Taghipour Ghahfarokhi, M. Jahangiri, and A. Alidadi Shamsabadi, "Design and Optimization of Heating, Cooling and Lightening Systems for a Residential Villa at Saman City, Iran," *Journal of Engineering, Design and Technology*, vol. 17, no. 1, pp. 41–52, 2019.
[13] R. Feng, J. Li, and X. Li, "Performance Study of External Wall Insulation and a Hybrid Energy Supply System for a Rural Residential Building," *Journal of Energy Engineering*, vol. 142, no. 4, 2016.
[14] B. Adly, and T. El-Khouly, "Combining Retrofitting Techniques, Renewable Energy Resources and Regulations for Residential Buildings to Achieve Energy Efficiency in Gated Communities," *Ain Shams Engineering Journal*, vol. 13, no. 6, 101772, 2022.
[15] M. Jahangiri, M. Khorsand Dehkordi, and S. Khorsand Dehkordi, "Potential Measurement of Electricity Supply," *International Journal of Low-Carbon Technologies*, vol. 18, pp. 1067–1076, 2023.

[16] Enerdata, "Iran Energy Market Report".

[17] T. Dong, S. Yin, and N. Zhang, "New Energy-Driven Construction Industry: Digital Green Innovation Investment Project Selection of Photovoltaic Building Materials Enterprises Using an Integrated Fuzzy Decision Approach," *Systems*, vol. 11, no. 1, 11, 2022.

[18] E. Heydari, J. Mehdinezhad, and P. Doulabi, "Strategic Principles of Designing the Form of a Residential Building in Bushehr Based on Reducing Energy Consumption," *Karafan Quarterly Scientific Journal*, vol. 18, no. 4, pp. 345–361, 2022.

[19] A. Shayanian, F. Mozaffari Qhadikolaei, and A. Pahlavan, "The Effect of Materials in Reducing Energy Consumption in Atrium Commercial Centers in the North and Center of Tehran Province," *Karafan Quarterly Scientific Journal*, vol. 18, no. 4, pp. 429–440, 2022.

[20] C. Z. Li, L. Zhang, et al., "Advances in the Research of Building Energy Saving," *Energy and Buildings*, vol. 254, 111556, 2022.

[21] S. H. Neshat Safavi, H. Zolfagharzadeh, M. Mafi, and A. Esfandiari, "Optimization the Position of the Windows for Improved Natural Ventilation, Thermal Comfort and Daylight in Yazd City," *Karafan Quarterly Scientific Journal*, vol. 18, no. 4, pp. 395–410, 2022

[22] E. I. Come Zebra, H. J. van der Windt, G. Nhumaio, and A. P. Faaij, "A Review of Hybrid Renewable Energy Systems in Mini-Grids for Off-Grid Electrification in Developing Countries," *Renewable and Sustainable Energy Reviews*, vol. 144, 111036, 2021.

[23] J. Zhang, H. Cho, and P. J. Mago, "Design and Optimization of Integrated Distributed Energy Systems for Off-Grid Buildings," *Journal of Energy Resources Technology*, vol. 144, no. 7, 2021.

[24] D. F. Quintero Pulido, M. V. Ten Kortenaar, J. L. Hurink, and G. J. Smit, "The Role of Off-Grid Houses in the Energy Transition with a Case Study in the Netherlands," *Energies*, vol. 12, no. 10, 2033, 2019.

[25] Y. Cao, H. A. Dhahad, et al., "Development and Transient Performance Analysis of a Decentralized Grid-Connected Smart Energy System Based on Hybrid Solar-Geothermal Resources; Techno-Economic Evaluation," *Sustainable Cities and Society*, vol. 76, 103425, 2022.

[26] M. Kim, D. Kim, J. Heo, and D. Lee, "Techno-Economic Analysis of Hybrid Renewable Energy System with Solar District Heating for Net Zero Energy Community," *Energy*, vol. 187, 115916, 2019.

[27] E. Vichos, N. Sifakis, and T. Tsoutsos, "Challenges of Integrating Hydrogen Energy Storage Systems into Nearly Zero-Energy Ports," *Energy*, vol. 241, 122878, 2022.

[28] E. Muh, and F. Tabet, "Comparative Analysis of Hybrid Renewable Energy Systems for Off-Grid Applications in Southern Cameroons," *Renewable Energy*, vol. 135, pp. 41–54, 2019.

[29] V. Suresh, M. M., and R. Kiranmayi, "Modelling and Optimization of an Off-Grid Hybrid Renewable Energy System for Electrification in a Rural Areas," *Energy Reports*, vol. 6, pp. 594–604, 2020.

[30] O. D. T. Odou, R. Bhandari, and R. Adamou, "Hybrid Off-Grid Renewable Power System for Sustainable Rural Electrification in Benin," *Renewable Energy*, vol. 145, pp. 1266–1279, 2020.

[31] Wikipedia, "Saman, Chaharmahal and Bakhtiari".

[32] Encyclopædia Britannica, "Mediterranean Climate".

[33] Y. Yousefi, M. Jahangiri, A. Alidadi Shamsabadi, and A. Raeesi Dehkordi, "Designing a Mediator Space and the Study of Its Effect on the Energy Consumption of a Residential Building Using EnergyPlus Software in Savadkuh, Iran," *Journal of Engineering, Design and Technology*, vol. 17, no. 4, pp. 833–846, 2019.

[34] M. Rezaei, M. Jahangiri, and A. Razmjoo, "Utilization of Rooftop Solar Units to Generate Electricity and Hydrogen: A Technoeconomic Analysis," *International Journal of Photoenergy*, vol. 2021, pp. 1–12, 2021.

[35] M. H. Razavi Dehkordi, A. H. Meghdadi Isfahani, et al., "Energy-Economic-Environmental Assessment of Solar-Wind-Biomass Systems for Finding the Best Areas in Iran: A Case Study Using GIS Maps," *Sustainable Energy Technologies and Assessments*, vol. 53, 102652, 2022.

[36] M. Jahangiri, Y. Yousefi, et al., "Techno–Econo–Enviro Energy Analysis, Ranking and Optimization of Various Building-Integrated Photovoltaic (BIPV) Types in Different Climatic Regions of Iran," *Energies*, vol. 16, no. 1, 546, 2023.

[37] M. Jahangiri, M. Khalili Geshnigani, A. Beigi Kheradmand, and R. Riahi, "Meeting the Hospital Oxygen Demand with a Decentralized Autonomous PV System: Effect of PV Tracking Systems," *Iranian Journal of Science and Technology, Transactions of Electrical Engineering*, vol. 47, no. 2, pp. 601–615, 2022.

[38] A. Mostafaeipour, M. Qolipour, et al., "A Novel Integrated Approach for Ranking Solar Energy Location Planning: a Case Study," *Journal of Engineering, Design and Technology*, vol. 19, no. 3, pp. 698–720, 2020.

[39] A. Mostafaeipour, M. Jahangiri, et al., "Impact of Different Solar Trackers on Hydrogen Production: A Case Study in Iran," *International Journal of Photoenergy*, vol. 2022, pp. 1–15, 2022.

[40] S. Shahgholian, M. Taheri, and M. Jahangiri, "Investigating the Cost-Effectiveness of Solar Electricity Compared to Grid Electricity in the Capitals of Middle Eastern Countries: A Residential Scale Case Study," *International Journal of Photoenergy*, vol. 2023, pp. 1–19, 2023.

[41] M. Jahangiri, M. Rezaei, et al., "Prioritization of Solar Electricity and Hydrogen Co-Production Stations Considering PV Losses and Different Types of Solar Trackers: A TOPSIS Approach," *Renewable Energy*, vol. 186, pp. 889–903, 2022.

[42] M. Jahangiri, A. Mostafaeipour, H. U. Rahman Habib, H. Saghaei, and A. Waqar, "Effect of Emission Penalty and Annual Interest Rate on Cogeneration of Electricity, Heat, and Hydrogen in Karachi: 3E Assessment and Sensitivity Analysis," *Journal of Engineering*, vol. 2021, pp. 1–16, 2021.

[43] G. R. Aboutalebi, M. Khalili, and M. Jahangiri, "Effect of Temperature Coefficient and Efficiency of PV Technologies on 3E Performance and Hydrogen Production of On-Grid PV System in a Very Hot and Humid Climate," *Journal of Solar Energy Research*, vol. 8, no. 4, pp. 1715–1727, 2023.

[44] GlobalPetrolPrices.com, "Diesel Prices".

[45] R. Keshavarzi, and M. Jahangiri, "Synergizing Wind, Solar, and Biomass Power: Ranking Analysis of Off-Grid System for Different Weather Conditions of Iran," *Energy Engineering*, vol. 121, no. 6, pp. 1381–1401, 2024.

[46] S. Shahgholian, M. Taheri, and M. Jahangiri, "Investigating the Cost-Effectiveness of Solar Electricity Compared to Grid Electricity in the Capitals of Middle Eastern Countries: A Residential Scale Case Study," *International Journal of Photoenergy*, vol. 2023, pp. 1–19, 2023.

[47] Y. Song, L. Huang, et al., "Energy Performance and Fire Risk of Solar PV Panels Under Partial Shading: An Experimental Study," *Renewable Energy*, vol. 246, 122910, 2025.

[48] Shedrack Onwusinkwue, Femi Osasona, et al., "Artificial Intelligence (AI) in Renewable Energy: A Review of Predictive Maintenance and Energy Optimization," *World Journal of Advanced Research and Reviews*, vol. 21, no. 1, pp. 2487–2799, 2024.

[49] E. Proedrou, "A Comprehensive Review of Residential Electricity Load Profile Models," *IEEE Access*, vol. 9, pp. 12114–12133, 2021.

[50] C. Vassiliades, "Optimizing Energy Efficiency in Mediterranean Single-Family Homes: A Parametric Study of Building Typology, Orientation, and BIPV Integration," *Renewable Energy*, vol. 237, 121541, 2024.

[51] D. Zhou, Z. Wang, K. Xi, C. Zuo, and Y. Jia, "Optimization Configuration Analysis of Wind-Solar-Storage System Based on HOMER," *Energy Engineering*, vol. 122, no. 5, pp. 2119–2153, 2025.

[52] P. Olczak, and D. Matuszewska, "Analysis of Implementing Hydrogen Storage for Surplus Energy from PV Systems in Polish Households," *Energies*, vol. 18, no. 14, 3674, 2025.

[53] H. M. H. Farh, A. A. Al-Shamma'a, et al., "Optimization and Uncertainty Analysis of Hybrid Energy Systems Using Monte Carlo Simulation Integrated with Genetic Algorithm," *Computers and Electrical Engineering*, vol. 120, 109833, 2024.

[54] D. Roy, H. Taghavifar, et al., "Multi-Criteria Decision-Making and Uncertainty Analyses of Off-Grid Hybrid Renewable Energy Systems for an Island Community," *Energy Conversion and Management*, vol. 343, 120120, 2025.

[55] F. K. Alhousni, F. B. I. Alnaimi, et al., "Photovoltaic Power Prediction Using Analytical Models and Homer-Pro: Investigation of Results Reliability," *Sustainability*, vol. 15, no. 11, 8904, 2023.

[56] A. Demirci, Z. Öztürk, and S. M. Tercan, "Decision-Making Between Hybrid Renewable Energy Configurations and Grid Extension in Rural Areas for Different Climate Zones," *Energy*, vol. 262, 125402, 2023.

[57] D. Wang, and M. Grimmelt, "Climate Influence on the Optimal Stand-Alone Microgrid System with Hybrid Storage – A Comparative Study," *Renewable Energy*, vol. 208, pp. 657–664, 2023.

[58] C. Choe, and H. Lim, "Life Cycle-Based Strategy and Feasibility of Surplus-To-X-To-Electricity on Domestic Surplus Utilization in the Republic of Korea," *Korean Journal of Chemical Engineering*, vol. 42, no. 8, pp. 1669–1682, 2025.

[59] C. Palanichamy, and P. Naveen, "Micro Grid for All India Institute of Medical Sciences, Madurai," *Clean Energy*, vol. 5, no. 2, pp. 254–272, 2021.

[60] E. E. Nta, N. I. Okpura, and K. M. Udofia, "PV Based Microgrid for Remote Area Electrification in Nigeria: A Systematic Review of Concepts and Extant Strategies," *Physical Science International Journal*, vol. 28, no. 5, pp. 125–146, 2024.

[61] A. Rafieioskouei, K. Rogale, A. A. Saei, M. Mahmoudi, and B. Bonakdarpour, "Beyond Correlation: Establishing Causality in Protein Corona Formation for Nanomedicine," *Molecular Pharmaceutics*, vol. 22, no. 5, pp. 2723–2730, 2025.

[62] A. Guha, S. A. Sadeghi, et al., "AI-Driven Prediction of Cardio-Oncology Biomarkers Through Protein Corona Analysis," *Chemical Engineering Journal*, vol. 509, 161134, 2025.

[63] A. Rafieioskouei, and B. Bonakdarpour, "Efficient Discovery of Actual Causality Using Abstraction Refinement," *IEEE Transactions on Computer-Aided Design of Integrated Circuits and Systems*, vol. 43, no. 11, pp. 4274–4285, 2024.

[64] A. Rastgou, J. Moshtagh, and S. Bahramara, "Probabilistic Power Distribution Planning Using Multi-Objective Harmony Search Algorithm," *Journal of Operation and Automation in Power Engineering*, vol. 6, no. 1, pp. 111–125, 2018.

[65] A. Rastgou, S. Bahramara, and J. Moshtagh, "Flexible and Robust Distribution Network Expansion Planning in the Presence of Distributed Generators," *International Transactions on Electrical Energy Systems*, vol. 28, no. 12, e2637, 2018.

[66] A. Rastgou, and S. Hosseini-Hemati, "Simultaneous Planning of the Medium and Low Voltage Distribution Networks Under Uncertainty: A Bi-Level Optimization Approach," *International Transactions on Electrical Energy Systems*, vol. 2022, pp. 1–19, 2022.

[67] A. Rastgou, "Distribution Network Expansion Planning: An Updated Review of Current Methods and New Challenges," *Renewable and Sustainable Energy Reviews*, vol. 189, 114062, 2024.

Declaration of competing interest

The author declare that she has no known competing financial interests or personal relationships that could have appeared to influence the work reported in this paper. The ethical issues, including plagiarism, informed consent, misconduct, data fabrication and/or falsification, double publication and/or submission, redundancy, have been completely observed by the author.

Bibliography

Narges Loghmani was born in 1991 in Shahrekord, Iran. received her Master's degree in Architecture from Yazd University, iran, In 2016. She has been a faculty member of the Department of Architectural Engineering at the National University of Skills since 2022. Her areas of expertise in research include architecture, sustainable architecture, architecture and energy.

Email: nloghmani@tvu.ac.ir

ORCID: 0000-0003-4675-2921

Contribution Statement: Conceptualization, Data curation, Formal analysis, Funding acquisition, Investigation, Methodology, Project administration, Resources, Software, Supervision, Validation, Visualization, Roles/Writing - original draft, Writing-review & editing.

Journal of Green Energy Research and Innovation

Optimized Energy Management in Grid-Connected Renewable Energy Hubs Incorporating Thermal, Compressed Air, and Hydrogen Storage Systems with Heat Pumps

Ehsan Akbari, Sasan Pirouzi, Abdolreza Behvandi

Highlights

- **The study optimizes a unified energy hub framework integrating solar, wind, and bio-waste sources with compressed air, thermal, and hydrogen storage.**
- **Advanced management of interdependencies between heat pumps, CHP systems, and storage units reduced energy procurement costs by approximately 44.1%.**
- **Operational efficiency improvements ranged from 28% to 90%, significantly outperforming traditional load flow methodologies.**
- **The proposed multi-criteria strategy successfully balances economic performance and technical reliability for modern electricity and heat grid operators.**

Graphical Abstract

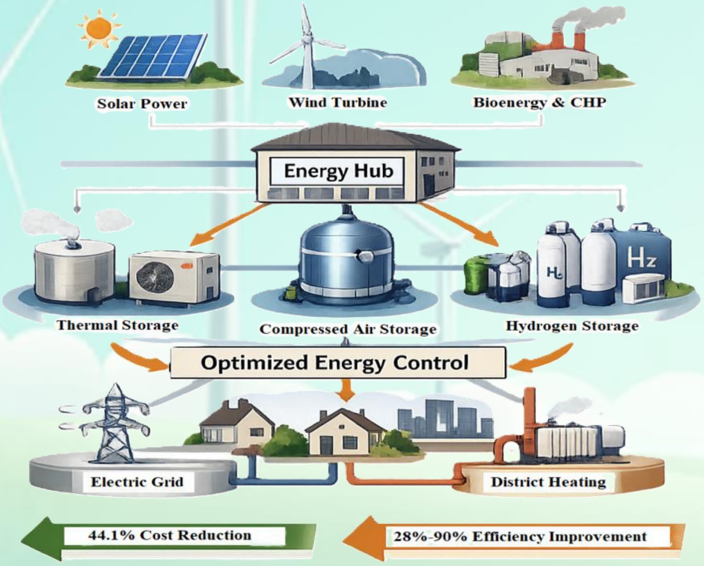

Use your device to scan and read the article online

Citation

E. Akbari, S. Pirouzi, and A. Behvandi, "Energy Management of Grid-Connected Renewable Energy Hubs with Thermal, Compressed Air and Hydrogen Storages and Heat Pump," Journal of Green Energy Research and Innovation, vol. 3, no. 1, pp. 31-41, 2026.

https://doi.org/10.61882/jgeri.3.1.31

JGERI Journal of Green Energy Research and Innovation

Journal of Green Energy Research and Innovation 3.1 (2026) 31-41

Online ISSN: 3041-9018

Journal of Green Energy Research and Innovation

Journal Homepage: www.jgeri.araku.ac.ir

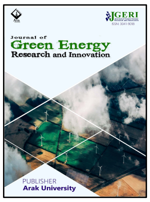

Optimized Energy Management in Grid-Connected Renewable Energy Hubs Incorporating Thermal, Compressed Air, and Hydrogen Storage Systems with Heat Pumps

Ehsan Akbari [1] , Sasan Pirouzi [2,*] , Abdolreza Behvandi [3]

[1] *Department of Electrical Engineering, Mazandaran University of Science and Technology, Babol, Iran.*

[2] *Department of Engineering, Sem.C., Islamic Azad University, Semmirom, Iran.*

[3] *Department of Electrical Engineering, Ramh.C., Islamic Azad University, Ramhormoz, Iran.*

ARTICLE INFO

Keywords:
Energy hub management,
Compressed air energy storage,
Hydrogen storage,
Thermal energy storage,
Multi-energy systems
optimization.

Article History:
Received: 19 August 2025;
Revised: 15 September 2025;
Accepted: 22 September 2025.

Article type:
Research Article

* ***Corresponding authors***
E-mail address
s.pirouzi@sutech.ac.ir (S. Pirouzi)

ABSTRACT

This study explores the effective energy management strategies employed by electricity and heat grids hubs, emphasizing multi-criteria objectives that balance economic performance and operational efficiency for network operators. The primary objective of this study is to optimize the integration of multiple renewable energy sources, namely solar energy, bio-waste units, and wind turbines, within a unified management framework. The system employs advanced energy storage technologies, including compressed air, thermal, and hydrogen storage units. Thermal energy production is achieved through electrically powered heat pumps, while combined heat and power (CHP) systems are utilized to enhance the performance of both bio-waste and hydrogen storage subsystems. The proposed approach seeks to optimize energy procurement costs across these networks, aligning with their operational models. A key challenge tackled involves efficiently managing the interdependencies of energy sources and storage systems within the conceptual framework of an energy hub. By addressing these complexities, the strategy demonstrates measurable improvements in both technical and financial outcomes for electricity and heat grids. The numerical analysis highlights the efficacy of the proposed approach, demonstrating significant improvements in both economic viability and operational efficiency. Specifically, the integration of renewable energy hubs, storage, and heat pump systems, has achieved an approximate 44.1% enhancement in economic conditions and operational improvements ranging from 28% to 90%. These gains signify a clear advantage over traditional load flow methodologies, reaffirming the potential of advanced hub energy management in modern networks.

1. Introduction

Energy Hubs (EHs) play a pivotal role in advancing energy network operations, and their functionality has been thoroughly explored across various research studies. In [1], EH unit commitment (UC) models, as outlined in earlier research, incorporate critical components such as hydrogen vehicle (HV) parking lots, electric heat pumps (HP), absorption chillers (AC), photovoltaic (PV) arrays, boilers, hydrogen electrolyzers (HELs), and a broad array of storage systems, including electric, thermal, cooling, and hydrogen facilities. These integrated systems transform inputs like natural gas, electricity, and heat into outputs satisfying demand for hydrogen, heating, cooling, natural gas, and electrical power. In [2], EHs collaborate with demand response aggregators to enable day-ahead scheduling, guided by existing methodologies. Renewable energy incorporation into EHs has been a notable focus area in past studies, with technologies such as PV panels, wind turbines (WTs), biomass systems, hydrogen ELs, combined heat and power (CHP) units, solar heaters, boilers, and associated storage systems receiving substantial attention. In [3], Beyond tapping into the gas and electricity grids, EHs leverage demand response aggregators for electricity procurement. To navigate uncertainties, such as fluctuating solar heat availability, electricity prices, variable PV and wind power outputs, and dynamic energy demands, a risk-aware framework called Information Gap Decision Theory (IGDT) has been employed.

In [4], optimizing EH operations to minimize costs and environmental impact has also been a core research objective. One study addresses optimal power flow for an EH equipped with components including electric vehicles (EVs), gas boilers, PV panels, CHP units, WTs, and heat storage systems. In [5], Future uncertainties in electricity pricing are managed using a grasshopper search algorithm alongside Monte Carlo simulation (MCS) to account for EV-related unpredictability. Further, the model integrates comprehensive thermal and electrical demand response strategies to enhance operational efficiency. Another approach leverages robust optimization to tackle uncertainties in power pricing and renewable energy availability. By analyzing EV charging behaviors through coordinated and uncoordinated charging loads with MCS methods, a clearer picture of charging dynamics emerges. Simultaneously, Smart Hub modeling frameworks have been developed to evaluate EH technical and economic feasibility. In [6], A simulation-based study investigates parameters like driver preferences, price inflation rates, PV module degradation, EV adoption trends, energy losses, and charging station variability. These factors are incorporated into simplified mathematical models capable of realistic day-ahead and real-time market assessments. For electricity market operations linked to EHs, researchers have proposed a two-stage stochastic modeling strategy aimed at handling demand uncertainties, renewable power fluctuations, and variable real-time pricing schemes. In [7], employing value-at-risk as a metric mitigates costs under adverse conditions while optimizing operational parameters for EH components and natural gas-electricity interactions. A multi-objective optimization methodology balances cost-effectiveness against risk resilience in complex EH designs. Innovative applications for EHs include their thermal integration within industrial settings like thermomechanical pulp mills. One study highlights how equipment such as electric boilers and steam generator HPs can be configured to meet the heating demands of paper machines while simultaneously supporting pulp mill operations. In [8], Advanced load forecasting techniques combined with reliability analyses and thermo-economic evaluations inform an efficient yet sophisticated EH design approach tailored to industrial processing needs. Finally, a multi-tier optimization strategy introduces stochastic-probabilistic models to enhance primary-level planning and secondary-level operations for EHs. This dual approach addresses challenging uncertainties linked to dynamic demand patterns and renewable energy generation variability while prioritizing resource efficiency and operational resilience. In [9], energy management strategies for heat and electricity generation grids in the context of renewable energy sources (RESs) focus on enhancing network flexibility through dynamic pricing services. These strategies revolve around EHs, which are composed of RESs, bio-waste units (BUs), responsive loads, and storage systems. Notably, bio-waste systems contribute to both electrical energy and heat generation simultaneously. The proposed methodology addresses gaps between network energy costs and hub-flexibility revenue by optimizing resource allocation. It incorporates flexibility models for hubs, advanced power-flow equations, and operational frameworks for managing resources, storage systems, and responsive loads. Reference [10] discusses how flexible EHs equipped with technologies such as compressed air systems, thermal and hydrogen storage (HS) devices, BUs, and wind farms (WFs) can be effectively integrated into energy markets through market-clearing price models. These hubs, operating within both electricity and heat grids, employ integrated heat and power technologies to produce heat and electricity concurrently through BUs. Ref. [11] proposed an innovative energy management framework that integrates Unified Plug-In Electric Vehicle (PEV)-based demand response strategies with energy storage systems through a hybrid coordination approach. Reference [12] presents a two-layer optimization model that enables coordinated energy exchange between two interconnected energy hubs (EHs). Operating collectively as a virtual energy hub (VEH), the system addresses heat, water, and electricity demands while engaging in the thermal energy market and adjusting to the upstream distribution network's hosting capacity to efficiently accommodate supplementary loads. Reference [13] proposes an innovative solution to address multifaceted challenges associated with EHs, particularly focusing on energy generation and transmission complexities across gas and electricity grids. A multi-carrier EH capable of generating and distributing electricity, heating, and cooling from diverse sources, including wind, solar, fuel cells (FCs), batteries, and compressed air, is featured in [14]. This hub incorporates intelligent functionalities to support participation in both electrical and thermal demand response programs, easing peak demand periods and enhancing overall system efficiency. Lastly, [15] examines stochastic energy management strategies within microgrid environments, considering renewable sources such as solar, wind, and tidal power alongside demand response initiatives and comprehensive energy storage systems.

Hubs generally rely on renewable sources such as wind and solar energy, but another valuable renewable option is the bio-waste system. This system generates gas by processing waste and, when paired with a CHP unit, can simultaneously produce heat and electricity. However, the utilization of bio-waste systems integrated with CHP has been examined in only a handful of studies. The majority of research efforts have focused on battery technology due to its high efficiency, although batteries are limited by a short lifespan and elevated installation costs. Consequently, storage devices like hydrogen and compressed air emerge as suitable alternatives, offering commendable efficiency and extended service life. Despite this potential, their integration has also seen limited exploration in scholarly works. This study develops an energy management strategy specifically designed for hubs that are integrated with both thermal and electrical networks. It aims to balance operational efficiency with financial optimization from the perspective of network operators. These hubs are equipped with RESs, including wind, solar, and BUs, complemented by storage systems for hydrogen, compressed air, and thermal energy. In addition, BU and FC are enhanced with CHP systems to boost energy efficiency, while HP convert electricity into thermal energy for broader use. The electrical output of these hubs primarily comes from WT, PV, and supplementary backup units.

$$\begin{aligned} P_{Sb,t} + \sum_i C_{Ei,b} P_{EHi,t} + \sum_j A_{Ej,b} P_{Lb,j,t} \\ = P_{Db,t}\ \forall b,t \end{aligned} \tag{1}$$

$$Q_{Sb,t} + \sum_j A_{Ej,t} Q_{Lb,j,t} = Q_{Db,t}\ \forall b,t \tag{2}$$

$$\begin{aligned} H_{Sn,t} + \sum_i C_{Hi,n} H_{EHi,t} + \sum_j A_{Hj,n} H_{Ln,j,t} \\ = H_{Dn,t} \forall n,t \end{aligned} \tag{3}$$

$$P_{Lb,j,t} = G_{Lb,j}\left(V_{b,t}\right)^2 - V_{b,t}V_{j,t}\begin{Bmatrix} G_{Lb,j}\cos\left(\varphi_{b,t} - \varphi_{j,t}\right) + \\ B_{Lb,j}\sin\left(\varphi_{b,t} - \varphi_{j,t}\right) \end{Bmatrix} \forall b,j,t \tag{4}$$

$$Q_{Lb,j,t} = -B_{Lb,j}\left(V_{b,t}\right)^2 + V_{b,t}V_{j,t}\begin{Bmatrix} B_{Lb,j}\cos\left(\varphi_{b,t} - \varphi_{j,t}\right) \\ -G_{Lb,j}\sin\left(\varphi_{b,t} - \varphi_{j,t}\right) \end{Bmatrix} \forall b,j,t \tag{5}$$

$$H_{Ln,j,t} = C_{Ln,j}\left(T_{n,t} - T_{j,t}\right) \forall n,j,t \tag{6}$$

$$V_{\min} \le V_{b,t} \le V_{\max} \, \forall b,t \tag{7}$$

$$T_{\min} \le T_{n,t} \le T_{\max} \, \forall n,t \tag{8}$$

$$\left(P_{Lb,j,t}\right)^2 + \left(Q_{Lb,j,t}\right)^2 \le \bar{S}_{Lb,j} \, \forall b,j,t \tag{9}$$

$$\left|H_{Ln,j,t}\right| \le \bar{H}_{Ln,j} \, \forall n,j,t \tag{10}$$

$$\left(P_{Sb,t}\right)^2 + \left(Q_{Sb,t}\right)^2 \le \bar{S}_{Sb} \, \forall b,t \tag{11}$$

$$\left|H_{Sn,t}\right| \le \bar{H}_{Sn} \, \forall n,t \tag{12}$$

$$P_{EHi,t} = P_{Wi,t} + P_{Vi,t} + P_{Bi,t} + \left(P_{Fi,t} - P_{Ei,t}\right) + \left(P_{Gi,t} - P_{Mi,t}\right) - P_{HPi,t} - P_{Di,t} \forall i,t \tag{13}$$

$$H_{EHi,t} = H_{Bi,t} + H_{HPi,t} + H_{Fi,t} + \left(H_{DISi,t} - H_{CHi,t}\right) - H_{Di,t} \forall i,t \tag{14}$$

$$H_{Bi,t} = \frac{(1-\eta_B)\eta_H}{\eta_B} P_{Bi,t} \, \forall i,t \tag{15}$$

$$H_{HP_{i,t}} = \eta_{HP} P_{HPi,t} \, \forall i,t \tag{16}$$

$$0 \le H_{HP_{i,t}} \le n_{HP} \bar{H}_{HPi} \, \forall i,t \tag{17}$$

$$0 \le P_{Fi,t} \le n_{HS} \bar{P}_{Fi} \, \forall i,t \tag{18}$$

$$0 \le P_{Ei,t} \le n_{HS} \bar{P}_{Ei} \, \forall i,t \tag{19}$$

$$P_{Fi,t} P_{Ei,t} = 0 \, \forall i,t \tag{20}$$

$$n_{HS} E_{HTi} \le n_{HS} \hat{E}_{HTi} + \textstyle\sum_{h=1}^{t} \left(\eta_E P_{Ei,t} - \dfrac{1}{\eta_F} P_{Fi,t}\right) \le n_{HS} \bar{E}_{HTi} \forall i,t \tag{21}$$

$$H_{Fi,t} = \frac{(1-\eta_F)\eta_H}{\eta_F} P_{Fi,t} \, \forall i,t \tag{22}$$

$$0 \le P_{Gi,t} \le n_{CA} \bar{P}_{Gi} \, \forall i,t \tag{23}$$

$$0 \le P_{Mi,t} \le n_{CA} \bar{P}_{Mi} \, \forall i,t \tag{24}$$

$$P_{Gi,t} P_{Mi,t} = 0 \, \forall i,t \tag{25}$$

$$n_{CA} E_{CATi} \le n_{CA} \hat{E}_{CATi} + \textstyle\sum_{h=1}^{t} \left(\eta_M P_{Mi,t} - \dfrac{1}{\eta_G} P_{Gi,t}\right) \le n_{CA} \bar{E}_{CATi} \, \forall i,t \tag{26}$$

$$0 \le H_{DISi,t} \le n_T \bar{H}_{DISi} \, \forall i,t \tag{27}$$

$$0 \le H_{CHi,t} \le n_T \bar{H}_{CHi} \, \forall i,t \tag{28}$$

$$H_{DISi,t} H_{CHi,t} = 0 \, \forall i,t \tag{29}$$

$$n_T \underline{E}_{TESi} \le n_T \hat{E}_{TESi} + \textstyle\sum_{h=1}^{t} \left(\eta_{CH} H_{CHi,t} - \dfrac{1}{\eta_{DIS}} H_{DISi,t}\right) \le n_T \bar{E}_{TESi} \, \forall i,t \tag{30}$$

Meanwhile, thermal energy is generated via FCs, HPs, and backup units as well. To ensure reliable energy storage, hydrogen and compressed air systems are dedicated to the electrical section, while thermal storage systems support the thermal side. The proposed energy management scheme represents the primary innovation introduced by this paper. It is structured as a deterministic optimization model aimed at minimizing total expected operating costs across electricity and heat generation networks. The formulation incorporates a series of constraints, including equations for optimal power distribution alongside operational models for RESs, storage units, and HPs, all interconnected to function seamlessly within the EH framework. Due to its non-linear nature, the optimization model is addressed by adopting the Interior Point OPTimizer (IPOPT) algorithm implemented in the General Algebraic Modeling System (GAMS). The core contributions of this scheme are twofold: first, it focuses on the optimal operation of a bio-waste energy unit within the hub to enhance overall energy efficiency. Second, it introduces robust energy management strategies for hydrogen and compressed air storage systems to improve the network's both economic and operational metrics.

Section 2 provides a comprehensive analysis of energy management strategies formulated for network-connected energy hubs. Section 3 focuses on a detailed case study, followed by Section 4, which presents and interprets the numerical results obtained from multiple simulation scenarios. Finally, Section 5 concludes the paper by summarizing the principal findings and outlining key insights.

2. Formulation of the Proposed Plan

This segment explores the energy management approaches utilized by renewable EHs, which incorporate diverse resources such as compressed air, hydrogen, and thermal storage. These hubs are designed with interconnected electric and thermal grids to maximize operational efficiency and minimize costs. The presented framework outlines the functional behavior of renewable and adaptable energy sources within the EH system, while also formulating critical equations to achieve optimal power allocation across network infrastructures. Consequently, the methodology is systematically expressed through mathematical definitions as described in Equations (1)-(31).

$$\min\mathrm{Cos}t = \sum_{b,t}\lambda_{Et}P_{Sb,t} + \sum_{n,t}\lambda_{Ht}H_{Sn,t} \tag{31}$$

Subject to:

To minimize the anticipated operating costs (Cost) within the electrical and thermal grids, this approach focuses on the objective function, given in Equation (1). Here, the energy procurement cost from the upstream network is expressed as the sum of two components, corresponding respectively to the electricity grid (first term) and the heat grid (second term) [9]. The cost is calculated by multiplying the energy price by the quantity of energy transmitted through the distribution points. Equations (2) to (13) outline the equations needed for optimal power flow across these networks. Equations (2) to (7) specifically detail the interactions involved in distributing power within these systems. Specifically, Equations (2) and (4) define the distribution of active and reactive power across electrical buses and the allocation of heat power within thermal nodes, respectively [9–10]. Furthermore, Equations (5)–(7) describe the flow of active and reactive power through the electrical distribution lines and the transfer of thermal energy through the pipeline network [16].

Equations (8) to (13) specify the boundaries within the heat and electricity grids. Equations (8) and (9) address the limits on voltage magnitude at electrical buses and temperature at thermal nodes, respectively. The limits on apparent power flowing through electrical distribution lines and heat power through pipelines are outlined in limitations (10) and (11). Additionally, Equations (12) and (13) take into account these limitations for electricity and heat distribution posts. Equations (14) to (31) define the operational parameters for Environmental Hubs that utilize flexible and RESs. Specifically, Equations (14) and (15) describe the balance between thermal and active power within these hubs. The model for RESs includes WF, PV Farms (PVF), and Battery Unit Farms (BUF). The findings indicate that the battery unit (BU) is integrated with combined heat and power (CHP) technology, allowing simultaneous generation of electrical and thermal energy. The heat power output of the BU is defined in Equation (16) as a coefficient corresponding to its active power [9]. The operational behavior of heat pumps (HPs) is described in Equations (17) and (18). The HP unit converts electrical energy into thermal energy [17], effectively acting as an active power consumer while producing thermal output. Equation (17) outlines the correlation between heat power and active HPs [17]. Equation (18) addresses the capacity limitations for power generation at the HPs' output. Equations (19) to (23) define the operational model for the HS [18,19], which includes the FC, electrolyzer (EL), and hydrogen tank (HT). Equation (19)-(20) specify the capacity limits for the FC and EL, respectively. To prevent simultaneous operation of HS in charge and discharge modes, Equation (21) ensures that the EL and FC do not operate at the same time. Equation (22) sets the maximum allowable hydrogen energy storage in the HT. The CHP model for FCs is described by Equation (23), stating that an FC's output heat power is proportional to its active power [18]. Equations (24) to (27) define the CAES operational model [20], which consists of a compressed air tank (CAT), a generator, and a motor. Equations (24) and (25) address the capacity restrictions of the generator and motor. Equation (26) prohibits their simultaneous operation, and restriction (27) sets the maximum energy capacity for compressed air storage in the CAT [20]. The TES operational model is defined in Equations (28) to (31). These include charge and discharge rate limitations in Equations (28) and (29). Relation (30) prevents simultaneous charging and discharging of TES, while Equation (31) sets limitations on the energy stored within TES [16].

3. Case Study

Figure 1 illustrates the integration of the EMS described in this section across the IEEE 33-bus electrical network [21] and the 14-node Madumvej heat network [22]. To obtain the time-varying load profile, the load factor curve is multiplied by the corresponding maximum load at each time interval. The projected daily load factor curve for the electrical network, established in previous studies [9-10], serves as the basis for calculations. During off-peak hours, from 01:00 to 07:00, the cost of electricity is set at 17.6 $/MWh. This price elevates to 33 $/MWh during peak hours from 17:00 to 22:00, and stabilizes at 26.4 $/MWh throughout mid-load periods at remaining intervals [9]. On the thermal energy side, pricing remains constant at 22 $/MWh during both peak hours (05:00–15:00) and off-peak periods (01:00–04:00 and 16:00–24:00) [9]. As depicted in Figure 1, the system is distributed across six operational hubs. Locations and attributes of each hub, including sources, storage units, and installed HP configurations, align with details provided in Table 1. Specifically, hubs 1 and 2 deliver thermal energy via BUF technology, whereas hubs 4 and 5 utilize localized HPs for thermal energy distribution. Electrical storage within hubs 1, 4, and 5 relies on CAES systems, while the remaining hubs are equipped with HS-type storage solutions. Comprehensive technical specifications for sources, storage units, and HPs are elaborated in supplementary references [23-24]. Each hub's load assignment corresponds directly to its strategic role within the network framework. Additional data regarding wind speed profiles, BU gas consumption trends, and solar radiation patterns are detailed in the referenced studies. It is noteworthy that the proposed scheme has no limitations for implementation on various types of energy networks, resources, and storage devices.

4. Numerical Reports and Discussions

This section presents the simulation studies carried out using the GAMS optimization environment, in which the IPOPT algorithm was employed as the primary solution strategy [25]. Owing to the inherently nonlinear and continuous characteristics of the proposed mathematical formulation, advanced nonlinear solvers such as IPOPT, BARON, BONMIN, and similar algorithms are particularly appropriate for achieving reliable and accurate solutions. To ensure robustness and computational efficiency, an extensive iterative trial-and-error procedure was conducted, during which multiple solvers and configurations were systematically evaluated and compared. The outcomes of this comparative analysis demonstrated that IPOPT consistently provided superior performance in terms of convergence stability, solution accuracy, and computational time, making it the most suitable solver for the problem under investigation. Consequently, IPOPT was selected for all subsequent simulations. The comprehensive quantitative findings obtained from these simulation studies are presented and discussed in detail in the following section.

A) Performance Assessment of Renewable Energy Hubs Incorporating Storage Units and Heat Pumps: The anticipated daily output patterns of active and heat power generated by sources, storage units, HPs, and EHs are illustrated in Figures 2 and 3. Figure 2 focuses on the daily production profiles of WT, PV, and biomass energy sources (BESs), providing a numerical correspondence to the variations in wind speed, solar radiation, and biogas rates presented in prior research [21]. The active power output of RESs is affected by these environmental conditions.

Per Figure 2's analysis, WFs, biogas utilization facilities (BUFs), and photovoltaic farms (PVFs) demonstrate peak performance at 1.8 MW, 2.4 MW, and 1.08 MW of active power generation, respectively. Regarding storage systems like heat storage units (HSs), Figure 2 reveals that during off-peak hours (1:00 to 7:00), they remain inactive due to lower electricity prices. In mid-load periods (8:00 to 16:00), HSs enter a charge mode where active power from RESs is transferred to them via ELs within the hubs. This operational strategy arises from substantial active power production by RESs during these hours, which could potentially overburden the electrical network with excess voltage.

Redirecting energy into HSs mitigates such risks. Furthermore, HSs consume power solely from RESs during this timeframe, thereby eliminating the need for supplementary energy costs from upstream networks. Later, between 17:00 and 22:00, HSs remain in charge mode, while FCs supply power to the electrical grid during peak hours from 23:00 to 24:00. HS operation at these times reduces energy expenses, as electricity prices are comparatively higher. Compressed air energy storage systems (CAESs) generally perform similarly to HSs but contribute additional active power to the grid during peak hours. Unlike ELs and FCs, CAES systems exhibit nearly equivalent motor and generator efficiency levels, whereas FC efficiency is notably lower than generator efficiency. Consequently, HS systems experience greater energy losses compared to CAESs, resulting in diminished discharge-mode power output relative to CAESs.

Both HSs and CAESs cease operation during off-peak hours due to the insufficient active power output from RESs during these periods, as illustrated in Figure 2. Operating energy storage systems under such conditions would necessitate additional power procurement from the main electrical grid, which would lead to increased operational expenditures while failing to achieve optimal cost efficiency. As a result, the strategic shutdown of HSs and CAESs during off-peak hours is economically justified and aligned with overall system optimization objectives.

In contrast, the performance of EHs enables sustained and reliable active power generation throughout the entire operational horizon. Consequently, EHs continuously inject electricity into the grid, providing a stable and uninterrupted energy supply despite fluctuations in RES production. The operational performance of HPs is intrinsically linked to EH functionality. Supplied primarily by energy generated within EHs, HPs remain operational during the periods of 1:00–7:00 and 17:00–24:00. Notably, during low-demand hours between 1:00 and 7:00, WF operations within Hub 4 produce approximately 1 MW of active power, which is sufficient to support the stable operation of HPs in this hub using energy derived exclusively from renewable energy sources.

In contrast, Hub 5 depends on solar energy production during low-load periods based on Figure 2's data; because solar output is minimal during these hours, Hub 5's HPs rely on electricity sourced from the main grid. However, during higher production intervals spanning 17:00–24:00, power contributions from HSs, CAESs, and WFs in both hubs significantly increase, allowing HPs in these hubs to operate efficiently using energy provided directly by EHs. Across all operation hours presented in these findings, the total active power output from EH systems remains consistently positive. This signifies that EHs not only support internal energy demands but also effectively function as producers supplying active electrical energy to the external grid throughout their operation.

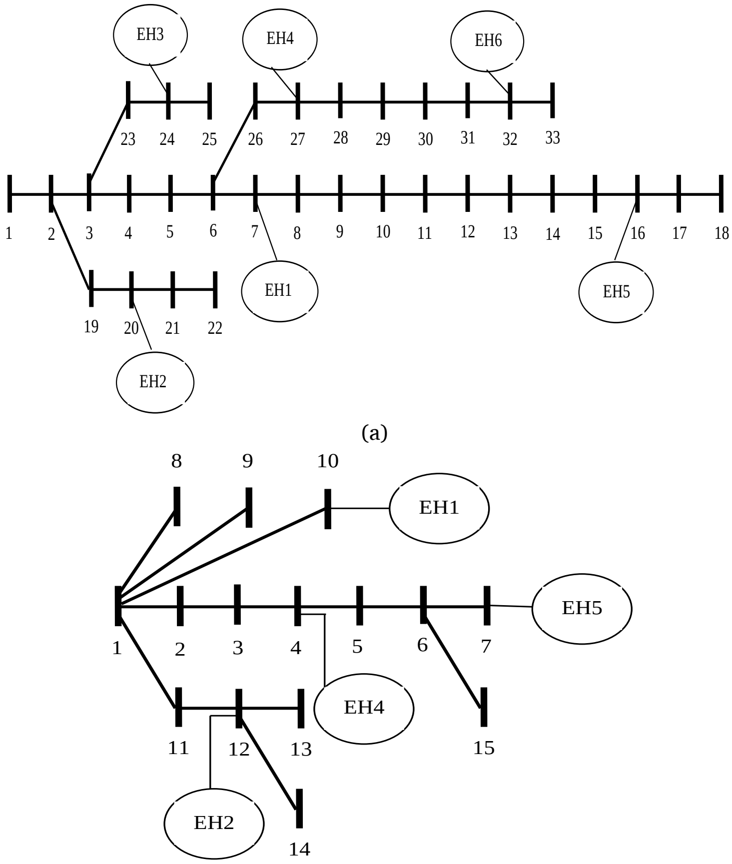

Figure 1. Test network, a) IEEE 33-bus electrical system [19], b) 14-node Madumvej district heating grid [20].

Tabe 1. Number of energy sources and storage units for energy hubs at different locations.

EH	Sources	Storages
1	120 BUs	40 CAESs, 40 TESs
2	120 BUs	80 HSs, 40 TESs
3	80 WTs	50 HSs
4	100 WTs, 50 HPs	30 CAESs, 25 TESs
5	1500 PVs, 40 HPs	25 CAESs, 25 TESs
6	1500 PVs	50 Ss

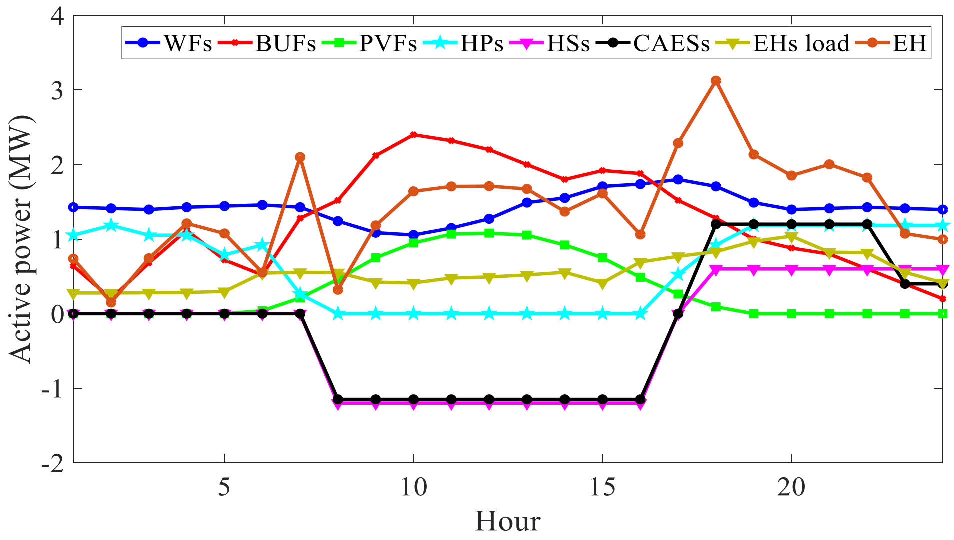

Figure 2. Expected daily active power trajectories of energy sources, storage systems, and aggregated EHs.

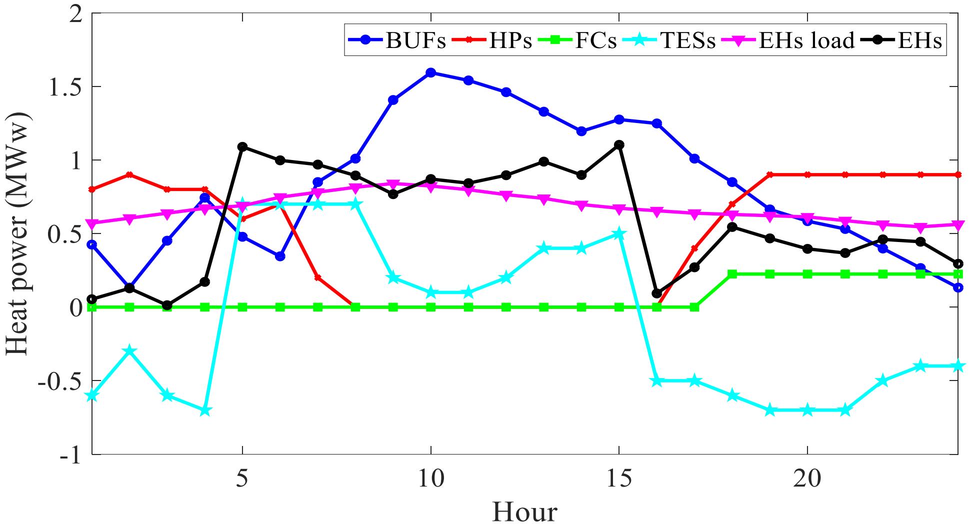

Figure 3. Expected daily heat power profiles of energy sources, storage systems, and EHs.

The heat power trends for BUFs, HPs, TESs, and EHs are illustrated in Figure 3. The daily heat power curve of BUFs closely resembles their active power curve, with only minor numerical differences. This similarity arises from Equation (16), which indicates that the heat power of a BU is directly correlated with its active power. During discharge mode, TESs experience peak thermal activity between 5:00 and 15:00, coinciding with high thermal energy prices. Discharging during these hours helps minimize costs. Outside of this period, TESs are in charge mode. Notably, during off-peak hours from 1:00 to 6:00 and 20:00 to midnight, BUFs produce less power than the demand from EHs. To avoid supplying heat power from the network to TESs during these times, HPs activate and generate heat power for EHs. Consequently, as shown in Figure 3, EHs continuously serve as energy producers, consistently injecting heat into the grid, thereby assisting in cost reduction within the heat grid.

B) *Operational Analysis of Electricity and Heat Grids Performance*: This section evaluates the key performance indicators for two distinct operational scenarios, namely Case I (Load flow analysis) and Case II (Proposed scheme). Table 2 provides a comprehensive comparison of the two cases by summarizing critical metrics, including Maximum Voltage Deviation (MVD), Maximum Temperature Deviation (MTD), Expected Energy Loss (EEL) for both the electrical network (E-EEL) and the thermal network (T-EEL), Peak Load Carrying Capacity (PLCC), and the overall operational cost (Cost) of the integrated energy networks.

In this study, energy loss within the network is defined as the difference between the total energy generated and the total energy consumed over the entire operating horizon. Voltage deviation is quantified as one minus the permissible voltage range, while temperature deviation is similarly calculated as one minus the allowable temperature range. Accordingly, MVD and MTD correspond to the maximum observed deviations in voltage and temperature, respectively, across all network nodes and time intervals. PLCC serves as an indicator of network robustness by representing the maximum peak load that the system can reliably accommodate without violating operational constraints.

As reported in Table 2, Case I reveals considerable energy losses, elevated operational costs, pronounced voltage drops, and notable temperature reductions during the energy network load distribution analysis. In addition, this case exhibits the lowest PLCC values, reflecting limited load-support capability, together with evident overvoltage occurrences and temperature fluctuations within the system.

In contrast, Case II, which strictly follows the proposed mathematical framework described by Equations (1)-(31) and incorporates energy hubs integrated with storage systems, heat pumps (HP), and renewable energy sources (RES), demonstrates a markedly improved operational performance. Relative to Case I, substantial enhancements are observed across all evaluated indicators. Specifically, the operational cost is reduced by approximately 44.1%, E-EEL decreases by 41%, T-EEL by 42.9%, and the overall EEL by 41.9%. Moreover, MVD and MTD are significantly mitigated, declining by 48.9% and 47.7%, respectively. Notably, PLCC experiences a pronounced improvement, increasing by nearly 82.5% in the electrical network and 89.5% in the thermal grid when compared to Case I, thereby confirming the superior reliability, efficiency, and load-handling capability of the proposed scheme.

Table 2. Values of operational indices under different operating scenarios.

Variable	Case I	Case II
Cost	4521.7	2527.6
E-EEL (MWh)	3.12	1.84
T-EEL (MWh)	2.54	1.45
EEL (MWh)	5.66	3.29
MVD (p.u.)	0.092	0.047
MTD (p.u.)	0.086	0.045
E-PLCC (MW)	3.72	6.79
T-PLCC (MW)	3.05	5.78

Table 3 presents the sensitivity analysis of the objective function, namely the operational Cost, with respect to variations in energy price, peak load, and renewable power penetration. In this table, the parameter α denotes the rate of increase applied to each examined factor. The results indicate that a 10% rise in energy price and peak load leads to corresponding increases in Cost of approximately 9.48% and 10.82%, respectively. In contrast, a 10% increase in renewable power generation results in a reduction of Cost by about 5.28%, highlighting the economic benefits associated with higher renewable energy integration.

An increase in peak load is typically associated with greater overall energy consumption, as higher maximum demand often reflects more intensive or extended operation of electrical and thermal equipment. Consequently, the energy required by the network from the upstream supply increases, which directly contributes to higher operational costs. Conversely, enhanced renewable energy generation reduces dependency on upstream network energy procurement, thereby lowering purchasing costs and improving overall economic performance. On the other hand, rising energy prices increase the monetary value of energy transactions within the system. While higher prices raise procurement expenses, they also amplify revenues from energy sales, ultimately causing an upward shift in the overall cost function, as reflected in the sensitivity analysis results.

Figure 4 illustrates the obtained Cost values corresponding to different solution algorithms. In this figure, IPOPT, BONMIN, and BARON are optimization solvers based on deterministic mathematical programming techniques, all of which are available within the GAMS software environment. In contrast, Particle Swarm Optimization (PSO) and the Genetic Algorithm (GA) are population-based evolutionary algorithms, and the proposed model was implemented for these solvers using the MATLAB software platform, which provides dedicated toolboxes for such metaheuristic methods.

As depicted in Figure 4, the application of different solvers to the proposed design results in distinct solutions and associated Cost values. This variation can be attributed to the inherently non-convex nature of the optimal power distribution problem in the electrical network, which may lead to multiple local optima depending on the employed solution strategy. Under such circumstances, the solver that yields the most favorable operating condition, characterized by the minimum achievable Cost, is considered the most appropriate. Based on the comparative results shown in Figure 4, the IPOPT solver demonstrates superior performance by converging to the lowest Cost value among the examined algorithms, thereby confirming its suitability and effectiveness for solving the proposed optimization problem.

Table 3. Sensitivity analysis for the objective function (Cost) based on the different parameters in Case II.

Parameter	Cost ($) for			Deviation (%)
	α = 0	α = 10%	α = 20%	
Energy price ($/MWh)	2527.6	2767.3	3007	+9.48×α
Peak load (MW)	2527.6	2801.2	3074.8	+10.82×α
Renewable power (MW)	2527.6	2394.1	2260.6	-5.28×α

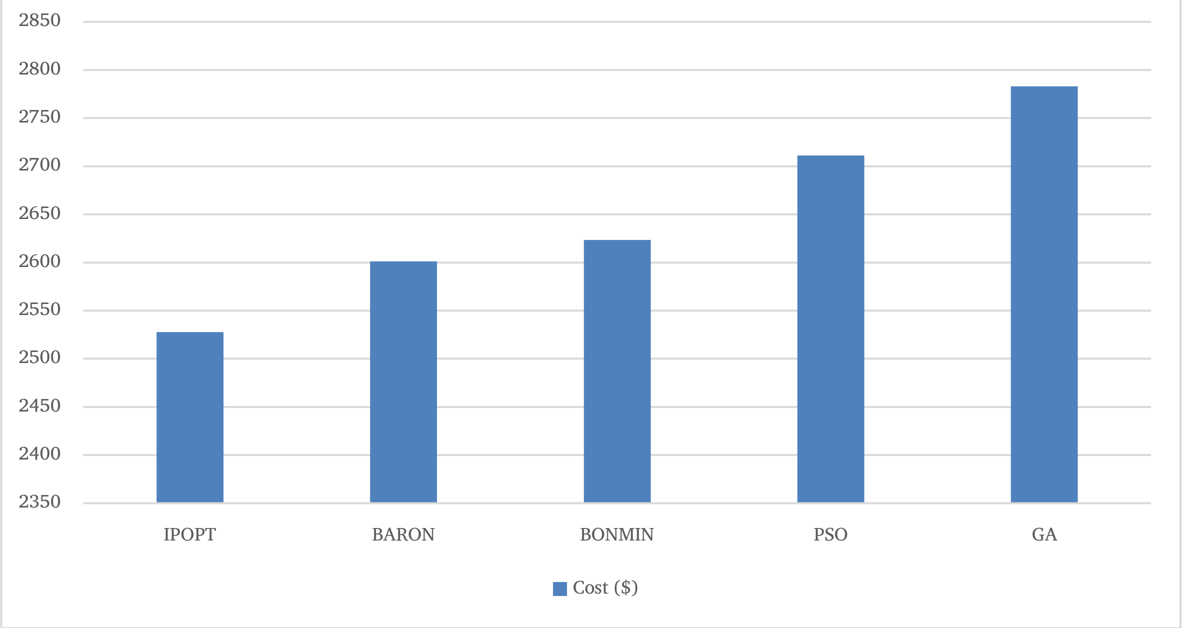

Figure 4. Value of Cost obtained by different solvers.

5. Conclusions

This study investigates the cost-effective operation of integrated thermal and electrical networks incorporating renewable EHs. These hubs encompass various components, including HS, thermal storage, compressed air storage, WTs, solar units, BUs, and HPs. The proposed solution aims to reduce operating costs by optimizing the energy management of these hubs within their operational constraints and aligning with an optimal power distribution model for the networks in question. The numerical results indicate that the approach successfully enhances the economic performance of these networks. Specifically, the study shows an approximate 44% improvement in economic efficiency compared to traditional load distribution scenarios. This method also positively impacts various operational parameters, such as power management for HPs and storage systems (compressed air, hydrogen, and thermal). Improvements are observed across key metrics like energy losses, voltage stability, temperature profiles, and load capacity, with enhancements ranging from 28% to 90% compared to previous load distribution models.

This study evaluated the performance capabilities of resources and storage systems configured as an EH within the proposed framework. However, load response is a method for managing energy and it can be useful in improving energy efficiency. This study identifies the incorporation of uncertainties in renewable resources, load demand, and energy prices as a direction for future research within the proposed framework. Therefore, stochastic, probabilistic, or robust modeling needs to be considered for them. In this paper, deterministic models were used for them, but this aspect is identified as a direction for future research within the proposed framework. To solve the proposed problem in this paper, mathematical algorithms were used. However, if the problem size increases, it is possible that mathematical solvers may encounter difficulties in converging to a feasible solution for the formulated problem, or a more powerful computing system will be required. In this case, the computational cost will increase. To compensate for this, it is necessary to use decomposition algorithms, hybrid evolutionary algorithms, and linear approximation models. These are considered future studies.

NOMENCLATURE

Variables			
Cost	Expected cost of operation ($)	PL, QL, HL	Active (MW) and reactive (MVAr) power passing through the electric distribution line, and heat power (MW) passing through the heat pipe
HB, HHP, HF	Heat power of bio-waste unit (BU), heat pump (HP), and fuel cell (FC) in MW	PM, PG	Active power of motor and generator in compressed air energy storage (CAES) in MW
HCH, HDIS	Heat power of thermal energy storage (TES) in charge and discharge mode (MW)	PS, QS, HS	Active (MW) and reactive (MVAr) power passing through the electric distribution post, and heat power (MW) passing through the heat post
PB, PV, PW	Active power of BU, photovoltaic (PV), and wind turbine (WT) in MW	T	Temperature (p.u.)
PE, PF	Active power of electrolyzer (EL) and FC in hydrogen storage (HS) in MW	V, φ	Voltage range (p.u.) and voltage angle (radian)
PEH, HEH	Active and heat power of the energy hub (EH) in MW	Parameters	
PHP	Active power of HP in MW	AE	Intersection matrix of bus and distribution line
		AH	Intersection matrix of node and heat pipe
BL, GL	Susceptance and conductance of distribution line (p.u.)	T_{miss} T_{max}	Minimum and maximum permissible temperature (p.u.)
CE	Intersection matrix of EH and the electric bus	$\bar{S}_L, \bar{S}_S$	Maximum apparent power passing through the electric distribution line and substation (MVA)
CH	Intersection matrix of EH and the heat node	V_{wisy} V_{max}	Minimum and maximum permissible voltage range (p.u.)
CL	Thermal constant of the heat pipe (p.u.)	η_{CH}, η_{DIS}	Charge and discharge efficiency in TES
$\underline{E}_{CAT}, \bar{E}_{CAT}, \hat{E}_{CAT}$	Minimum and maximum energy stored in the compressed air tank (CAT) and its initial energy (MWh)	η_H	Thermal efficiency in combined heat and power (CHP)
$\underline{E}_{HT}, \bar{E}_{HT}, \hat{E}_{HT}$	Minimum and maximum energy stored in the hydrogen tank (HT) and its initial energy (MWh)	η_{HP}	HP efficiency
$\underline{E}_{TES}, \bar{E}_{TES}, \hat{E}_{TES}$	Minimum and maximum energy stored in TES and its initial energy (MWh)	η_M	Motor and generator efficiency in CAES
$\bar{H}_{CH}, \bar{H}_{DIS}$	Charge/discharge rate in TES (MW)	η_G	Electric and thermal energy price ($/MWh)
$\bar{H}_L, \bar{H}_S$	Maximum heat power passing through the heat pipe and heat post (MW)	λ_E, λ_H	Thermal efficiency in combined heat and power (CHP)
$\bar{H}_{HP}$	Maximum heat power produced by HP (MW)	Indices	
P_D, Q_D, H_D	Active (MW), reactive (MVAr), and thermal (MW) load	b, n	Bus in the electric network, a node in the heat network
$\bar{P}_E, \bar{P}_F$	EL and FC capacity in HS (MW)	i	EH
$\bar{P}_M, \bar{P}_G$	Motor and generator capacity in CAES (MW)	j	Auxiliary index corresponding to bus or node
		t	Operating hour

References

[1] M. Nasir, A. Rezaee Jordehi, et al., "Optimal Operation of Energy Hubs Including Parking Lots for Hydrogen Vehicles and Responsive Demands," *Journal of Energy Storage*, vol. 50, 104630, 2022.

[2] M. Nasir, A. R. Jordehi, et al., "Operation of Energy Hubs with Storage Systems, Solar, Wind and Biomass Units Connected to Demand Response Aggregators," *Sustainable Cities and Society*, vol. 83, 103974, 2022.

[3] R. Li, and S. SaeidNahaei, "Optimal Operation of Energy Hubs Integrated with Electric Vehicles, Load Management, Combined Heat and Power Unit and Renewable Energy Sources," *Journal of Energy Storage*, vol. 48, 103822, 2022.

[4] M. Aslani, M. Mashayekhi, H. Hashemi-Dezaki, and A. Ketabi, "Robust Optimal Operation of Energy Hub Incorporating Integrated Thermal and Electrical Demand Response Programs Under Various Electric Vehicle Charging Modes," *Applied Energy*, vol. 321, 119344, 2022.

[5] H. George-Williams, N. Wade, and R. Carpenter, "A Probabilistic Framework for the Techno-Economic Assessment of Smart Energy Hubs for Electric Vehicle Charging," *Renewable and Sustainable Energy Reviews*, vol. 162, 112386, 2022.

[6] A. R. Jordehi, "Two-Stage Stochastic Programming for Risk-Aware Scheduling of Energy Hubs Participating in Day-Ahead and Real-Time Electricity Markets," *Sustainable Cities and Society*, vol. 81, 103823, 2022.

[7] B. Talebjedi, T. Laukkanen, H. Holmberg, and S. Syri, "Advanced Design and Operation of Energy Hub for Forest Industry Using Reliability Assessment," *Applied Thermal*

Engineering, vol. 230, 120751, 2023.

[8] A. Iranpour Mobarakeh, R. Sadeghi, H. Saghafi Esfahani, and M. Delshad, "Optimal Planning and Operation of Energy Hub by Considering Demand Response Algorithms and Uncertainties Based on Problem-Solving Approach in Discrete and Continuous Space," *Electric Power Systems Research*, vol. 214, 108859, 2023.

[9] E. Akbari, S. F. Mousavi Shabestari, S. Pirouzi, and M. Jadidoleslam, "Network Flexibility Regulation by Renewable Energy Hubs Using Flexibility Pricing-Based Energy Management," *Renewable Energy*, vol. 206, pp. 295–308, 2023.

[10] Z. Qu, C. Xu, F. Yang, F. Ling, and S. Pirouzi, "Market Clearing Price-Based Energy Management of Grid-Connected Renewable Energy Hubs Including Flexible Sources According to Thermal, Hydrogen, and Compressed Air Storage Systems," *Journal of Energy Storage*, vol. 69, 107981, 2023.

[11] A. Karthikeyan, and V. Arun, "Enhancing Energy Hub Management with Unified Plug-In Electric Vehicle Based Demand Response and Energy Storage Systems," *Journal of Energy Storage*, vol. 108, 114997, 2025.

[12] Y. Pezhmani, and N. Rezaei, "Risk-Averse Energy Management of a Water-Heat-Power Virtual Energy Hub Considering Hosting Capacity and Volt-VAR Control of Distribution Network," *Energy*, vol. 318, 134949, 2025.

[13] L. Yan, X. Deng, and J. Li, "Integrated Energy Hub Optimization in Microgrids: Uncertainty-Aware Modeling and Efficient Operation," *Energy*, vol. 291, 130391, 2024.

[14] P. Hajiamoosha, A. Rastgou, and H. Afshar, "A Multi-Objective Framework for Smart Energy Hubs: Leveraging Compressed Air Storage and Demand Response," *Journal of Green Energy Research and Innovation*, vol. 2, no. 2, pp. 1–25, 2025.

[15] P. Hajiamoosha, A. Rastgou, S. Bahramara, and S. M. Bagher Sadati, "Stochastic Energy Management in a Renewable Energy-Based Microgrid Considering Demand Response Program," *International Journal of Electrical Power & Energy Systems*, vol. 129, 106791, 2021.

[16] G. A. Gómez-Ramírez, L. García-Santander, M. Zubiaga Lazkano, and C. Meza, "Increasing Flexibility in Vulnerable Power Grids Using Electrochemical Storage," *Heliyon*, vol. 10, no. 16, e35710, 2024.

[17] K. Chua, S. Chou, and W. Yang, "Advances in Heat Pump Systems: A Review," *Applied Energy*, vol. 87, no. 12, pp. 3611–3624, 2010.

[18] Y. Zhang, P. E. Campana, A. Lundblad, and J. Yan, "Comparative Study of Hydrogen Storage and Battery Storage in Grid Connected Photovoltaic System: Storage Sizing and Rule-Based Operation," *Applied Energy*, vol. 201, pp. 397–411, 2017.

[19] H. Maleki, M. S. Sepasian, M. R. Aghamohammadi, and M. Marzband, "Optimizing the Design of a Hydrogen Refueling Station Integrating Renewable Energy and Seawater Desalination: A Case Study in Southern Iran," *International Journal of Industrial Electronics Control and Optimization*, 2025.

[20] A. Olabi, T. Wilberforce, M. Ramadan, M. A. Abdelkareem, and A. H. Alami, "Compressed Air Energy Storage Systems: Components and Operating Parameters – A Review," *Journal of Energy Storage*, vol. 34, 102000, 2021.

[21] A. Azarhooshang, and A. Rezazadeh, "RETRACTED: Energy Management of Distribution Network with Inverter-based Renewable Virtual Power Plant Considering Voltage Security Index," *IET Renewable Power Generation*, vol. 18, no. 1, pp. 126–140, 2023.

[22] I. Gabrielaitienė, B. Bøhm, and B. Sundén, "Dynamic Temperature Simulation in District Heating Systems in Denmark Regarding Pronounced Transient Behaviour," *Journal of Civil Engineering and Management*, vol. 17, no. 1, pp. 79–87, 2011.

[23] F. Khalafian, N. Iliaee, et al., "Capabilities of Compressed Air Energy Storage in the Economic Design of Renewable Off-Grid System to Supply Electricity and Heat Costumers and Smart Charging-Based Electric Vehicles," *Journal of Energy Storage*, vol. 78, 109888, 2024.

[24] A. Maleki, and A. Askarzadeh, "Optimal Sizing of a PV/Wind/Diesel System with Battery Storage for Electrification to an Off-Grid Remote Region: A Case Study of Rafsanjan, Iran," *Sustainable Energy Technologies and Assessments*, vol. 7, pp. 147–153, 2014.

[25] M. R. Bussieck, and A. Meeraus, "General Algebraic Modeling System (GAMS)," *Applied Optimization*, pp. 137–157, 2004.

Declaration of competing interest

The authors declare that they have no known competing financial interests or personal relationships that could have appeared to influence the work reported in this paper. The ethical issues, including plagiarism, informed consent, misconduct, data fabrication and/or falsification, double publication and/or submission, redundancy, have been completely observed by the authors.

Bibliography

Ehsan Akbari received the B.Sc. degree in Electrical Power Engineering from Mazandaran University, Babolsar, Iran, in 2009 and M.S. degree in Electrical Power Engineering from Mazandaran University of Science and Technology, Babol, Iran, in 2014. He received Ph.D. in Electrical Power Engineering from Isfahan University of Technology, Isfahan, Iran in 2022. He is now a Assistant Professor at Department of Electrical Engineering, Mazandaran University of Science and Technology, Babol, Iran. He is the author of 25 books and more than 355 papers in reputed journals and conferences and won six patents in his research fields. He has obtained five provincial scientific and technological progress awards. His main areas of research are power quality, flexible AC transmission systems (FACTS), application of power electronics in power systems, power electronics multilevel converters, smart grids, control of grid-connected converters, fault location, distributed generation, energy storage systems, micro-grids, voltage stability, electrical machines, special electrical machinery, HVDC systems, harmonics, reactive power control using hybrid filters and renewable energy systems.

Email: e.akbari@ustmb.ac.ir
ORCID: 0000-0002-53185673

Contribution Statement: Conceptualization, Data curation, Formal analysis, Funding acquisition, Investigation, Methodology, Project administration, Resources, Software, Supervision, Validation, Visualization, Roles/Writing - original draft, Writing-review & editing.

Sasan Pirouzi received the B.Sc. degree in electrical engineering from Technical and Vocational University, Mashhad, Iran, in 2012, the M.Sc. degree from the Isfahan University of Technology, Isfahan, Iran, in 2014, and the Ph.D. degree from the Shiraz University of Technology (SUTECH), Shiraz, Iran, in 2017. His research interests include power system operation and planning, electric vehicles, DERs, and the application of optimization methods in power systems.

Email: s.pirouzi@sutech.ac.ir
ORCID: 0000-0001-5966-4432

Contribution Statement: Conceptualization, Data curation, Formal analysis, Funding acquisition, Investigation, Methodology, Project administration, Resources, Software, Supervision, Validation, Visualization, Roles/Writing - original draft, Writing-review & editing.

Abdolreza Behvandi was born in 1987 in Iran. He received his B.Sc., M.Sc., and Ph.D. degrees all in Electrical Engineering (Power Systems) in 2010, 2012, and 2019 from Isfahan University of Technology, Isfahan University, and Shahid Chamran University of Ahvaz, respectively. Currently, he is an Assistant Professor at Department of Electrical Engineering, Ramhormoz Branch, Islamic Azad University, Ramhormoz, Iran. His special interests are power system studies, power system protection, renewable energy, and microgrids.

Email: rezabehvandi@gmail.com
ORCID: 0000-0001-5966-4432

Contribution Statement: Data curation, Formal analysis, Investigation, Resources, Validation.

Journal of
Green Energy
Research and Innovation

Optimizing Distributed Energy Resources for Sustainable Solutions: A Multi-Objective Approach Based on Harmony Search Algorithm

Fardad Rastgou, Saman Hosseini-Hemati, Ashkan Mohammadi

Highlights

- **A multi-objective harmony search algorithm with Monte Carlo simulation minimizes costs and emissions under load and price uncertainties.**
- **The model optimizes six diverse energy resources to balance economic and environmental trade-offs using fuzzy decision-making.**
- **Results confirm that higher renewable energy penetration significantly reduces losses, cuts emissions, and improves system efficiency.**

Graphical Abstract

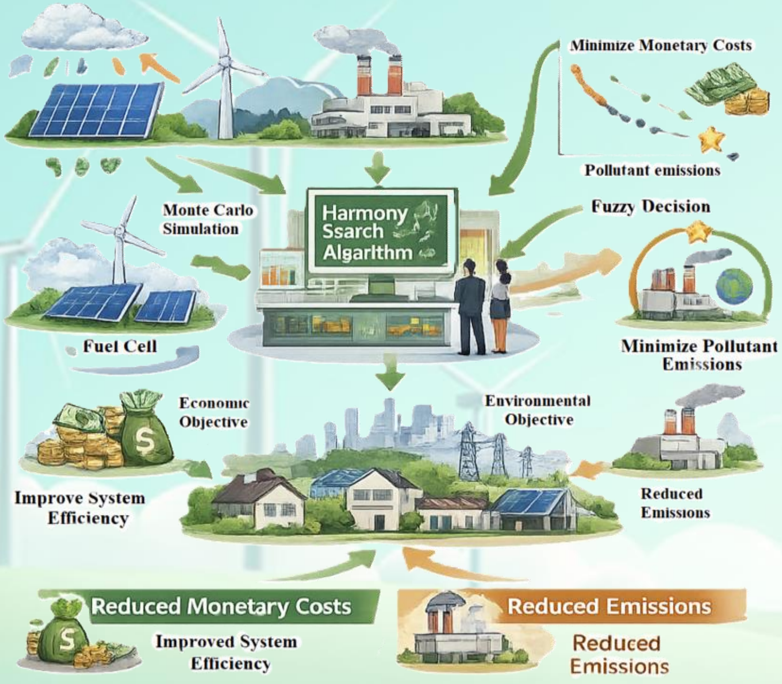

Citation
A. Rastgou, S. Hosseini-Hemati, and A. Mohammadi, "Optimizing Distributed Energy Resources for Sustainable Solutions: A Multi-Objective Approach Based on Harmony Search Algorithm," *Journal of Green Energy Research and Innovation*, vol. 3, no. 1, pp. 42-55, 2026.

https://doi.org/10.61882/jgeri.3.1.42

JGERI
Journal of Green Energy
Research and Innovation

Journal of Green Energy Research and Innovation 3.1 (2026) 42-55

Online ISSN: 3041-9018

Journal of Green Energy Research and Innovation

Journal Homepage: www.jgeri.araku.ac.ir

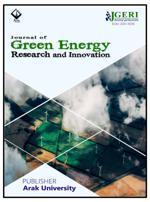

Optimizing Distributed Energy Resources for Sustainable Solutions: A Multi-Objective Approach Based on Harmony Search Algorithm

Fardad Rastgou [1,*] , Saman Hosseini-Hemati [1] , Ashkan Mohammadi [2]

[1] *Department of Electrical Engineering, Ker.C., Islamic Azad University, Kermanshah, Iran.*

[2] *Department of Electrical Engineering, IsG.C., Islamic Azad University, Eslamabad-E-Gharb, Kermanshah, Iran.*

ARTICLE INFO

Keywords:
Harmony search algorithm,
Optimization in power system,
Distributed energy resources,
Monte-Carlo simulation.

Article History:
Received: 02 April 2025;
Revised: 15 April 2025;
Accepted: 20 April 2025.

Article type:
Research Article

* ***Corresponding author***
E-mail address
fardad.rastgou@gmail.com (F. Rastgou)

ABSTRACT

This study introduces a comprehensive multi-objective harmony search algorithm designed to simultaneously minimize total monetary costs and pollutant emissions while explicitly accounting for uncertainties associated with electrical load demand and electricity market prices. To effectively capture and model these inherent uncertainties, a Monte Carlo simulation (MCS) framework is employed, enabling a probabilistic assessment of system behavior under varying operating conditions. The formulated optimization problem integrates six distinct types of distributed energy resources (DER), namely wind turbines, photovoltaic systems, fuel cells, micro-turbines, gas turbines, and diesel generators. This diverse portfolio of DER technologies allows the model to accurately reflect the operational flexibility and heterogeneity of modern distributed energy systems. Within the proposed multi-objective harmony search framework, a non-dominated sorting mechanism is applied to systematically classify candidate solutions and extract the Pareto-optimal front, thereby revealing the trade-offs between economic and environmental objectives. To further support practical decision-making, a fuzzy decision-making methodology is incorporated to identify the most suitable compromise solution from the set of Pareto-optimal alternatives, taking into account decision-makers' preferences and system priorities. The simulation results demonstrate that higher penetration of renewable energy sources plays a crucial role in reducing energy losses, mitigating environmental impacts, and improving overall system efficiency. These findings highlight the effectiveness of the proposed optimization framework in enhancing the economic and environmental performance of distributed energy systems under uncertainty.

1. Introduction

1.1. Motivation and aim

Optimal planning of distributed energy resources (DERs) plays a pivotal role in the development and operation of modern energy distribution networks, particularly in response to the growing demand for sustainable, reliable, and environmentally friendly energy solutions, as well as the urgent need to reduce dependence on fossil fuel–based generation. The integration of renewable energy sources (RESs), such as solar photovoltaic and wind power systems, significantly contributes to lowering greenhouse gas emissions, mitigating environmental impacts, and advancing long-term energy sustainability objectives. Moreover, the strategic allocation and optimal sizing of DERs in close proximity to consumption points lead to a substantial reduction in transmission and distribution losses, thereby enhancing overall system efficiency. Such localized generation also strengthens grid resilience by improving voltage profiles, increasing supply reliability, and providing greater flexibility in accommodating load variations. By enabling the effective utilization of locally available renewable resources, optimal DER planning supports a more decentralized, robust, and sustainable energy infrastructure capable of meeting future energy challenges. Advanced forecasting and modeling techniques ensure the effective deployment of DERs while maintaining grid stability.

Additionally, optimal DER planning fosters consumer empowerment through energy independence, enabling participation in generation via rooftop solar panels or community wind projects, which also supports local economic development and job creation in the renewable sector [1,2]. The DERs planning is crucial for modern energy distribution networks, as it reduces dependence on fossil fuels, lowers air pollution, and mitigates climate change impacts. By integrating RESs, this approach enhances grid efficiency and resilience while promoting consumer participation and local economic growth. Ultimately, effective DER integration is essential for achieving a cleaner, sustainable energy future and addressing urgent environmental challenges.

1.2. Literature review

The study presented in [3] introduces an advanced three-dimensional multi-objective optimization framework aimed at the optimal planning of distributed energy resources (DERs) alongside the effective management of electrical energy storage systems within distribution networks. This framework simultaneously considers multiple conflicting objectives, enabling a balanced trade-off between economic performance, technical reliability, and environmental impact. By incorporating the coordinated operation of DERs and storage systems, the proposed approach enhances operational flexibility, improves energy utilization efficiency, and supports more reliable and resilient distribution network planning under diverse operating conditions. In [4], a multi-objective planning strategy is introduced that takes into account the stochastic nature of customer-owned DERs. This approach concurrently tackles dynamic network reconfiguration, capacitor placement, and the dynamic adjustment of on-load tap changer transformers. The primary goal is to reduce power loss costs while enhancing the system's voltage profile by minimizing a newly proposed voltage consistency indicator presented in this study. Ref. [5] presents a comprehensive long-term stochastic mixed-integer single-level, single-stage nonlinear multi-objective optimization planning model specifically developed to facilitate the effective integration of distributed energy resources (DERs) into power distribution systems. This model captures the inherent uncertainties associated with long-term planning horizons while simultaneously addressing multiple conflicting objectives, thereby enabling more informed and robust decision-making for DER deployment. In [6], the authors investigate the coordinated and synergistic integration of RESs with battery energy storage systems, with the primary objective of improving the sustainability, operational reliability, and flexibility of modern power systems. By leveraging the complementary characteristics of renewables and storage technologies, the proposed approach enhances energy balancing capabilities and mitigates the adverse impacts of renewable intermittency. Furthermore, the study in [7] develops an optimization-based planning framework for the strategic placement and sizing of multiple DERs in conjunction with electric vehicle charging stations within distribution networks. This framework aims to accommodate the increasing penetration of electric vehicles while maintaining network performance, reducing operational costs, and ensuring efficient utilization of distributed energy assets. Additionally, [8] discusses various modeling and optimization methodologies for DERs, as well as control strategies for DERs and microgrids. Ref. [9] addresses stochastic energy management within a microgrid environment, taking into account RESs such as photovoltaic, wind, and tidal energy, along with demand response programs and storage solutions. In [10], a novel and comprehensive modeling approach is proposed that explicitly incorporates several practical and influential factors affecting distributed generation planning. These factors include pollutant emissions, capital investment costs, and operational expenses associated with distributed generators, as well as the cost of purchasing electricity from the main grid. In addition, the proposed framework accounts for dynamic planning aspects over the study horizon and addresses uncertainties arising from variations in load demand and electricity market prices. By integrating these considerations, the model provides a more realistic and robust decision-support tool for optimal planning and operation of distributed energy resources under real-world conditions. Ref. [11] focuses on establishing penetration limits for regulations within existing networks. As new electrification systems emerge, the integration of DERs necessitates new planning principles that consider the sizing and selection of network components such as feeder cables and transformer while accounting for various scenarios regarding DER uptake. Furthermore, it is crucial to address the uncertainties linked to the operation of these networks, particularly concerning the location and capacity of DERs. Ref. [12] proposes a comprehensive methodology for the optimal and coordinated allocation of wind farms, energy storage systems, and parking facilities for plug-in electric vehicles, while explicitly incorporating demand response programs and hourly distribution network reconfiguration under both normal operating conditions and severe contingency scenarios. In addition, this methodology evaluates the participation and behavior of different load types, providing a realistic representation of system demand dynamics and enhancing the operational flexibility and resilience of the distribution network. In [13], a multi-objective planning model for distributed energy resources is developed with the aim of achieving an effective trade-off between carbon emission reduction and economic cost minimization. By simultaneously addressing environmental and financial objectives, the proposed model supports sustainable planning decisions and promotes the integration of cleaner energy technologies within modern power systems. An innovative enhanced adaptive weighted-sum algorithm featuring a single sparse-preference parameter is introduced to generate a comprehensive Pareto front. Additionally, [14] proposes a three-objective capacity planning model for DERs that considers economic cost, carbon emissions, and voltage deviation. A comprehensive review about DER planning is stated in [15].

This paper presents a comprehensive probabilistic multi-objective framework designed to optimize the planning and deployment of DERs within distribution electricity networks. The proposed model is formulated from the viewpoint of the distribution company, ensuring that practical operational and economic considerations are fully reflected in the planning process. The mathematical formulation is based on nonlinear programming techniques, allowing the model to accurately capture the complex interactions and constraints inherent in modern distribution systems.

The proposed design aims to achieve an effective trade-off between minimizing total monetary costs and reducing pollutant emissions, while explicitly accounting for uncertainties associated with electrical load variations and fluctuations in electricity market prices. The monetary cost objective includes investment and operational costs of distributed generation (DG) units, compensation payments related to network losses, and expenditures incurred from purchasing electricity from the upstream grid.

To efficiently solve the resulting multi-objective optimization problem, the non-dominated sorting harmony search algorithm (NSHSA) is employed, enabling the identification of Pareto-optimal solutions. In addition, uncertainty analysis is conducted using the Monte Carlo simulation method, which provides a robust probabilistic assessment of system performance under varying stochastic conditions.

The NSHSA is a hybrid optimization technique that integrates two well-established and powerful methodologies [16], namely non-dominated sorting and the harmony search algorithm. This hybrid structure makes NSHSA particularly suitable for solving complex multi-objective optimization problems, in which the primary aim is to identify a set of optimal solutions that represent meaningful trade-offs among multiple, often conflicting, objectives. Rather than converging to a single solution, the algorithm seeks to generate a diverse collection of alternatives that collectively describe the Pareto-optimal front. Within NSHSA, the non-dominated sorting mechanism is employed to classify and rank candidate solutions according to the concept of Pareto dominance [17,18]. Under this framework, each solution is evaluated not only based on its individual objective values but also in comparison with other solutions in the population. A solution is defined as non-dominated if no other solution performs better across all objectives simultaneously. This ranking strategy enables the algorithm to preserve a diverse set of high-quality solutions, ensuring broad coverage of the Pareto front and facilitating a comprehensive exploration of the solution space. The harmony search component of NSHSA is inspired by the process of musical improvisation, in which musicians collaboratively seek harmonious sound patterns through experience, memory, and random variation [19]. Analogously, in the optimization context, new candidate solutions are generated by combining information from existing solutions, guided by harmony memory, pitch adjustment, and random selection mechanisms. This balance between exploitation of known good solutions and exploration of new regions of the search space enhances the algorithm's ability to avoid premature convergence. Furthermore, NSHSA dynamically adapts its search behavior based on solution performance, allowing for a flexible and efficient optimization process capable of handling nonlinear, multi-modal, and multi-objective problems effectively.

One of the primary advantages of the NSHSA lies in its strong capability to efficiently address multi-objective optimization problems. By simultaneously considering multiple conflicting objectives, NSHSA is able to generate a diverse set of Pareto-optimal solutions rather than converging to a single point. This feature allows decision-makers to clearly observe the trade-offs among objectives and select solutions that best align with technical, economic, or environmental priorities. Moreover, the integration of non-dominated sorting with the adaptive search mechanism of harmony search enhances both solution diversity and convergence speed, making NSHSA particularly effective for complex, nonlinear, and large-scale optimization problems. By combining non-dominated sorting with harmony search, NSHSA can effectively balance exploration and exploitation, leading to a robust search capability [20]. Additionally, the diversity maintained through non-dominated sorting helps prevent premature convergence to suboptimal solutions, ensuring that a wide range of potential solutions is considered. This makes NSHSA particularly suitable for complex real-world problems where multiple criteria must be optimized simultaneously, such as in engineering design, resource allocation, and scheduling tasks. Overall, NSHSA represents a significant advancement in multi-objective optimization techniques, leveraging the strengths of both non-dominated sorting and harmony search to achieve superior results. The novel contributions of this paper in comparison to prior research in the field can be outlined as follows:

- Introduction of a new multi-objective probabilistic framework for the planning of DERs by distribution companies operating in a competitive electricity market.
- Development of an effective scenario-based methodology to address uncertainties related to electricity prices and load demands.
- Simultaneous consideration of six distinct types of DERs, which include wind turbine (WT), photovoltaic (PV) system, fuel cell (FC), micro-turbine (MT), gas turbine (GT), and diesel engine (DE).
- Utilization of the NSHSA combined with a fuzzy decision-making approach to identify the optimal compromise solution from the set of Pareto optimal solutions.

1.3. Paper organization

The remainder of this paper is organized as follows. Section 2 describes the scenario-based modeling approach adopted to effectively address uncertainties associated with electricity pricing and load demand variations. Section 3 outlines the proposed probabilistic and multi-objective optimization framework developed for the optimal planning of distributed energy resources (DERs). The detailed mathematical formulation of the multi-objective optimization strategy and associated constraints is presented in Section 4. Section 5 provides a comprehensive analysis and discussion of the simulation results obtained from the studied primary distribution network. Finally, Section 6 concludes the paper by summarizing the main findings of the study and highlighting the practical implications and potential applications of the proposed approach.

2. Modeling uncertainties using scenario-based approaches

This paper focuses on various uncertainties that impact the planning of DERs, specifically addressing price and load uncertainties. The demand for electric power significantly influences the fluctuations in periodic electricity prices. Consequently, there is an increasing emphasis on analyzing the relationship between electricity prices and load demands.

A critical feature of electricity generated from RESs such as solar and wind is its intermittent availability, particularly during peak demand periods. From an economic perspective, ensuring system adequacy, defined as the ability to provide sufficient capacity to reliably meet peak demand, means that electricity holds greater value during these peak hours.

Therefore, it is essential to establish a correlation between electricity load profiles and price dynamics. However, it is important to note that this paper does not account for the correlation between load and price. The modeling strategy proposed herein is outlined as follows.

2.1. *Modeling electricity prices based on different scenarios*

In competitive electricity markets, distribution companies are obligated to purchase electrical energy directly from the market. Due to the highly dynamic and uncertain characteristics of these markets, electricity prices exhibit significant fluctuations over time, which introduces considerable uncertainty into operational and planning decisions. As a result, accurate anticipation of future market prices is essential for distribution companies to effectively schedule their short-term operations and long-term planning strategies. Nevertheless, the stochastic and volatile behavior of market prices makes reliable forecasting challenging, and prediction errors can substantially affect both operational performance and planning outcomes. To mitigate the impacts of price uncertainty, a scenario-based modeling approach that combines fuzzy C-means clustering with Monte Carlo simulation (FCM/MCS) is adopted to represent variations in electricity market prices. In this framework, the statistical properties of price behavior are captured through scenario generation rather than relying on a single forecast. It should be noted that the estimation of key statistical parameters, such as the expected value and variance of electricity prices, is commonly performed using advanced forecasting methods, including time series techniques and artificial neural network models.

Initially, using the forecasted mean and variance of prices, a set of np price samples is generated through Monte Carlo simulation, with each scenario assigned an equal probability of $1/n_p$. Although generating a large number of price samples enhances the representation of the uncertain model, it also results in a stochastic program that may become excessively large and difficult to solve. Therefore, a balance must be struck between achieving a good approximation and managing computational complexity. Consequently, various scenario reduction methods have been introduced in the literature to limit the total number of generated scenarios while maintaining the essential statistical properties of electricity price behavior. These techniques aim to improve computational efficiency by discarding scenarios with negligible occurrence probabilities and consolidating those that exhibit similar characteristics into representative groups, thereby preserving the overall stochastic structure of the problem. In this context, the FCM technique serves as the primary method for price scenario reduction. FCM is utilized to cluster n_p randomly generated samples into a specified number of clusters. By definition, a cluster comprises objects that are similar to one another but dissimilar to those in other clusters. Thus, the center of each cluster can effectively represent similar price scenarios within that cluster. Accordingly, FCM serves as an effective complement to the Monte Carlo simulation framework by transforming the initially generated set of n_p random price samples at each time interval into a smaller set of n_r representative and distinct scenarios. This reduction process retains the diversity of price behavior while significantly decreasing computational complexity. The occurrence probability assigned to each reduced price scenario is then calculated using the following approach [21]:

$$P_M = \frac{n_c}{n_p}, \quad M = 1, 2, \ldots, n_r \tag{1}$$

Consequently, a price scenario that serves as the center of a cluster with a greater number of members is considered to have a higher probability than other scenarios.

2.2. *Scenario-based modeling of electrical loads*

To properly reflect inaccuracies in load forecasting, it is necessary to explicitly model load-related uncertainties within the analytical framework. This requires identifying an appropriate probability distribution to represent load forecast errors. In this study, the load forecasting error is assumed to follow a Gaussian distribution, with its mean equal to the predicted peak demand that the distribution company is required to supply. Figure 1 depicts the continuous probability density function associated with the system load forecasting error, which is subsequently discretized into seven distinct intervals. Each interval spans a range equivalent to one standard deviation of the load forecast error, consistent with the methodology adopted in [22,23]. To produce representative load scenarios corresponding to different forecasted demand levels and their associated probabilities obtained from the defined probability distribution function, a roulette wheel selection technique is applied, as outlined in [24]. This probabilistic sampling approach enables the systematic generation of load scenarios in proportion to their likelihood of occurrence. At the first stage, the interval [0,1] is partitioned according to the normalized probabilities assigned to each load level, as illustrated in Figure 2. Next, a random value is drawn uniformly from the interval [0,1].

If the generated random value lies within the normalized probability segment associated with a particular load forecast level on the roulette wheel, that load level is selected as a representative scenario. By repeatedly applying this probabilistic selection procedure, a sufficient and diverse set of load scenarios is gradually constructed. The integration of the roulette wheel selection method with the Monte Carlo simulation framework forms a hybrid scenario generation approach, commonly referred to as the RW/MCS technique, which enables efficient and statistically consistent modeling of load uncertainties.

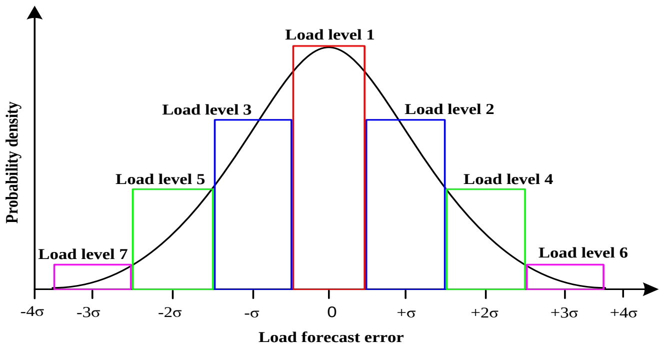

Figure 1. A standard approach involves discretizing the continuous probability distribution of the load forecast error into seven intervals.

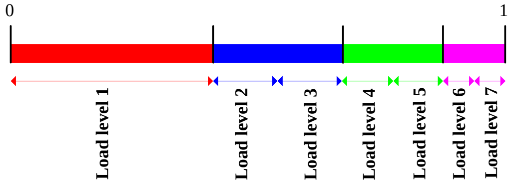

Figure 2. The roulette wheel mechanism is utilized for the normalized probabilities of load forecast levels.

3. Problem formulation

This section develops the formulation of a multi-objective optimal planning problem for distributed energy resources. The proposed framework is expressed as a nonlinear programming model, allowing for the accurate representation of the complex interactions and constraints inherent in the planning and operation of distributed energy systems.

3.1. *Objective functions*

The economic objective function in the planning problem of DERs aims to minimize the investment and operational costs associated with DERs, as well as the expenses related to loss compensation services and payments for purchased power by the distribution company. The monetary objective function is represented by Equations (2) and (3) [21]:

$$f_1 = \sum_s \pi_s \left(\begin{array}{l} \sum_i \sum_k \left(C_k^{INV} S_B P_{s,i,k}^{OP} \right) + 8760 \times \sum_t \sum_i \sum_k \left(\left(\frac{1}{1+d} \right)^t C_k^{OP} S_B P_{s,i,k}^{OP} \right) + \\ 8760 \times \sum_t \left(\left(\frac{1}{1+d} \right)^t P_{s,ij}^{Loss} S_B \rho_s \right) + 8760 \times \sum_t \left(\left(\frac{1}{1+d} \right)^t \sum_n P_{s,n}^{PP} S_B \rho_s \right) \end{array} \right) \quad (2)$$

$$\forall s \in \{1,\ldots,NS\},\ \forall t \in \{1,\ldots,NT\},\ \underset{i \neq j}{\forall}\, i \in \{1,\ldots,NB\}$$

$$\forall k \in \{\mathrm{WT,PV,FC,MT,GT,DE}\},\ \forall n \in \{1,\ldots,NSS\}$$

where

$$P_{s,ij}^{Loss} = \sum_i \sum_j \left(\frac{\left(|V_{s,i}| - |V_{s,j}| \right)^2}{|Z_{ij}|} \right) \times \cos\varphi \quad (3)$$

$$\underset{i \neq j}{\forall}\, i \in \{1,\ldots,NB\},\ \underset{i \neq j}{\forall}\, j \in \{1,\ldots,NLB\}$$

In Equation (2), C_k^{OP} encompasses both fixed and variable components of operating costs. The fixed components consist of the costs associated with operation and maintenance, while the variable components pertain to fuel expenses. Furthermore, to appropriately capture the trade-off between locally generated electricity, especially the variable and emission-free power produced by solar and wind–based DERs, and energy purchased from the upstream grid, the emission minimization objective function is defined as shown in Equation (4) [21]:

$$f_2 = \sum_s \pi_s \left(\begin{array}{l} \sum_i \sum_k \left(8760 \times P_{s,i,k}^{OP} \times S_B \times \sum_m E_{k,m}^{DER} \right) + \\ \sum_n \left(8760 \times P_{s,n}^{PP} \times S_B \times \sum_m E_m^G \right) \end{array} \right) \quad (4)$$

$$\forall s \in \{1,\ldots,NS\},\ \forall n \in \{1,\ldots,NSS\},\ \forall i \in \{1,\ldots,NB\}$$

$$\forall k \in \{\mathrm{WT,PV,FC,MT,GT,DE}\},$$

$$\forall m \in \{\mathrm{SO_2,NO}_x\mathrm{,CO,CO_2,PM_{10}}\}$$

In modern energy system planning and operation, a wide range of effective measures are available to mitigate pollutant emissions. These measures include shifting energy production away from fossil fuel–based technologies toward RESs, improving overall energy efficiency across generation and consumption sectors, adopting market-based mechanisms such as carbon taxation, and enabling emission trading schemes between public and private stakeholders. Such approaches provide both regulatory and economic pathways for controlling emissions while maintaining system performance.

Within optimization-based planning frameworks, marginal emission abatement costs can be estimated directly from the optimization outcomes, offering valuable insight into the economic trade-offs associated with emission reduction strategies. In multi-objective planning models, the weighting factors assigned to the emission-related objective function can be carefully tuned so that the resulting marginal abatement costs are consistent with long-term emission price targets and policy expectations defined by decision makers. As a result, planners are required to determine the appropriate level of clean energy deployment or procurement by balancing the operational and societal benefits of electricity generation against the financial penalties associated with surpassing allowable emission thresholds. This process enables informed decision-making that aligns environmental goals with economic feasibility.

3.2. Constraints

The objective functions associated with DER planning are optimized subject to a set of technical and operational constraints to guarantee realistic and feasible planning solutions. These constraints encompass limitations related to the operational capacities of DER units, the maximum allowable capacities of distribution substations, the thermal loading limits of distribution feeders, and the fundamental requirements of power balance and conservation within the network. Each of these constraints plays a critical role in maintaining system reliability and operational security and is described and analyzed in detail in the following subsections [21].

a) Operational capacity of DER: This constraint, as shown in Equation (5), refers to the maximum power output that the DER can deliver under normal operating conditions. It ensures that the generation from the DER does not exceed its rated capacity, which is crucial for maintaining grid stability and reliability.

$$P^{OP}_{s,i,k} \times S_B \le P^{CAP}_{k} \tag{5}$$

$$\forall s \in \{1,\ldots,NS\},\ \ \forall i \in \{1,\ldots,NB\}$$

$$\forall k \in \{\mathrm{WT}, \mathrm{PV}, \mathrm{FC}, \mathrm{MT}, \mathrm{GT}, \mathrm{DE}\},$$

b) Distribution substation capacity: This constraint, as shown in Equation (6), defines the maximum load that a distribution substation can handle. It limits the total amount of power that can be supplied to the distribution network from the substation, ensuring that it does not exceed its designed capacity and avoiding potential overloads.

$$P^{SS}_{n} \le P^{SS-MAX}_{n},\quad \forall n \in \{1,\ldots,NSS\} \tag{6}$$

c) Thermal capacity of distribution feeder: This constraint, as shown in Equation (7), refers to the maximum current that a distribution feeder can carry without overheating. It ensures that the thermal limits of the feeder are not exceeded, which could lead to equipment damage or failure.

$$P_{s,ij} \times S_B \le P^{MAX}_{ij}, \tag{7}$$

$$\forall s \in \{1,\ldots,NS\},\ \underset{i\neq j}{\forall}\, i \in \{1,\ldots,NB\},$$

$$\underset{i\neq j}{\forall}\, j \in \{1,\ldots,NLB\}$$

d) Power balance limits: This constraint, as shown in Equation (8), ensures that the total power generated in the system equals the total power consumed, maintaining equilibrium in the network. It is essential for preventing over-generation or under-generation scenarios, which can affect system stability.

$$\left\{\sum_{j}\left\{P_{s,ij} - P^{Loss}_{s,ji}\right\} - \sum_{j} P_{s,ij} + \sum_{k} P^{OP}_{s,i,k}\right\} \times S_B = D_{s,i} \tag{8}$$

$$\forall s \in \{1,\ldots,NS\},\ \forall i \in \{1,\ldots,NB\},\ \underset{i\neq j}{\forall}\, j \in \{1,\ldots,NLB\},$$

$$\forall k \in \{\mathrm{WT},\mathrm{PV},\mathrm{FC},\mathrm{MT},\mathrm{GT},\mathrm{DE}\},$$

4. Solution methodology

4.1. NSHSA

In this study, the proposed multi-objective optimization framework is addressed using the Harmony Search Algorithm enhanced with a non-dominated sorting mechanism. This approach is particularly well suited to distribution network expansion planning problems, as it retains high computational efficiency when dealing with non-convex and complex solution spaces. Moreover, one of its key strengths is the ability to generate the entire Pareto-optimal front within a single execution of the algorithm, eliminating the need for repeated runs with different weighting factors. The underlying principle of this algorithm relies on organizing candidate solutions into multiple hierarchical levels based on their degree of optimality. Solutions assigned to the first level represent quasi-optimal outcomes over the entire feasible solution space, as they are not dominated by any other alternatives.

Subsequent levels consist of solutions that are quasi-optimal within the reduced solution space obtained after excluding solutions from higher-ranked levels. This ranking procedure continues iteratively, progressively categorizing solutions according to their relative performance across the multiple objectives. Figure 3 provides a graphical illustration of this Pareto-based classification process, highlighting the distribution of solutions across different optimality levels.

As shown in Figure 3, only three Pareto levels are depicted for illustrative purposes. Once all candidate solutions are classified into their respective Pareto levels, a fitness value is assigned to the solutions within each level using randomly generated numbers. These fitness values serve as a quantitative measure for guiding the search process of the algorithm. Solutions located on the first Pareto level are given the highest fitness values, while progressively smaller fitness values are allocated to solutions in the subsequent levels. It should be noted that there is no strict rule governing the exact numerical assignment of these fitness values; the only requirement is that solutions in higher-ranked Pareto levels receive larger fitness values than those in lower-ranked levels, thereby preserving the dominance hierarchy among solutions.

In addition to Pareto ranking, a secondary control parameter used for evaluating and ranking candidate solutions is the crowding distance metric. This concept is introduced to preserve diversity among solutions by measuring the density of neighboring solutions surrounding a particular option. Specifically, when a solution is located in a densely populated region of the Pareto front, its fitness value is reduced, whereas solutions situated in sparsely populated regions are favored. As illustrated in Figure 4, consider a set of Pareto-optimal solutions in which the $(i-1)$th and $(i+1)$th solutions are the immediate neighbors of the ith solution along the Pareto front. The crowding distance associated with the ith solution is then calculated using Equation (9), which quantifies the relative spacing between adjacent solutions and ensures a well-distributed and diverse Pareto front.

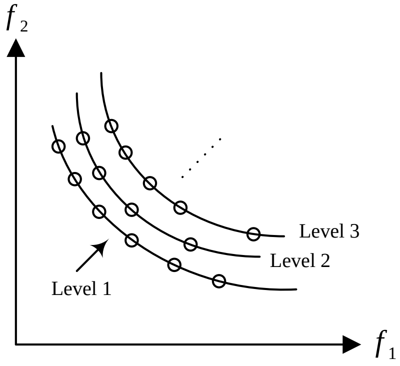

Figure 3. Dividing options into multiple Pareto levels.

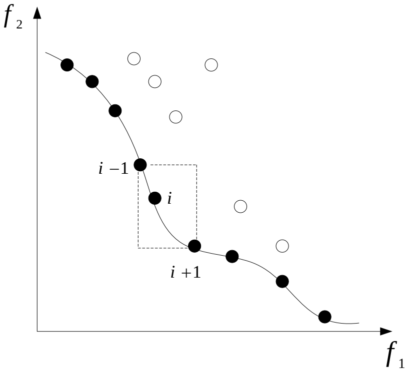

Figure 4. Definition of crowding distance.

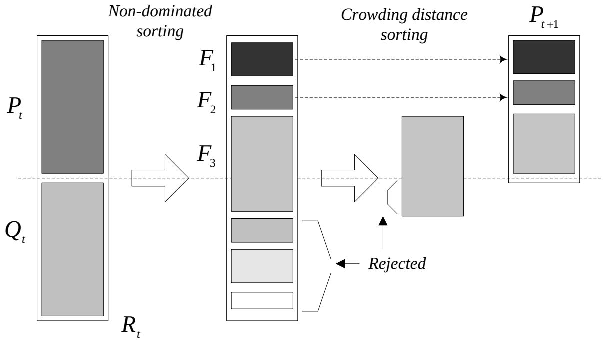

Figure 5. The process of selecting the best vector from among the alternatives.

$$d_i = d_i^1 + d_i^2, \quad d_i^1 = \frac{f_1(x_{i+1}) - f_1(x_{i-1})}{f_1^{\max} - f_1^{\min}}, \quad d_i^2 = \frac{f_2(x_{i-1}) - f_2(x_{i+1})}{f_2^{\max} - f_2^{\min}} \tag{9}$$

In a bi-objective competition, solution i is considered superior to solution j if any of the following conditions are met:

- The rank of i is lower than the rank of j ($r_i < r_j$).
- If solution i has the same rank as j, then solution i is superior to solution j if the crowding distance of solution i is greater than the crowding distance of solution j ($d_i > d_j$).

Following the completion of the Pareto ranking process and the computation of crowding distances, a new population vector of candidate solutions is constructed. This updated set of options reflects both solution optimality and diversity and serves as the basis for subsequent stages of the optimization procedure. Then, using common methods employed in harmony search algorithms, new options are generated from this new harmony, and the previous steps are repeated. Figure 5 illustrates the process of selecting the superior vector from among the options.

According to the above figure, at the beginning of each iteration, a vector from the harmony memory (Q_t) is generated using conventional methods of the harmony search algorithm. Then, all vectors ($R_t = P_t \cup Q_t$) are sorted and divided into different levels of Pareto. The number of members in this combined vector is equal to 2N, where N is the number of members in the initial vector selected by the planner. From the vector R_t, the top N options are selected based on priority and sent to the $(t+1)$-th iteration, and this process continues until the stopping condition is met. Given the method used to form the new vector, it is evident that an elitist approach is employed, as suitable solutions from the previous iteration are carried over unchanged to the next iteration. The stopping condition can be defined in various ways, including setting a maximum number of iterations.

Non-dominated sorting is a fundamental mechanism in multi-objective optimization frameworks. A candidate solution is regarded as non-dominated when no other solution outperforms it simultaneously across all objective functions. This procedure entails assessing an entire population of solutions and organizing them into multiple layers, or fronts, according to their dominance relationships. The first front comprises solutions that are not dominated by any others in the population, representing the best trade-offs among objectives. The second front includes solutions that are dominated only by those in the first front, while remaining mutually non-dominating, and this hierarchical sorting continues for subsequent fronts. Such a structured classification plays a crucial role in directing the optimization process toward the Pareto-optimal region while ensuring sufficient diversity among the generated solutions.

4.2. Harmony Search Mechanism

The harmony search algorithm is inspired by the musical improvisation process, in which musicians collaboratively strive to achieve a harmonious sound by continuously tuning and adjusting their instruments based on experience, memory, and creative variation. In NSHSA, a harmony memory (HM) stores a set of potential solutions (harmonies), and new solutions are generated through a combination of existing harmonies. The generation process involves three main operations: pitch adjustment, harmony memory consideration, and random selection.

1. Pitch Adjustment: This operation allows for fine-tuning of solutions by making small perturbations, helping to explore the solution space more thoroughly.
2. Harmony Memory Consideration: Solutions from the harmony memory are selected based on a probability distribution, promoting the retention of high-quality solutions.
3. Random Selection: Occasionally, new random solutions are introduced to maintain diversity and avoid premature convergence.

4.3. Important Parameters

Several parameters significantly influence the performance of NSHSA:

1. Harmony Memory Size (HMS): This parameter determines the number of solutions stored in the harmony memory. A larger HMS can provide a richer set of solutions but may slow down convergence, while a smaller HMS may lead to faster convergence but less diversity.
2. Harmony Memory Considering Rate (HMCR): This rate indicates the probability of selecting a solution from the harmony memory when generating new solutions. A higher HMCR encourages exploitation of known good solutions, while a lower HMCR promotes exploration.
3. Pitch Adjustment Rate (PAR): This parameter defines the likelihood that a generated solution will undergo pitch adjustment. A higher PAR allows for more exploration around existing solutions, while a lower PAR may focus more on exploitation.
4. Number of Iterations: The total number of iterations or generations affects the algorithm's ability to converge to optimal solutions. More iterations can lead to better results, but at the cost of increased computational time.
5. Diversity Maintenance: Techniques such as crowding distance or niche formation can be incorporated to maintain diversity among non-dominated solutions in the population, preventing convergence to a single solution.

In conclusion, the NSHSA provides a powerful and reliable framework for addressing multi-objective optimization problems through the seamless integration of non-dominated sorting techniques with the adaptive search mechanisms of the harmony search algorithm. By appropriately adjusting its control parameters and systematically applying non-dominated sorting, NSHSA is capable of thoroughly exploring the feasible solution space and producing a well-distributed set of Pareto-optimal solutions that clearly reflect the inherent trade-offs among competing objectives.

4.4. Fuzzy decision-making

Fuzzy-based decision-making offers a practical and flexible framework for managing multi-objective problems, especially in situations where objectives are inherently conflicting and subject to uncertainty. In the context of multi-objective optimization, decision-makers are frequently confronted with the difficulty of choosing a single preferred alternative from a collection of Pareto-optimal solutions, each of which embodies a different balance among competing objectives. Fuzzy decision-making provides a framework to incorporate subjective preferences and imprecise information into the decision-making process. By utilizing fuzzy logic, decision-makers can express their preferences more flexibly, allowing for the representation of vague or ambiguous criteria that may not be easily quantifiable. This is particularly important in multi-objective scenarios where stakeholders may have differing priorities or values. To select a satisfactory solution from the Pareto front using fuzzy decision-making, decision-makers can define fuzzy membership functions for each objective, reflecting their level of satisfaction with different outcomes. These functions help to evaluate and rank the Pareto-optimal solutions based on how well they align with the decision-makers' preferences.

The incorporation of fuzzy logic allows for a more nuanced understanding of trade-offs and helps to identify solutions that are acceptable to all planners involved. Ultimately, fuzzy decision-making facilitates a collaborative approach, ensuring that the selected solution not only meets the objectives but also resonates with the diverse perspectives of all stakeholders, leading to a more widely accepted and robust decision.

To determine the most appropriate compromise solution from the Pareto-optimal set produced by the NSHSA method, a fuzzy-based decision-making strategy is applied. Within this framework, a linear fuzzy membership function is constructed for each objective of the multi-objective optimization model. For objective functions formulated as minimization problems, the corresponding membership function is expressed according to Equation (10) [21]:

$$\mu_i^k = \begin{cases} 1 & f_i^k \le f_i^{\min} \\ \dfrac{f_i^{\max} - f_i^k}{f_i^{\max} - f_i^{\min}} & f_i^{\min} \le f_i^k \le f_i^{\max} \\ 0 & f_i^k \ge f_i^{\max} \end{cases} \tag{10}$$

For objective functions formulated with a maximization goal, the associated fuzzy membership function is defined as given in Equation (11).

$$\mu_i^k = \begin{cases} 0 & f_i^k \le f_i^{\min} \\ \dfrac{f_i^k - f_i^{\min}}{f_i^{\max} - f_i^{\min}} & f_i^{\min} \le f_i^k \le f_i^{\max} \\ 1 & f_i^k \ge f_i^{\max} \end{cases} \tag{11}$$

In this framework, f_i^k and μ_i^k represent the value of the ith objective function and its associated membership degree for the kth Pareto-optimal solution, respectively. The membership function quantifies the level of satisfaction or desirability of the ith objective within the corresponding Pareto solution. The comprehensive membership degree of the kth Pareto-optimal solution, denoted by μ_k, is obtained by combining its individual objective membership values in accordance with Equation (12) [21]:

$$\mu^k = \frac{\sum_{i=1}^{p} w_i \times \mu_i^k}{\sum_{i=1}^{p} w_i} \tag{12}$$

The weight factors w_i utilized in Equation (12) play a crucial role in the decision-making process. For the multi-objective DER planning problem, these weight factors can be determined by the distribution company according to the significance of both monetary costs and emissions. The Pareto solution that exhibits the highest membership function μ^k is deemed the most favorable option based on the selected weight factors, and therefore, it is chosen as the final solution to the multi-objective optimization problem.

5. Numerical results

5.1. 9-Node primary distribution system

This paper reports simulation outcomes obtained from a 9-node primary distribution benchmark network. The structural layout of the test system is depicted in Figure 6. The network consists of a single 132 kV/33 kV substation situated at node 9, which has a rated capacity of 40 MVA and supplies eight aggregated load points connected to nodes 1 through 8 under normal operating conditions.

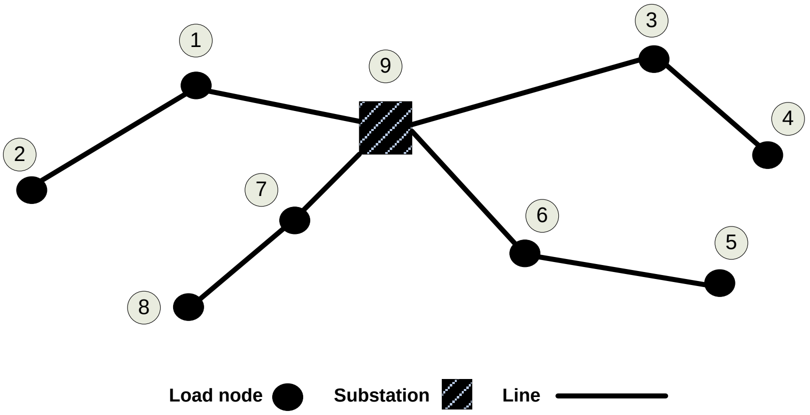

Figure 6. The 9-bus test distribution network.

The numerical simulations conducted for this test system utilize data sourced from [25]. A peak load of 51.1 MVA is projected and must be accommodated. Six different types of DERs are considered in the analysis, including wind turbines, photovoltaics, fuel cells, micro turbines, gas turbines, and diesel engines. The specifications for these DERs are derived from [21], and they are detailed in Tables 1 and 2.

To construct representative scenarios for load demand and electricity prices, the procedure described in Section 2 is applied. In this study, the electricity market price during peak load hours is assumed to be fixed at 70 USD per MWh. Furthermore, for all subsequent simulation cases, the system power factor is considered to be unity in order to simplify the analysis and focus on active power exchanges. At the initial stage of the assessment, the emission factor corresponding to electricity purchased from the upstream grid is assumed to be insignificant.

To extract the set of Pareto-optimal solutions, the NSHSA is executed using the following parameter settings: harmony memory size (HMS) equal to 40, harmony memory consideration rate (HMCR) of 0.99, pitch adjustment rate (PAR) of 0.001, and a maximum iteration number $N$of 200. The obtained non-dominated solutions are presented in Figure 7, which clearly illustrates the trade-off relationship between the economic objective and the environmental objective, highlighting the balance between cost minimization and emission reduction.

The Pareto optimal solutions presented in Figure 7 indicate that a reduction in daily emissions correlates with an increase in the total cost of DER planning, and conversely, an increase in emissions results in lower planning costs. This suggests that the adoption of clean DER technologies aimed at reducing emissions will lead to higher overall DER planning costs. The overall cost associated with DER planning is observed to vary between 163.02 and 225.025 million USD across the set of Pareto-optimal solutions. The normalized fuzzy membership function defined in Equation (12) provides a systematic tool to support decision-makers in identifying the most appropriate compromise solution among these alternatives. It should be emphasized that the weighting coefficients used in the fuzzy membership aggregation can be flexibly adjusted to reflect the relative importance assigned to each objective by the decision-maker. One commonly adopted approach for determining such weights is the analytical hierarchy process (AHP). Nevertheless, in the present analysis, equal importance is assigned to the economic and environmental objectives, resulting in weighting factors of $w_1 = w_2 = 0.5$.

Table 1. Data of six DG technologies.

DG	Unit size (kW)	Installed capacity Limit (kW)	Investment cost ($/kW)	Operation cost ($/kWh)
DE	1000	2000	500	0.045
FC	1500	3000	3500	0.050
GT	1000	4000	1000	0.040
MT	200	2000	1500	0.050
PV	100	2000	5000	0.005
WT	1000	4000	4500	0.010

Table 2. Emission of pollutant rates of six DG technologies.

DG	NOX (kg/kWh)	SO2 (kg/kWh)	CO2 (kg/kWh)	CO (kg/kWh)	PM10 (kg/kWh)
DE	0.00213	0.00125	0.625	0.0028	0.00036
FC	0.000015	0.000024	0.447	0	0
GT	0.00029	0.000032	0.625	0.00042	0.000041
MT	0.0002	0.000037	0.725	0.00047	0.000041
PV	0	0	0	0	0
WT	0	0	0	0	0
Grid	0.0022952	0.0035834	0.92125	-	-

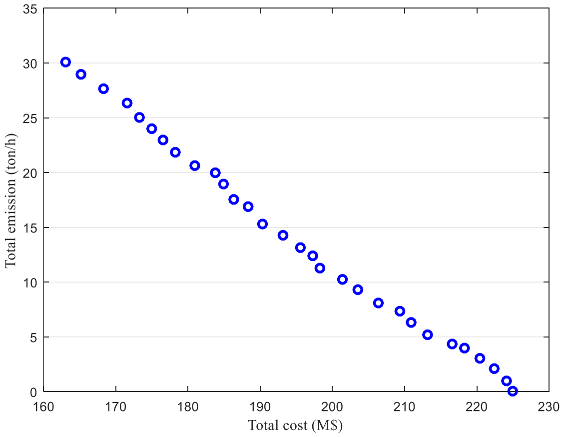

Figure 7. Pareto front of case study.

By applying the fuzzy decision-making framework described in Equation (12) with equal weights for both objectives, the optimal compromise solution for DER planning is obtained, as reported in Table 3. For this selected solution, the total economic cost, encompassing investment and operational expenditures of DER units, electricity procurement costs, and network energy losses, is estimated to be 185.6 million USD. Simultaneously, the corresponding environmental performance is evaluated at 13.1 tons per hour, reflecting a balanced trade-off between economic efficiency and emission mitigation.

To demonstrate the effectiveness of the proposed method, a comparison is made with the NSGA II (population size = 300, Mutation rate = 0.95, crossover rate = 0.8) and NSPSO (number of particles = 300, cognitive learning rate = 1.5, social learning rate = 1.1, inertia weight = 0.85) methods, as illustrated in Figure 8. For evaluating the Pareto solutions of the multi-objective methods, two indices are employed: the diversity measure and the ideal distance mean. The first index, as defined in Equation (13), indicates the diversity of the solutions; a larger value signifies better diversity. The second index, according to Equation (14), reflects the quality of the solutions in relation to their proximity to the average optimal solution, where a smaller value indicates superior quality of the Pareto solutions.

$$\mathrm{DM}=\sqrt{\sum_{i=1}^{M}\left(\max_{j=1,\ldots,N_P}\{f_i^{\,j}\}-\min\{f_i^{\,j}\}\right)^2} \tag{13}$$

$$\mathrm{MID}=\frac{\sum_{j=1}^{N_P} C_j}{N_P},\quad C_j=\sqrt{\sum_{i=1}^{M}\left(f_i^{\,j}-f_{i,\mathrm{m}}\right)^2} \tag{14}$$

In this context, N represents the number of Pareto solutions, M denotes the number of objective functions, $f_i^{\,j}$ is the value of the objective function i for solution j, and $f_{i,m}$ indicates the average value of the Pareto solutions for objective function i. Table 4 presents a comparison of the proposed method's solutions with those obtained from the mentioned algorithms. As shown in Table 4, the parameters for the proposed method outperform those of the other algorithms, demonstrating the effectiveness of the proposed approach.

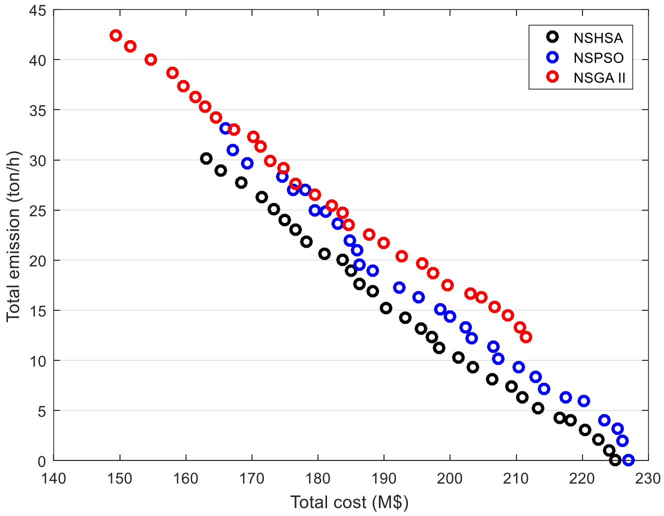

Figure 8. Pareto solutions of other algorithms used in solving the applied multi-objective model.

Table 3. The best compromised solution.

	Type, size (MW), and location of planned DERs					
	WT	PV	FC	MT	GT	DE
Total planned capacity	2,1	1,1	-	-	3,1,1,1,1,1,1,2	2,2,2,2,2,2,2,2
Bus	1,7	1,7	-	-	1,2,3,4,5,6,7,8	1,2,3,4,5,6,7,8

Table 4. Comparison of the parameters of diversity size and ideal mean distance in the multi-objective model.

Algorithm	Diversity size	Ideal mean distance
NSHSA	163.312	59.3277
NSPSO	161.987	60.6121
NSGA-II	161.691	61.8124

5.2. A real distribution system in Iran

The effectiveness of the proposed methodology is further demonstrated through its application to a real-world segment of the Iranian distribution power system, where it is used to compare the existing historical expansion strategy with a newly developed expansion plan derived from the proposed framework. A simplified schematic of the selected portion of the Iranian 20 kV distribution network is presented in Figure 9.

The studied system consists of a single distribution substation, 72 distribution lines, and 47 network nodes. The planning problem is formulated over a five-year horizon, during which a total load increase of 15% is anticipated. One candidate distribution substation with a rated capacity of 4 MVA is available for potential installation, while all existing feeders are considered eligible for either reinforcement or new construction, depending on the planning outcomes. As indicated in Figure 9, four candidate sites for distributed generation installation are identified and labeled as “a,” “b,” “c,” and “d.”

For the purposes of this case study, several system parameters are specified. The power factor is assumed to be 0.992, the system base power is set to 100 MVA, the discount rate is taken as 10%, and the electricity price is fixed at 0.07 USD per kWh. In addition, the thermal capacities of the lines connecting nodes “a”–“b,” “b”–“c,” and “c”–“d” are each assumed to be 4 MW. Additional technical and network-related data for this distribution system are available in [10]. The resulting optimal expansion plan obtained using the proposed approach is summarized in Table 5.

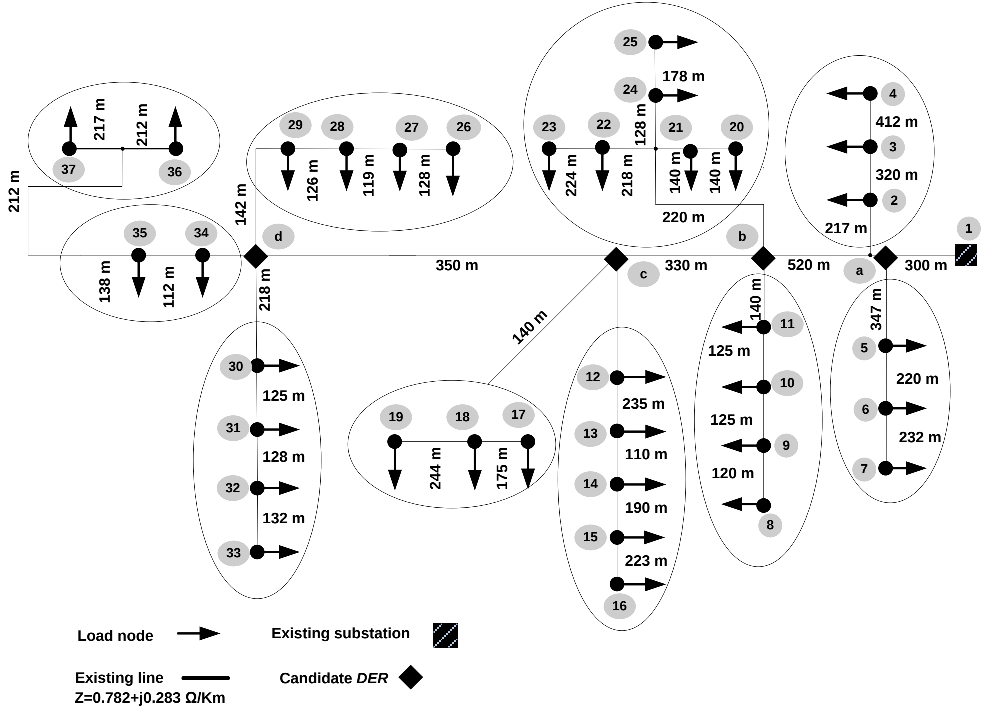

Figure 9. Single-line diagram of part of the 20 kV distribution network.

Table 5. Optimal expansion planning for system (6).

Node	DG	Type, size, and location of planned DGs					
		WT	PV	FC	MT	GT	DE
a	OG*	2000	-	-	-	-	1000
	PC*	2 × 1000	-	-	-	-	1 × 1000
b	OG	-	-	-	-	-	-
	PC	-	-	-	-	-	-
c	OG	-	-	-	-	-	2000
	PC	-	-	-	-	-	2 × 1000
d	OG	-	-	-	-	-	1000
	PC	-	-	-	-	-	1 × 1000

Investment cost (M$): 11
Operation cost (M$): 8.7864
Cost of purchased power (M$): 0.0025
Pollution (ton/h): 2.4262
Losses (p.u.): 0.011227
Losses without DGs: 0.001154
* OG: operating generation
* PC: planned capacity

6. Conclusion

In conclusion, this paper introduces a novel probabilistic multi-objective framework for optimizing DERs in distribution electricity networks. It utilizes nonlinear programming to address the needs of distribution companies in a competitive market, balancing monetary costs and pollutant emissions while managing uncertainties in electrical load and market prices. The model employs an NSHSA for efficient solution exploration, combining non-dominated sorting with harmony search to enhance multi-objective problem management and ensure a diverse set of solutions representing the Pareto front. Key contributions include a scenario-based approach for uncertainty management, simultaneous consideration of various DER types, and a fuzzy decision-making method for identifying optimal compromise solutions from the Pareto set. Overall, the framework demonstrates effectiveness and potential applicability in real-world scenarios, advancing multi-objective optimization techniques in the energy sector.

Nomenclature

i, j	Index for buses
k	Index of DERs technologies
m	Index of gaseous emissions
s	Index of scenarios
n	Index of substations
t	Index of times
np	Number of randomly generated price samples
nc	Number of members at cluster c
nr	Number of clusters
NB	Total number of buses
NLM	Total number of load buses
PM	The probability of each price reduction scenario
SB	Base kVA of the network
P_{ij}^{MAX}	The thermal capacity of the feeder that connects bus i to bus j
P_k^{CAP}	The capacity limit associated with the kth DER technology
Ps,ij	The power flow within the feeder that links bus i to bus j during scenario s
f1, f2	The monetary and environmental objective functions, respectively
$f_i^{\max}$, $f_i^{\min}$	The maximum and minimum values of the objective function i, respectively
$E_{k,m}^{DER}$	The emission factor for type m in the kth DER technology
E_m^G	The emission factor for type m related to electricity sourced from the grid
Ds,i	The demand present at the ith load bus during scenario s
d	The applicable discount rate
$\cos\varphi$	The power factor of the overall system
C_k^{OP}	The operational cost associated with the kth DER technology
C_k^{INV}	The investment cost linked to the kth DER technology
$P_{s,ij}^{Loss}$	The total power loss occurring in the feeder that connects bus i to bus j during scenario s
$P_{s,i,k}^{OP}$	The operational generation of the kth DER technology at bus i in scenario s
$P_{s,n}^{PP}$	The power purchased from substation n in scenario s
P_n^{SS}	The power output of the distribution substation
P_n^{SS-MAX}	The capacity limit of the distribution substation
Vs,i	The voltage level at bus i in scenario s
Zij	The impedance of the feeder that connects bus i to bus j
ρ_s	The electricity market price during scenario s
π_s	The probability associated with each scenario
μ_i^k	The membership function corresponding to the ith objective function in the kth Pareto optimal solution
μ^k	The overall membership function for the kth Pareto optimal solution

References

[1] A. Rastgou, "Distribution Network Expansion Planning: An Updated Review of Current Methods and New Challenges," *Renewable and Sustainable Energy Reviews*, vol. 189, 114062, 2024.

[2] P. Hajiamoosha, A. Rastgou, and H. Afshar, "A Multi-Objective Framework for Smart Energy Hubs: Leveraging Compressed Air Storage and Demand Response," *Journal of Green Energy Research and Innovation*, vol. 2, no. 2, pp. 1–25, 2025.

[3] B. Ahmadi, O. Ceylan, A. Ozdemir, and M. Fotuhi-Firuzabad, "A Multi-Objective Framework for Distributed Energy Resources Planning and Storage Management," *Applied Energy*, vol. 314, 118887, 2022.

[4] R. S. F. Ferraz, R. S. F. Ferraz, V. F. S. Júnior, and A. C. Rueda-Medina, "Multi-Objective Approach for Distribution System Planning Considering Stochastic Customer-Owned Distributed Energy Resources," *IEEE Access*, vol. 13, pp. 40561–40576, 2025.

[5] A. K. ALAhmad, R. Verayiah, H. Shareef, A. Ramasamy, and S. Ba-swaimi, "Enhancing Renewable Energy Integration Through Strategic Stochastic Optimization Planning of Distributed Energy Resources (Wind/PV/SBESS/MBESS) in Distribution Systems," *Energy Strategy Reviews*, vol. 59, 101683, 2025.

[6] A. Ali, A. Bughio, et al., "Optimization of Distributed Energy Resources Planning and Battery Energy Storage Management Via Large-Scale Multi-Objective Evolutionary Algorithm," *Energy*, vol. 311, 133463, 2024.

[7] K. E. Adetunji, I. W. Hofsajer, A. M. Abu-Mahfouz, and L. Cheng, "An Optimization Planning Framework for Allocating Multiple Distributed Energy Resources and Electric Vehicle Charging Stations in Distribution Networks," *Applied Energy*, vol. 322, 119513, 2022.

[8] K. Twaisan, and N. Barışçı, "Integrated Distributed Energy Resources (DER) and Microgrids: Modeling and Optimization of DERs," *Electronics*, vol. 11, no. 18, 2816, 2022.
[9] P. Hajiamoosha, A. Rastgou, S. Bahramara, and S. M. Bagher Sadati, "Stochastic Energy Management in a Renewable Energy-Based Microgrid Considering Demand Response Program," *International Journal of Electrical Power & Energy Systems*, vol. 129, 106791, 2021.
[10] A. Rastgou, J. Moshtagh, and S. Bahramara, "Improved Harmony Search Algorithm for Electrical Distribution Network Expansion Planning in the Presence of Distributed Generators," *Energy*, vol. 151, pp. 178–202, 2018.
[11] M. J. Chihota, and B. Bekker, "New Planning Principles for Distribution Networks with Penetration of Distributed Energy Resources," *2020 6th IEEE International Energy Conference (ENERGYCon)*, pp. 643–648, 2020.
[12] E. Kianmehr, S. Nikkhah, V. Vahidinasab, D. Giaouris, and P. C. Taylor, "A Resilience-Based Architecture for Joint Distributed Energy Resources Allocation and Hourly Network Reconfiguration," *IEEE Transactions on Industrial Informatics*, vol. 15, no. 10, pp. 5444–5455, 2019.
[13] Y. Wang, Y. Xu, and H. Sun, "Multi-Objective Planning of Distributed Energy Resources Based on Enhanced Adaptive Weighted-Sum Algorithm," *IEEE Transactions on Power Systems*, vol. 39, no. 2, pp. 4624–4637, 2024.
[14] Y. Wang, Y. Xu, and H. Sun, "Three-Objective Capacity Planning of Distributed Energy Resources in Distribution Network," *2024 IEEE Power & Energy Society General Meeting (PESGM)*, pp. 1–5, 2024.
[15] M. Adham, S. Keene, and R. B. Bass, "Distributed Energy Resources: A Systematic Literature Review," *Energy Reports*, vol. 13, pp. 1980–1999, 2025.
[16] A. Rastgou, J. Moshtagh, and S. Bahramara, "Probabilistic Power Distribution Planning Using Multi-Objective Harmony Search Algorithm," *Journal of Operation and Automation in Power Engineering*, vol. 6, no. 1, pp. 111–125, 2018.
[17] K. Deb, A. Pratap, S. Agarwal, and T. Meyarivan, "A Fast and Elitist Multiobjective Genetic Algorithm: NSGA-II," *IEEE Transactions on Evolutionary Computation*, vol. 6, no. 2, pp. 182–197, 2002.
[18] A. Rastgou, S. Bahramara, and J. Moshtagh, "Flexible and Robust Distribution Network Expansion Planning in the Presence of Distributed Generators," *International Transactions on Electrical Energy Systems*, vol. 28, no. 12, e2637, 2018.
[19] X. Yang, "Harmony Search as a Metaheuristic Algorithm," *Studies in Computational Intelligence*, pp. 1–14, n.d.
[20] A. Rastgou, and J. Moshtagh, "Improved Harmony Search Algorithm for Transmission Expansion Planning with Adequacy–Security Considerations in the Deregulated Power System," *International Journal of Electrical Power & Energy Systems*, vol. 60, pp. 153–164, 2014.
[21] V. Vahidinasab, "Optimal Distributed Energy Resources Planning in a Competitive Electricity Market: Multiobjective Optimization and Probabilistic Design," *Renewable Energy*, vol. 66, pp. 354–363, 2014.
[22] R. N. Allan, *Reliability Evaluation of Power Systems*, Springer Science & Business Media, 2013.
[23] Lei Wu, M. Shahidehpour, and Tao Li, "Cost of Reliability Analysis Based on Stochastic Unit Commitment," *IEEE Transactions on Power Systems*, vol. 23, no. 3, pp. 1364–1374, 2008.
[24] ZZ. Michalewicz, *Genetic Algorithms + Data Structures = Evolution Programs*, Springer Science & Business Media, 2013.
[25] M. Haghifam, H. Falaghi, and O. Malik, "Risk-Based Distributed Generation Placement," *IET Generation, Transmission & Distribution*, vol. 2, no. 2, pp. 252–260, 2008.

Declaration of competing interest

The authors declare that they have no known competing financial interests or personal relationships that could have appeared to influence the work reported in this paper. The ethical issues, including plagiarism, informed consent, misconduct, data fabrication and/or falsification, double publication and/or submission, redundancy, have been completely observed by the authors.

Bibliography

Fardad Rastgou holds a Bachelor's, Master's, and Ph.D. degree in Power Electrical Engineering. He completed his Bachelor's degree at Tabriz University and went on to earn both his Master's and Ph.D. degrees with honors from Kurdistan University in Sanandaj. Dr. Rastgou has a keen interest in power system planning, bi-level planning, and renewable resource planning. His academic journey reflects a strong commitment to advancing the field of electrical engineering, particularly in optimizing power systems for sustainability and efficiency.
Email: Fardad.rastgou@gmail.com
ORCID: 0000-0002-8620-2185
Contribution Statement: Conceptualization, Data curation, Formal analysis, Investigation, Methodology, Project administration, Resources, Software, Supervision, Validation, Visualization.

Saman Hosseini-Hemati Assistant Professor and Electrical Engineer with over 12 years of combined experience in power systems engineering, academic teaching, and research. Skilled in power system analysis, MV/HV design, and grid integration. Experienced in teaching, supervising students, and leading research in smart grids and renewable energy.
Email: saman.h@live.com
ORCID: 0000-0002-9323-2534
Contribution Statement: Software, Writing-original draft, Writing-review & editing.

Ashkan Mohammadi received the M.Sc. degree in Electrical Engineering from Azad Islamic University, Science and Research Branch, Tehran, Iran, in 2015. He obtained his Ph.D. from the University of Science and Research, Tehran. Currently, he is a faculty member at Azad Islamic University, Islamabad West Branch, Kermanshah.
Email: ashkan.mo1365@yahoo.com
ORCID: 0009-0009-9979-7032
Contribution Statement: Software, Writing-original draft, Writing-review & editing.

Journal of
Green Energy
Research and Innovation

Green Energy Generation and Sustainable Chromium Remediation in MSRC by Focusing on the Role of Microbial Bio-Supports

Marzie Razavi

Highlights

- A hybrid microbial fuel cell–electrokinetic system was developed to simultaneously remediate hexavalent chromium soil and generate bioelectricity.
- Electrodes modified with activated carbon granules significantly outperformed plain ones, increasing voltage to 641 mV and power density to 4.21 W/m^3.
- The modified system achieved 83.5% COD removal and reduced soil chromium concentrations to 68–99 μg/g.
- This approach proves to be an efficient, eco-friendly solution for simultaneous energy recovery and in-situ soil remediation.

Graphical Abstract

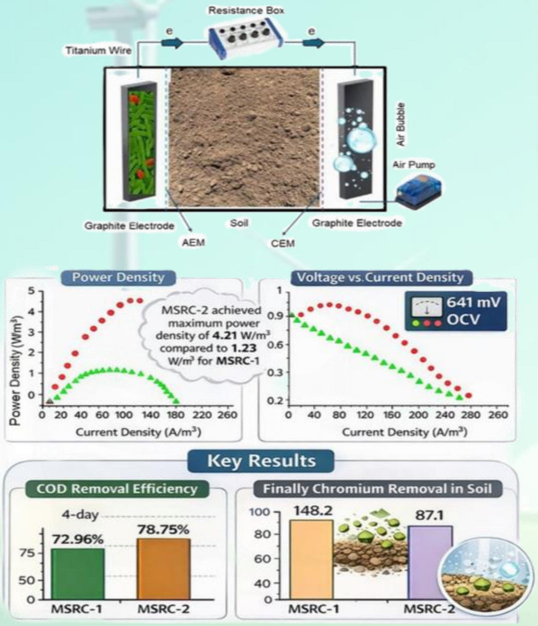

Use your device to scan and read the article online

Citation
M. Razavi, "Green Energy Generation and Sustainable Chromium Remediation in MSRC by Focusing on the Role of Microbial Bio-Supports," *Journal of Green Energy Research and Innovation*, vol. 3, no. 1, pp. 56-63, 2026.

https://doi.org/10.61882/jgeri.3.1.56

JGERI
Journal of Green Energy
Research and Innovation

Journal of Green Energy Research and Innovation 3.1 (2026) 56-63

Online ISSN: 3041-9018

Journal of Green Energy Research and Innovation

Journal Homepage: www.jgeri.araku.ac.ir

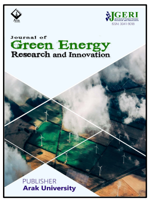

Green Energy Generation and Sustainable Chromium Remediation in MSRC by Focusing on the Role of Microbial Bio-Supports

Marzie Razavi [*]

Department of Civil Engineering, Tafresh University, 39518-79611, Tafresh, Iran.

ARTICLE INFO

Keywords:
Microbial fuel cell,
Electrokinetic remediation,
Soil remediation,
Biofilm.

Article History:
Received: 02 August 2025;
Revised: 26 August 2025;
Accepted: 23 October 2025.

Article type:
Research Article

* ***Corresponding authors***
E-mail address
m.razavi@tafreshu.ac.ir (M. Razavi)

ABSTRACT

In this study, a hybrid microbial fuel cell–electrokinetic remediation system (MSRC) was developed to remediate soil contaminated with hexavalent chromium while simultaneously generating bioelectricity. Two configurations were compared: MSRC-1 with plain graphite electrodes and MSRC-2 with graphite electrodes modified using activated carbon granules. The results demonstrated that electrode modification significantly enhanced biofilm development and electron transfer, leading to higher system efficiency. MSRC-2 achieved an open-circuit voltage of 641 mV, a maximum power density of 4.21 W/m^3, and 83.5% COD removal, compared to 406 mV, 1.23 W/m^3, and 62.3% in MSRC-1. Chromium migration toward the cathode was also more effective in MSRC-2, reducing soil concentrations to 68–99 µg/g. These findings highlight the novelty of integrating activated-carbon-modified electrodes into a microbial fuel cell–electrokinetic system, offering an efficient and environmentally friendly approach for simultaneous energy recovery and in-situ remediation of Cr (VI)-polluted soils.

1. Introduction

The discharge of wastewater containing heavy metals into receiving waters generally results in physical, chemical, and biological alterations in the environment [1,2]. The nature and extent of these changes depend largely on the type and concentration of heavy metals present in both the water and soil [3]. Due to their toxicity, these metals pose significant threats to the health of living organisms [4]. Furthermore, because these compounds cannot be degraded by microorganisms in soil, they persist for extended periods, making their removal from aquatic environments crucial [5]. The heavy metal chromium is widely distributed in soil, sediment, water, and biological materials and is considered a serious hazard to them [6-10]. The main source of chromium entering the environment is the output of metal plating processes, textile and paint industries, leather manufacturing, and its direct disposal [11,12]. Chromium exists in two forms in soil: trivalent chromium and hexavalent chromium [13]. Trivalent chromium is essential for the body in small amounts, but it has been shown that hexavalent chromium has carcinogenic effects in living organisms [14]. According to studies by Costa and Klein in 2006 and also by Owlad et al. in 2009, it has been shown that trivalent chromium can be converted to hexavalent chromium by oxidation and may accumulate in aquatic habitats through bioaccumulation processes [15,16]. Therefore, chromium removal is very critical for human health and the environment. Various soil remediation technologies have been developed to remove this contaminant based on physicochemical, thermal, and biological methods [17]. One of the physicochemical reduction techniques is the electrokinetic remediation method. Electrokinetic remediation is a well-known environmental method for removing contaminants from porous matrices with low permeability, soils, sediments, and wastes [18]. In this technique, organic materials and heavy metals are removed from the contaminated environment or transferred to another place using a weak electric field through various charge transfer mechanisms, charged particle operations, and the effects of electric potential on fluid transport within the pores of the media [19].

However, the high consumption of electrical energy is one of the limitations of the electrokinetic method in soil and sediment remediation [20]. Also, electrolytic reactions near the electrodes cause changes in the pH of the soil, such that the pH near the anode decreases sharply and increases sharply near the cathode [21]. This can cause a cemented zone near the cathode electrode and greatly slow down the migration of pollutants there [17]. For this reason, researchers have sought to provide useful methods combined with the EKR method to reduce the costs of electricity consumption in the process and, by controlling the pH, prevent cementation conditions and interruption of electroosmosis flow in the cathode zone, and simultaneously remediate contaminated soil or sediment.

Among the methods combined with EKR, solar energy and microbial fuel cells can be mentioned [20, 22-25]. In recent years, microbial fuel cells have been proposed as an emerging technology in the production of clean water [26-28] and green energy [28,29] using waste materials and have provided a new way to use renewable and low-cost energy sources [30-32]. The main obstacle in the microbial fuel cell process is the high cost of the materials used in its construction [33]. Since the shape and design of the electrodes are key factors in reducing the price of the electrode material, many efforts have been made to provide cheaper electrode materials and higher energy output [34-36]. Carbon materials are considered one of the most suitable options for electrodes in microbial fuel cells due to their high chemical resistance, low cost, and sufficient electrical conductivity [36]. It is noteworthy that the efficiency of the microbial fuel cell is increased by optimizing the formation of biofilm on the electrode, increasing the rate of organic matter decomposition, and electron transfer between the bacteria and the anode electrode. Achieving all of the above is possible by modifying the electrode surface and has become a new research field among researchers [37-39]. The first concept of a three-compartment microbial fuel cell design with an electrokinetic process for the purification of vegetable garden soil was proposed by Chen et al. in 2015, which resulted in the removal of 25% and 18% of zinc and cadmium metals, respectively [40].

Considering the challenges in the electrokinetic remediation process, including high energy consumption, severe pH changes in the vicinity of the electrodes, and reduced process efficiency due to phenomena such as the formation of a cement zone near the cathode, the need to utilize new and combined technologies to improve the efficiency and sustainability of the remediation process is increasingly felt. In the meantime, the use of microbial fuel cells as a renewable and low-cost energy source has opened a new horizon in the development of environmental cleaning technologies. These systems, with the ability to simultaneously utilize organic materials in the environment to generate electricity and remove pollutants, have paved the way for the design of more efficient combined processes. Considering the potential of microbial fuel cells in providing the energy required for the electrokinetic process, and on the other hand, the lack of comprehensive studies on the combination of these two technologies in removing heavy metals from contaminated soil, investigating and evaluating the efficiency of combined remediation systems under real conditions is considered an important research gap. According to the findings of the researchers of this study, no study has been conducted so far in the field of contaminated soil cleaning using a combined method of microbial fuel cell and electrokinetic. This study is conducted to remediate chromium-contaminated soil using an integrated Microbial–Soil–Remediation Coupled system (MSRC), as a novel hybrid approach. Also, in the present study, the performance of the combined MSRC process using three different electrodes, plate graphite, scratched plate graphite, and a combination of plate graphite and activated carbon granules as electrodes, was compared. The results of this study can be presented as a new technique for in-situ remediation of soil contaminated with heavy metals in coastal areas.

2. Materials and Methods

2.1. MSRC reactor structure

Figure 1 illustrates the schematic of the MSRC reactor, which is constructed from Plexiglas and consists of three equal-sized cubic chambers. The first chamber, known as the anode chamber, contains the wastewater; the middle chamber holds the contaminated soil sample; and the third chamber, referred to as the cathode chamber, is filled with distilled water and a phosphate buffer solution. Two ion exchange membranes (Anion exchange membrane and a cation exchange membrane) are used to separate the middle chamber from the other two chambers. In this study, two MSRC reactors with numbers 1 and 2 were used. A smooth graphite electrode was used in the anode chamber of reactor number 1. The dimensions of the anode and cathode electrodes were selected to be 3 × 3 × 0.5 cubic centimeters. The useful dimensions of the side and middle chambers were 3 × 5 × 5 cm3 and 4 × 5 × 5 cm3, respectively, in length, width, and height. A piece of titanium wire was used to connect each of the electrodes and place them in the circuit.

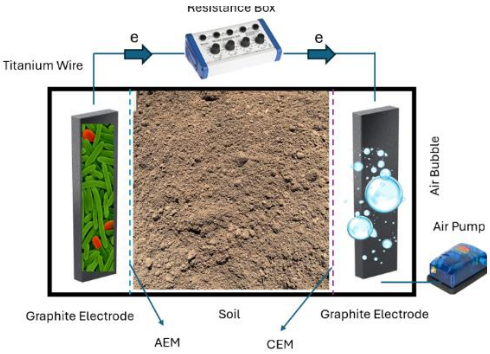

Figure 1. Schematic of MSRC in this research.

In order to start the MSRC reactor, the anode chamber was fed with a volumetric mixture of 50% anaerobic sludge obtained from the Borujerd city wastewater treatment plant as the inoculum and 50% synthetic wastewater. The specifications of the synthetic wastewater used in the system are shown in Table 1.

2.2. Soil Sampling and Characterization

The soil used in the study was obtained from the Silakhor Plain agricultural region in Lorestan Province. This plain, with an area of approximately 377 square kilometers, is located between longitude 48 ˚ 28′′ to 49 ˚30″ east and latitude 33 ˚ 15″ to 34 ˚ 10″ north, southeast of Borujerd. After visual inspection and field observations,10 topsoil samples were collected from all parts of the plain from a depth of 0-10 cm. The location and number of sampling points in the study area are shown in Figure 2.

Then, after drying in the open air, the soil samples were passed through a No.200 sieve and then subjected to physical and chemical tests. The chemical characteristics of the studied soil are presented in Table 2. An amount of 265 g of oven-dried soil was introduced into the reactor's middle chamber and compacted layer by layer in three stages to ensure uniform density. After the reactor parts were fully assembled, deionized water was introduced into the reactor through a hole in the top of the middle chamber. This operation was repeated once a week during the test period to keep the chromium-contaminated soil moist. The reactor was operated under discontinuous feeding conditions throughout the entire commissioning period. The anolyte was drained from its chamber every 4 days to maintain the appropriate level of nutrients. This process was also performed to replace the catholyte. After achieving stable electrical potential changes, the MSRC reactor operated for two more cycles. All tests were performed at room temperature. It should be noted that the average time for cleaning the chromium-contaminated soil was 78 days for each of the reactors.

3. Analysis and Calculation Methods

The pH of the solutions was measured and recorded daily using a pH meter (HI6221, HANNA, USA). The chromium concentration in the soil was measured using an inductively coupled plasma emission spectrometer (ICP-OES, Optima 5300DV, Perkin Elmer, US). The chromium reading and measurement method was performed according to standard methods [41]. The power density of the MSRC reactor presented in this study is obtained using Equation (1).

$$P = V \times I/\nu \tag{1}$$

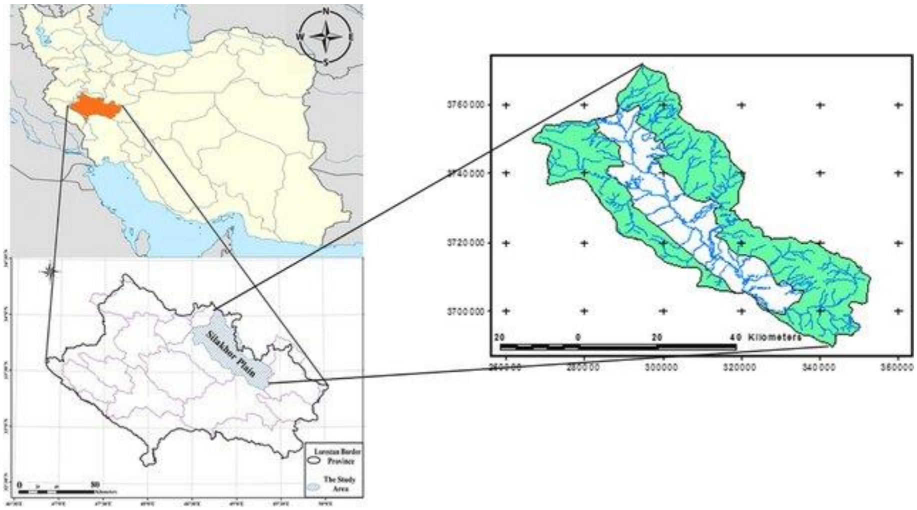

Figure 2. Silakhor plain (location and borders).

Table 1. Specifications of sewage [28].

Chemical	Amount (grams) per liter of distilled water
CH_3COONa	1.6
K_2HPO_4	1.07
KH_2PO_4	0.53
NH_4Cl	0.15
NaCl	0.5
$MgSO_4$	0.015
$CaCl_2$	0.02
Yeast extract	0.1

Table 2. Chemical characteristics of the studied samples.

	pH	CEC	EC
Unit	-	$cmol_c$/ kg	dS/m
Amount	7.6 ± 0.28	18.28 ± 4.3	0.16 ± 0.04

The resulting electric current is calculated according to Ohm's law from Equation (2):

$$I = V/R \tag{2}$$

In these relations, V is the potential difference recorded by the data logger in volts, R is the external resistance in ohms, and ν is the useful volume of the anode chamber in liters. The polarization curve was obtained based on the studies of Watson et al. to determine and calculate the internal resistance and also the maximum power density [42]. The reactor voltage was recorded every 20 minutes using a comprehensive information system with the model (AEP-DG40-WiFi, Universal, Iran). The Coulombic efficiency (CE) was calculated in Equation (3).

$$CE = \left(\sum_{i=1}^{n} I_i t_i \Big/ F b V C_R\right) \times M \times 100\% \tag{3}$$

In the equations presented, F is the Faraday constant, b is the number of moles of electrons produced per mole of substrate consumed (24 moles of electrons are produced per mole of glucose oxidized under anaerobic conditions), S is the concentration of the substrate used, and M is the molecular mass of the substrate consumed. COD was measured in triplicate and daily (every 24 hours) according to methods extracted from the standard method and using a spectrophotometer model (Hach DR 6000, USA) at a wavelength of 600 nm [43]. At the end of the experiments, the different parts of the reactor were separated from each other, and the soil sample, electrodes, and activated carbon granules (if present in the experiment) were stored in appropriate conditions for other examinations and measurements. The modified soil was stored in a refrigerator at 4 °C.

4. Results and Discussion

4.1. Power and Current Generation

In the present study, a mixture of synthetic wastewater and aerobic-anaerobic sludge from a municipal treatment plant was used as feed (substrate) in the reactors. The highest OCV values were obtained in MSRC-1 and MSRC-2 reactors, with values of 641 ± 12 mV and 406 ± 34 mV, respectively, as shown in Figure 3. When the open circuit voltage showed a stable performance, the operation of two more cycles was continued. Then, the polarization and power density curves were measured and plotted at 20-minute intervals using external resistors of 50000 to 10 Ohms (resistor box) that were closed on the circuit [42]. From these curves and the polarization gradient, the internal resistance of the reactor is obtained [44]. According to the information obtained from the polarization curve of the MSRC-1 reactor, the highest power density obtained was 4.21 W/m^3, which showed a better performance compared to the MSRC-2 reactor, with the highest power density of 1.23 W/m^3 (Figure 4). The comparison between the highest power production of the two reactors shows that the type of anode electrodes can be effective in improving the performance of the reactors. The results clearly indicate that reactor number 2, due to the presence of activated carbon granules and having a large surface area for the establishment of microorganisms and creating a suitable shelter for them, has caused the formation of a suitable biofilm on it [45]. Biological systems of adhesive growth with activated carbon granules are known as the biological activated carbon process [46]. In fact, the combination of surface adsorption and biological removal of organic matter led to the production of higher power in reactor number (2). Figures 3 and 4 show the power density and polarization curves.

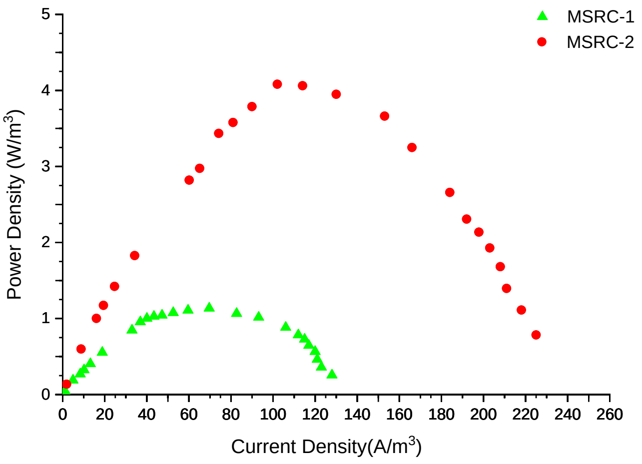

Figure 3. Power density curve of reactors.

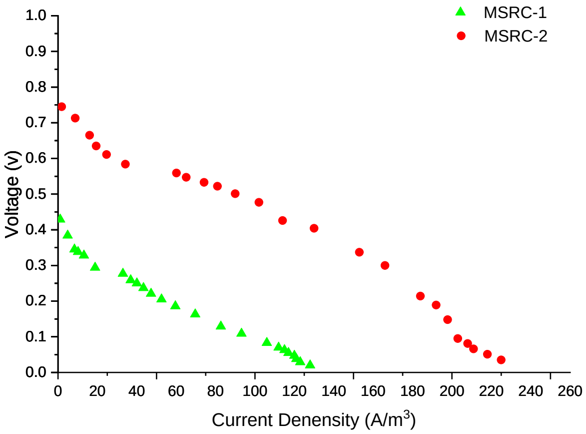

Figure 4. Polarization curve of reactors.

4.2. pH changes in soil samples

After transporting the soil sample to the laboratory and preparing it, the initial pH of the soil was measured, which was 6.8 ± 0.2. After the test period in two reactors, the pH changes in the chromium-contaminated soil were measured from the anode area to the cathode area. According to the results obtained, during the cleaning operation of the chromium-contaminated soil, the pH in the anode area was acidic and reached 6.11 ± 0.04. This is while the cathode area was basic and had a pH of 8.6 ± 0.2. According to the results of other researchers, acid is produced in the anode area and in the cathode area, and it is regenerated. Therefore, the pH at the anode decreases and increases at the cathode [47]. In general, the electrolysis process leads to alkalization and acidification of the soil, respectively, near the cathode and anode, and the production of H+ at the anode and OH- at the cathode [21]. H+ ions are transported by electroosmosis and electromigration processes, while OH- moves in the opposite direction and towards the anode. It should be noted that the mobility of H+ ions is 1.76 times higher than that of OH- ions. The migration of H+ and OH- from the anode and cathode along the contaminated soil sample as soon as an electric current is applied leads to dynamic changes in the pH of the soil [47]. In general, pH is one of the important and influential parameters in the mobility of heavy metals [48]. During the process of H+ movement in the sample, heavy metal desorption occurs, although with the presence of OH- and the formation of metal hydroxides such as Cr(OH)3 and their deposition in the sample, their mobility decreases [20,49]. During the implementation of the electrokinetic process for heavy metal removal, it is vital and essential to maintain an acidic pH throughout the soil sample and prevent the formation of metal hydroxides and the trapping of metals in the pores of the contaminated soil. Oxygen in the cathode chamber is reduced and produces water by consuming protons [50]. As a result of the consumption of protons in the oxygen reduction process, the proton transfer rate along the sample decreases and may cause the precipitation and trapping of chromium in the sample [10]. The results of this study also show that in both reactors, MSRC-1 and MSRC-2, the pH at the anode decreased and increased at the cathode. The increase in pH in both reactors is shown in Figure 5. The largest pH changes were observed in the MSRC-2 reactor. In fact, the pH changes in reactor number 2 are influenced by the electrochemical operations inside the cell and anaerobic respiration of microorganisms, the formation of more biofilm attached to the activated carbon granules and the electrode, and also the increase in the electron exchange rate between the GAC and the electrode [36,51]. In the case of reactor number 1, due to the smoothness of the graphite surface and less biofilm formation on it, resulting in reduced anaerobic respiration of bacteria, the rate of electron exchange was lower and therefore the pH changes were lower than in the previous two reactors.

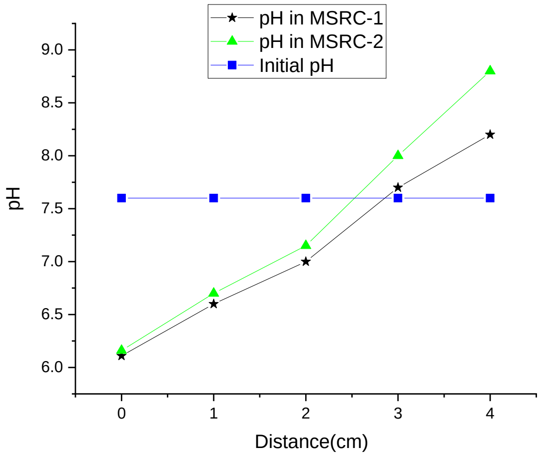

Figure 5. Relationship between pH and distance from the anode.

4.3. Chromium migration

The results of this study confirm the electrokinetic migration of chromium within the soil matrix under the electric field generated by the microbial fuel cell. As shown in Figure 6, the distribution of chromium across different sections of the soil sample after remediation by the MSRC system is compared to the initial concentration of 320 µg/g. Soil sampling was performed at 1 cm intervals along the length of the reactor. The observed trend clearly shows that chromium ions migrated from the anode region toward the cathode region, with some ultimately entering the catholyte solution. This is evident from the gradual increase in chromium concentration from the anode to the cathode side of the soil sample [10].

In this study, the soil concentration in the cathode area decreased to 132.45 µg/g and 99.1 µg/g in reactors 1 and 2, respectively. Also, the chromium concentration in the cathode region of both reactors reached 87.55 µg/g and 68 µg/g, respectively, and indicates its migration from the soil sample. Considering the presence of chromium in the catholyte (cathode chamber), it can be concluded that chromium migration from the soil sample has taken place.

4.4. COD Removal and Coulombic Efficiency in MSRC Reactor

The results of COD removal in the reactors of the present study are presented in Figure 7. Each MSRC reactor was initially operated in an open circuit mode and discontinuously, and after obtaining three suitable cycles in a closed-circuit mode. The highest COD drop in the 4-day operating time intervals was from 344.32 ± 22.35 to 763.81 ± 30.14 mg/L, respectively. The organic matter in the anolyte chamber of the reactors is consumed by the microorganisms present in it. The microorganisms form biofilms on the electrode as well as the activated carbon granules and cause the transfer of the released electrons to the electrode through the existing circuit. Activated carbon granules are mainly used for the removal of natural organic matter (NOM) and synthetic organic compounds (SOCs) [46]. A comparison of COD removal efficiencies in the two reactors shows that the low COD removal rate in the initial days of operation could be due to the growth of methanogenic bacteria that occurs in the presence of high substrate concentrations. However, the COD removal rate gradually increases as a result of the adaptation of bacteria in the system [39]. In this study, the comparison of COD removal rates clearly shows the relationship between the microbial population in the anode compartment and the COD removal rate. In fact, the increase in the anaerobic microbial population causes more electron release and consequently increases the cell voltage. The highest COD removal efficiencies were obtained in reactors 1 and 2 at 4-day HRTs of 62.28% and 83.45%, respectively. The results show that in reactor number 2, due to the presence of activated carbon granules and the provision of a more suitable substrate for creating a biofilm on it and creating ideal conditions for reducing the substrate, the COD removal efficiency was higher than in reactor 1. Also, the Coulombic efficiency obtained from the reactors is evidence of the number of electrons obtained from the substrate to produce an electric current.

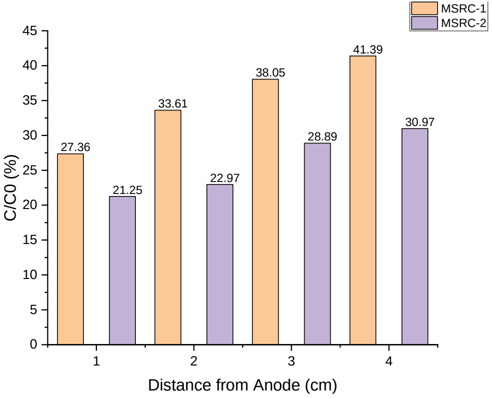

Figure 6. Chromium concentration ratio (C/C0) along the contaminated soil sample.

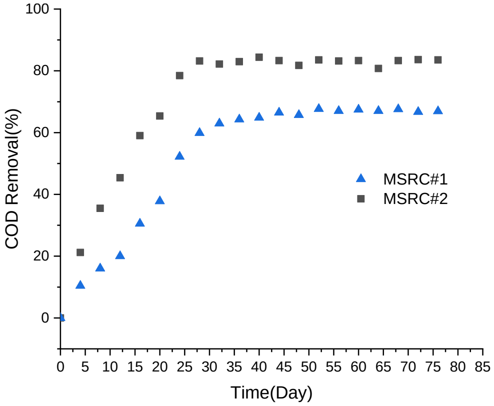

Figure 7. COD removal efficiency over time in reactors 1 and 2.

5. Conclusion

In the present study, the removal of the heavy metal chromium from contaminated soil and the impact of varying anode electrode operating conditions on the efficiency of the MSRC system were investigated. The results from reactors No. 1 and 2 indicated that pH levels decreased near the anode and increased near the cathode in both systems. The highest pH changes were observed in the MSRC-2 reactor, which was a result of electrochemical operations inside the cell and the formation of more biofilm adhering to the activated carbon granules and the electrode, as well as an increase in the electron exchange rate between GAC and the electrode. In the case of reactor No. 1, due to the smoothness of the graphite surface and the formation of less biofilm on it, the electron exchange rate was lower, and therefore the pH changes were lower than in the previous reactor. The highest OCV values were obtained in MSRC-2 and MSRC-1 reactors, with values of 641 ± 12 mV and 406 ± 34 mV, respectively. According to the information obtained from the polarization curve of the MSRC-2 reactor, the highest power density obtained was 4.21 W/m^3, which showed better performance compared to the MSRC-1 reactor, with the highest power density of 1.23 W/m^3. The comparison between the highest power production of the reactors shows that the type of anode electrodes can be effective in better performance of the reactors. Also, the research findings showed that the highest COD removal efficiency in 4-day HRTs was 78.75% and 72.96%, respectively, which indicates a more favorable performance of reactor number 2 compared to reactor number 1. Previous studies did not report COD removal efficiency under comparable MSRC operating conditions, highlighting the novelty of the present work. The use of activated carbon granules, due to the creation of a suitable substrate for bacteria to settle and anaerobic respiration, as well as electron transfer, can be a very good option for increasing the efficiency of microbial fuel cell systems. The results also showed that the use of a combined microbial fuel cell and electrokinetic process method can be considered as an environmentally friendly method due to the favorable results in cleaning chromium-contaminated soil.

References

[1] O. B. Akpor, "Heavy Metal Pollutants in Wastewater Effluents: Sources, Effects and Remediation," *Advances in Bioscience and Bioengineering*, vol. 2, no. 4, 37, 2014.

[2] P. K. Singh, U. Kumar, et al., "Critical Review on Toxic Contaminants in Surface Water Ecosystem: Sources, Monitoring, and Its Impact on Human Health," *Environmental Science and Pollution Research*, vol. 31, no. 45, pp. 56428–56462, 2024.

[3] P. Saravanan, V. Saravanan, et al., "Comprehensive Review on Toxic Heavy Metals in the Aquatic System: Sources, Identification, Treatment Strategies, and Health Risk Assessment," *Environmental Research*, vol. 258, 119440, 2024.

[4] S. Kamran, A. Shafaqat, et al., "Heavy Metals Contamination and What Are the Impacts on Living Organisms," *Greener Journal of Environmental Management and Public Safety*, vol. 2, no. 4, pp. 172–179, 2013.

[5] N. Abdu, A. A. Abdullahi, and A. Abdulkadir, "Heavy Metals and Soil Microbes," *Environmental Chemistry Letters*, vol. 15, no. 1, pp. 65–84, 2016.

[6] Anonymous, "The Trace Element Content of Soils," *Agronomy Journal*, vol. 48, no. 3, pp. 144–144, 1956.

[7] M. Z. H. Khan, M. R. Hasan, M. Khan, S. Aktar, and K. Fatema, "Distribution of Heavy Metals in Surface Sediments of the Bay of Bengal Coast," *Journal of Toxicology*, vol. 2017, pp. 1–7, 2017.

[8] L. Ghosh, S. Adhikari, and S. Ayyappan, "Distribution of Lead, Cadmium and Chromium in Sediment and Their Availability to Various Organs of a Freshwater Teleost, Labeo Rohita (Hamilton)," *Journal of Fisheries and Aquatic Science*, vol. 1, no. 2, pp. 200–208, 2006.

[9] P. Muniz, N. Venturini, and M. Gómez-Erache, "Spatial Distribution of Chromium and Lead in the Benthic Environment of Coastal Areas of the Río De La Plata Estuary (Montevideo, Uruguai)," *Brazilian Journal of Biology*, vol. 64, no. 1, pp. 103–116, 2004.

[10] N. Habibul, Y. Hu, and G. Sheng, "Microbial Fuel Cell Driving Electrokinetic Remediation of Toxic Metal Contaminated Soils," *Journal of Hazardous Materials*, vol. 318, pp. 9–14, 2016.

[11] R. Saha, R. Nandi, and B. Saha, "Sources and Toxicity of Hexavalent Chromium," *Journal of Coordination Chemistry*, vol. 64, no. 10, pp. 1782–1806, 2011.

[12] S. Dhanakumar, and R. Mohanraj, "Chromium Fractionation in the River Sediments and Its Implications on the Coastal Environment: A Case Study in the Cauvery Delta, Southeast Coast of India," *Coastal Zone Management*, pp. 347–360, 2019.

[13] N. Shariatmadari, C. Weng, and H. Daryaee, "Enhancement of Hexavalent Chromium [Cr(VI)] Remediation from Clayey Soils by Electrokinetics Coupled with a Nano-Sized Zero-Valent Iron Barrier," *Environmental Engineering Science*, vol. 26, no. 6, pp. 1071–1079, 2009.

[14] T. Norseth, "The Carcinogenicity of Chromium," *Environmental Health Perspectives*, vol. 40, 121, 1981.

[15] M. Costa, and C. B. Klein, "Toxicity and Carcinogenicity of Chromium Compounds in Humans," *Critical Reviews in Toxicology*, vol. 36, no. 2, pp. 155–163, 2006.

[16] M. Owlad, M. K. Aroua, W. A. W. Daud, and S. Baroutian, "Removal of Hexavalent Chromium-Contaminated Water and Wastewater: A Review," *Water, Air, and Soil Pollution*, vol. 200, no. 1-4, pp. 59–77, 2008.

[17] H. D. Sharma and K. R. Reddy, *Geoenvironmental Engineering: Site Remediation, Waste Containment, and Emerging Waste Management Technologies*, John Wiley & Sons, 2004.

[18] F. Rozas, and M. Castellote, "Electrokinetic Remediation of Dredged Sediments Polluted with Heavy Metals with Different Enhancing Electrolytes," *Electrochimica Acta*, vol. 86, pp. 102–109, 2012.

[19] Y. B. Acar, R. J. Gale, et al., "Electrokinetic Remediation: Basics and Technology Status," *Journal of Hazardous Materials*, vol. 40, no. 2, pp. 117–137, 1995.

[20] S. Yuan, Z. Zheng, J. Chen, and X. Lu, "Use of Solar Cell in Electrokinetic Remediation of Cadmium-Contaminated Soil," *Journal of Hazardous Materials*, vol. 162, no. 2-3, pp. 1583–1587, 2009.

[21] K. Kim, J. Cho, K. Baek, J. Yang, and S. Ko, "Electrokinetic Removal of Chloride and Sodium from Tidelands," *Journal of Applied Electrochemistry*, vol. 40, no. 6, pp. 1139–1144, 2010.

[22] E. Jeon, S. Ryu, and K. Baek, "Application of Solar-Cells in the Electrokinetic Remediation of As-Contaminated Soil," *Electrochimica Acta*, vol. 181, pp. 160–166, 2015.

[23] P. S. C. Rao, J. W. Jawitz, C. G. Enfield, R. Falta Jr., M. D. Annable, and A. L. Wood, "Technology Integration for Contaminated Site Remediation: Clean-Up Goals and Performance Criteria," in *Groundwater Quality: Natural and Enhanced Restoration of Groundwater Pollution*, 2001, pp. 571–578.

[24] S. Pamukcu, A. Weeks, and J. K. Wittle, "Enhanced Reduction of Cr(VI) by Direct Electric Current in a Contaminated Clay," *Environmental Science & Technology*, vol. 38, no. 4, pp. 1236–1241, 2004.

[25] P. Thepsithar, and E. P. L. Roberts, "Removal of Phenol from Contaminated Kaolin Using Electrokinetically Enhanced in Situ Chemical Oxidation," *Environmental Science & Technology*, vol. 40, no. 19, pp. 6098–6103, 2006.

[26] A. Ebrahimi, D. Yousefi Kebria, and G. D. Najafpour, "Co-Treatment of Septage and Municipal Wastewater in a Quadripartite Microbial Desalination Cell," *Chemical Engineering Journal*, vol. 354, pp. 1092–1099, 2018.

[27] T. C. Pannell, R. K. Goud, D. J. Schell, and A. P. Borole, "Effect of Fed-Batch Vs. Continuous Mode of Operation on Microbial Fuel Cell Performance Treating Biorefinery Wastewater," *Biochemical Engineering Journal*, vol. 116, pp. 85–94, 2016.

[28] A. Ebrahimi, G. D. Najafpour, and D. Yousefi Kebria, "Performance of Microbial Desalination Cell for Salt Removal and Energy Generation Using Different Catholyte Solutions," *Desalination*, vol. 432, pp. 1–9, 2018.

[29] A. Ebrahimi, D. Yousefi Kebria, and G. N. Darzi, "Improving Bioelectricity Generation and COD Removal of Sewage Sludge in Microbial Desalination Cell," *Environmental Technology*, vol. 39, no. 9, pp. 1188–1197, 2017.

[30] I. Gajda, J. Greenman, C. Melhuish, and I. A. Ieropoulos, "Electricity and Disinfectant Production from Wastewater: Microbial Fuel Cell as a Self-Powered Electrolyser," *Scientific Reports*, vol. 6, no. 1, 2016.

[31] D. Pant, A. Singh, et al., "Bioelectrochemical Systems (BES) for Sustainable Energy Production and Product Recovery from Organic Wastes and Industrial Wastewaters,"

RSC Adv., vol. 2, no. 4, pp. 1248–1263, 2012.
[32] M. A. Massoud, A. Tarhini, and J. A. Nasr, "Decentralized Approaches to Wastewater Treatment and Management: Applicability in Developing Countries," *Journal of Environmental Management*, vol. 90, no. 1, pp. 652–659, 2009.
[33] L. Zhuang, Y. Yuan, Y. Wang, and S. Zhou, "Long-Term Evaluation of a 10-Liter Serpentine-Type Microbial Fuel Cell Stack Treating Brewery Wastewater," *Bioresource Technology*, vol. 123, pp. 406–412, 2012.
[34] X. Chen, P. Liang, Z. Wei, X. Zhang, and X. Huang, "Sustainable Water Desalination and Electricity Generation in a Separator Coupled Stacked Microbial Desalination Cell with Buffer Free Electrolyte Circulation," *Bioresource Technology*, vol. 119, pp. 88–93, 2012.
[35] Z. Wang, U. Wille, and E. Juaristi, *Encyclopedia of Physical Organic Chemistry, 6 Volume Set*, John Wiley & Sons, 2017.
[36] J. Wei, P. Liang, and X. Huang, "Recent Progress in Electrodes for Microbial Fuel Cells," *Bioresource Technology*, vol. 102, no. 20, pp. 9335–9344, 2011.
[37] M. Zhou, M. Chi, J. Luo, H. He, and T. Jin, "An Overview of Electrode Materials in Microbial Fuel Cells," *Journal of Power Sources*, vol. 196, no. 10, pp. 4427–4435, 2011.
[38] H. Liu, S. Cheng, and B. E. Logan, "Power Generation in Fed-Batch Microbial Fuel Cells as a Function of Ionic Strength, Temperature, and Reactor Configuration," *Environmental Science & Technology*, vol. 39, no. 14, pp. 5488–5493, 2005.
[39] A. Ebrahimi, D. Yousefi Kebria, and G. Najafpour Darzi, "Enhancing Biodegradation and Energy Generation Via Roughened Surface Graphite Electrode in Microbial Desalination Cell," *Water Science and Technology*, vol. 76, no. 5, pp. 1206–1214, 2017.
[40] Z. Chen, B. Zhu, W. Jia, J. Liang, and G. Sun, "Can Electrokinetic Removal of Metals from Contaminated Paddy Soils Be Powered by Microbial Fuel Cells?," *Environmental Technology & Innovation*, vol. 3, pp. 63–67, 2015.
[41] J. R. Dean, *Methods for Environmental Trace Analysis*, John Wiley & Sons, 2003.
[42] V. J. Watson, and B. E. Logan, "Analysis of Polarization Methods for Elimination of Power Overshoot in Microbial Fuel Cells," *Electrochemistry Communications*, vol. 13, no. 1, pp. 54–56, 2011.
[43] American Public Health Association (APHA), *Standard Methods for the Examination of Water and Wastewater*, 21st ed., Washington, DC, USA, 2005.
[44] B. E. Logan, *Microbial Fuel Cells*, John Wiley & Sons, 2008.
[45] W. Weber, Jr., M. Pirbazari, and G. Melson, "Biological Growth on Activated Carbon: An Investigation by Scanning Electron Microscopy," *Environmental Science & Technology*, vol. 12, no. 7, pp. 817–819, 1978.
[46] F. Çeçen and Ö. Aktas, *Activated Carbon for Water and Wastewater Treatment: Integration of Adsorption and Biological Treatment*, John Wiley & Sons, 2011.
[47] Y. B. Acar, and A. N. Alshawabkeh, "Principles of Electrokinetic Remediation," *Environmental Science & Technology*, vol. 27, no. 13, pp. 2638–2647, 1993.
[48] J. Peng, Y. Song, P. Yuan, X. Cui, and G. Qiu, "The Remediation of Heavy Metals Contaminated Sediment," *Journal of Hazardous Materials*, vol. 161, no. 2-3, pp. 633–640, 2009.
[49] R. Iannelli, M. Masi, et al., "Electrokinetic Remediation of Metal-Polluted Marine Sediments: Experimental Investigation for Plant Design," *Electrochimica Acta*, vol. 181, pp. 146–159, 2015.
[50] C. J. Sund, S. McMasters, S. R. Crittenden, L. E. Harrell, and J. J. Sumner, "Effect of Electron Mediators on Current Generation and Fermentation in a Microbial Fuel Cell," *Applied Microbiology and Biotechnology*, vol. 76, no. 3, pp. 561–568, 2007.
[51] B. Erable, D. Féron, and A. Bergel, "Microbial Catalysis of the Oxygen Reduction Reaction for Microbial Fuel Cells: A Review," *ChemSusChem*, vol. 5, no. 6, pp. 975–987, 2012.

Declaration of competing interest

The author declare that she has no known competing financial interests or personal relationships that could have appeared to influence the work reported in this paper. The ethical issues, including plagiarism, informed consent, misconduct, data fabrication and/or falsification, double publication and/or submission, redundancy, have been completely observed by the author.

Bibliography

Marzie Razavi obtained her M.Sc. degree in Environmental Engineering from Iran University of Science and Technology (IUST), Tehran, Iran in 2012 and her Ph.D. degree in Environmental Engineering from Babol Noshirvani University of Technology, Babol, Iran in 2020. She is currently a member of the Faculty of Civil Engineering at Tafresh University. Her research interests include Water and Wastewater treatment, Electrokinetic Soil Remediation, Electrocoagulation and Energy production by Microbial Fuel Cell.

Email: m.razavi@tafreshu.ac.ir

ORCID: 0000-0003-4229-3502

Contribution Statement: Conceptualization, Investigation, Methodology, Resources, Roles/Writing - original draft, Writing-review & editing.

Journal of
Green Energy
Research and Innovation

Maximum Power Point Tracking of Solar Arrays under Partial Shading Conditions Using a New Quadratic-Spline Method

Behrooz Shaban , Abdolhossein Saleh

Highlights

- **A novel quadratic spline-based MPPT (QS-MPPT) technique accurately tracks the global maximum power point under partial shading.**
- **The method uses simple interpolation to achieve rapid, oscillation-free convergence, outperforming standard algorithms like P&O and PSO.**
- **Its low complexity enables easy implementation on cost-effective microcontrollers for real-world applications.**
- **Simulations confirm superior accuracy and speed in complex multi-peak shading scenarios compared to existing methods.**

Graphical Abstract

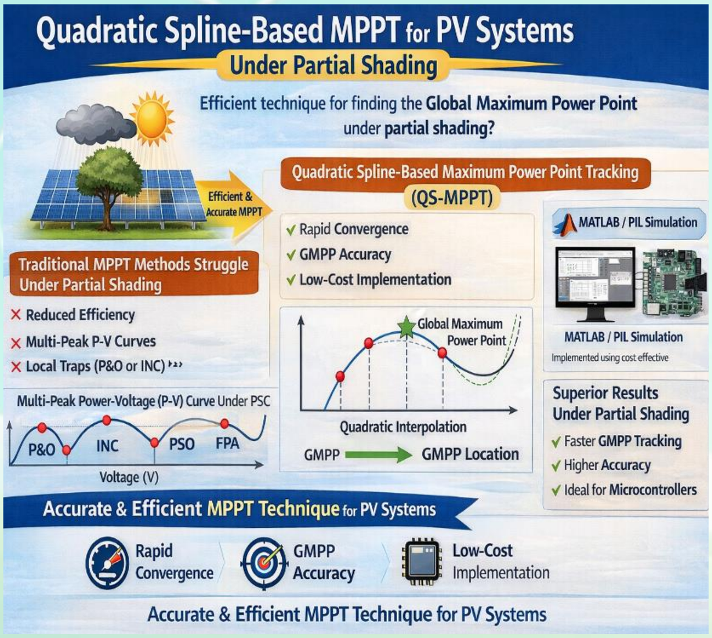

Citation
B. Shaban, and A. Saleh, "Maximum Power Point Tracking of Solar Arrays under Partial Shading Condition Using a New Quadratic-Spline Method," *Journal of Green Energy Research and Innovation*, vol. 3, no. 1, pp. 64-76, 2026.

https://doi.org/10.61882/jgeri.3.1.64

JGERI
Journal of Green Energy Research and Innovation

Journal of Green Energy Research and Innovation 3.1 (2026) 64-76

Online ISSN: 3041-9018

Journal of Green Energy Research and Innovation

Journal Homepage: www.jgeri.araku.ac.ir

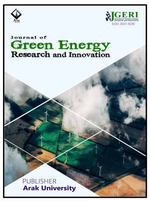

Maximum Power Point Tracking of Solar Arrays under Partial Shading Conditions Using a New Quadratic-Spline Method

Behrooz Shaban, Abdolhossein Saleh*

Department of Electrical Engineering, Faculty of Engineering, Malayer University, Malayer, Iran.

ARTICLE INFO

Keywords:
Photovoltaic Array,
Maximum Power Point Tracking,
Partial Shading Conditions,
Multi-Peak P-V Characteristics,
Quadratic Spline.

Article History:
Received: 01 September 2025;
Revised: 07 October 2025;
Accepted: 25 October 2025.

Article type:
Research Article

* ***Corresponding author***
E-mail address
hosein.saleh@malayeru.ac.ir (A.Saleh)

ABSTRACT

Photovoltaic (PV) systems have become indispensable in the renewable energy landscape, harnessing the sun's abundant and clean potential. However, their efficiency is often compromised by low conversion rates, particularly under partial shading conditions (PSC). This study introduces a novel quadratic spline-based maximum power point tracking (QS-MPPT) technique to optimize PV array performance under both uniform irradiance and PSC. Unlike conventional methods such as Perturb and Observe (P&O) or Incremental Conductance (INC), which struggle to pinpoint the global maximum power point (GMPP) amid the multi-peak power-voltage (P-V) curves typical of PSC, QS-MPPT employs a straightforward quadratic interpolation approach. By leveraging a minimal set of sampled points, this method rapidly and accurately locates the GMPP, ensuring stability without oscillations around the operating point. Simplicity of the proposed method also makes it ideal for implementation on cost-effective microcontrollers, broadening its practical appeal for real-world PV applications. The efficiency of the proposed method is shown by the time domain simulation in the MATLAB/SIMULINK environment and implementation in the form of a processor-in-the-loop (PIL). Through MATLAB simulations, QS-MPPT performance is evaluated and compared with MPPT techniques like P&O, Particle Swarm Optimization (PSO), and Flower Pollination Algorithm (FPA) in three- and four-peak PSC scenarios, where the proposed method shows higher accuracy and faster convergence.

1. Introduction

The urgent global shift toward renewable energy has positioned photovoltaic (PV) systems as a cornerstone of sustainable power generation, capitalizing on their clean, abundant, and inexhaustible nature [1]. Solar energy offers a promising alternative to fossil fuels, reducing greenhouse gas emissions and dependency on finite resources, yet its widespread adoption is hindered by inherent limitations in energy conversion efficiency [2]. One of the most significant challenges arises under partial shading conditions (PSC), where non-uniform irradiance caused by obstacles such as buildings, trees, or clouds disrupts the uniform performance of PV arrays [3]. This disruption leads to a complex power-voltage (P-V) characteristic, marked by multiple peaks, which complicates the identification and tracking of the global maximum power point (GMPP), which is critical for optimal energy harvest [4].
Traditional maximum power point tracking (MPPT) techniques, such as Perturb and Observe (P&O) and Hill Climbing (HC), and improved methods [5,6] have been widely employed due to their simplicity and effectiveness under uniform sunlight [7]. However, these methods falter in PSC scenarios and frequently converge to local maximum power points (LMPPs) rather than the GMPP, resulting in substantial energy losses [8]. The inability of these conventional approaches to adapt to varying environmental conditions has spurred extensive research into more robust solutions [9]. Among these, advanced meta-heuristic algorithms like Particle Swarm Optimization (PSO) have gained attention for their ability to navigate multi-peak P-V characteristics by simulating swarm behavior to locate the GMPP [10]. Similarly, the Flower Pollination Algorithm (FPA) draws inspiration from natural processes to enhance tracking accuracy under challenging conditions [11], while the Artificial Bee Colony (ABC) method mimics foraging patterns to achieve comparable results [12].

- These techniques have demonstrated impressive performance, often achieving high precision and rapid convergence even in dynamic shading scenarios [13]. Despite their strengths, meta-heuristic methods come with notable drawbacks, including high computational complexity and resource demands, which inflate implementation costs and limit their practicality for widespread use, particularly in cost-sensitive applications [14]. This complexity often necessitates sophisticated hardware, posing a barrier to scalability in real-world PV installations [15]. Alternative approaches, such as Incremental Conductance (INC), aim to overcome some of these issues by relying on dynamic adjustments to track the MPP, yet they too struggle to identify the GMPP consistently under PSC [16,17]. Other strategies, like Golden Section Search (GSS), offer a structured search mechanism but lack the flexibility required for rapidly changing shading patterns [18]. Fuzzy logic-based methods have also been explored, leveraging rule-based systems to improve adaptability, though their effectiveness depends heavily on precise tuning, adding another layer of complexity [19]. In [20-22], new MPPT techniques based on the cubic spline method are presented, which are fast and accurate in tracking GMPP. These methods impose a large computational burden on the processor because they require inverting a matrix with a large number of elements to calculate the coefficients of the polynomials for each section of the P-V curve. This computational burden will be much higher when fitting multiple peaks in a multi-peak P-V characteristic in specific applications that require extracting the equivalent polynomial for all peaks. In response to these challenges, this paper introduces a novel quadratic spline-based MPPT (QS-MPPT) technique designed to balance between simplicity, accuracy, and efficiency. By employing a quadratic spline interpolation approach and establishing simplified equations, this method constructs a piecewise representation of the P-V curve using a minimal set of sampled points and provides accurate GMPP tracking without the computational overhead of meta-heuristic algorithms and the cubic-spline method. It does not involve over-fitting and the matrix inversions of higher-order splines, which are prone to ill-conditioning. The proposed technique is rigorously validated through MATLAB simulations, and its performance is compared with established methods such as FPA, PSO, and P&O, and its practical feasibility is demonstrated through processor-in-the-loop (PIL) testing using an STM32 microcontroller. Thus, the main highlights of the paper are:
- **Novel QS-MPPT algorithm:** The core contribution is a new MPPT method that uses quadratic spline interpolation to model the complex, multi-peak P-V curve that occurs under partial shading. It rapidly estimates the GMPP using a minimal set of voltage and current samples.
- **Computational efficiency and simplicity:** Unlike meta-heuristic algorithms (PSO, FPA) or cubic spline methods, the proposed quadratic approach uses simpler mathematical equations, avoiding matrix inversions and complex calculations. This makes it suitable for low-cost microcontrollers. It does not involve over-fitting and the matrix inversions of higher-order splines, which are prone to ill-conditioning.
- **Fast and accurate convergence:** Through simulations, the paper demonstrates that the QS-MPPT method converges to the GMPP faster and often more accurately than the compared methods (FPA, PSO, P&O), particularly in challenging scenarios with three and four peaks in the P-V curve.
- **Practical validation via PIL implementation:** By validating the algorithm's feasibility through PIL testing on an STM32 microcontroller, it is proven that the algorithm can be run in real-time on affordable and available hardware.

The rest of the article is divided as follows. Section 2 describes the structure of the power circuit and the PIL implementation method. Section 3 presents the concepts of quadratic spline curve fitting and the proposed MPPT method. In Section 4, time-domain simulation studies and PIL testing results are presented, and finally, in Section 5, the conclusions are drawn.

2. Power Circuit and PIL Implementation Description

The power circuit used to obtain maximum power consists of a conventional boost converter with a series array of solar panels connected to its input terminal and a resistive load at its output. The PV system design strategy varies depending on the converter and different types of loads; different criteria for resistance loads and fixed voltage loads must be considered. The structure of this circuit is shown in Figure 1.

With respect to the voltage and current gain of the boost converter, which are given in Equations (1) and (2) respectively, the relationship between the equivalent resistance observed from the load resistance R_{out} at the input of the converter R_{in} is expressed by Equation (3).

$$\frac{V_{out}}{V_{in}} = \frac{1}{1-D} \tag{1}$$

$$\frac{I_{out}}{I_{in}} = 1-D \tag{2}$$

$$R_{in} = R_{out}(1-D)^2\,; 0 < D < 1 \tag{3}$$

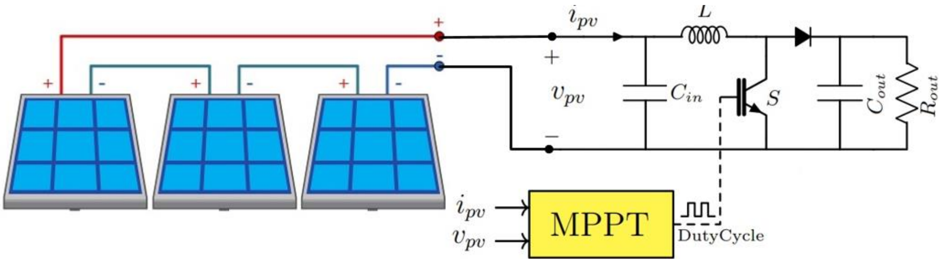

Figure 1. Power circuit for MPPT.

where V_{out}/I_{out} and V_{in}/I_{in} are respectively the output voltage/current and input voltage/current of the converter, and D is the duty cycle. Based on Equation (3), one can deduce Equation (4):

$$R_{in} \leq R_{out} \tag{4}$$

Therefore, to extract maximum power from the solar panels connected to the input of the boost converter, the load resistance must be chosen large enough so that it is greater than the equivalent resistance of the solar panel when operating at MPP. Figure 2 shows the region of the I-V characteristic of a solar panel that a boost converter can sweep at its input.

3. Concepts of Quadratic Spline Curve Fitting and Proposed MPPT Method

In this section, the concepts of curve fitting using a quadratic spline are first explained. In the following, the proposed MPPT method, derived from this curve fitting method, which can track the maximum power point in partial shading conditions in series solar panels and a multi-peaked P-V characteristic, is presented.

3.1. *Basic Concepts of Quadratic Spline Curve Fitting*

To better understand the quadratic spline curve fitting method, an explanation of the concepts of this method is provided on a hypothetical P-V characteristic shown in Figure 3. Quadratic spline interpolation defines a quadratic polynomial between two specific points; then, for the *n* sample points, n-1 quadratic functions are continuous and have first and second derivatives over the entire domain. For example, in Figure 3, a typical quadratic spline function connects the 5 sample points $((V_1, P_1), (V_2, P_2), (V_3, P_3), (V_4, P_4), (V_5, P_5))$ (Equations (5) and (6)), where:

$$P(v) = \begin{cases} C_1(v) & v_1 \leq v < v_2 \\ C_2(v) & v_2 \leq x < v_3 \\ C_3(v) & v_3 \leq x < v_4 \\ C_4(v) & v_4 \leq x < v_5 \end{cases} \tag{5}$$

where

$$C_i(v) = \gamma_i(v - v_i)^2 + \beta_i(v - v_i) + \alpha_i \quad ; \quad i = 1,2,3,4 \tag{6}$$

According to Figure 3, for every sample v_i, the calculated spline function should yield P_i . Then, we have Equation (7):

$$C_i(v_i) = P_i \quad ; \quad i = 1,2,3,4 \tag{7}$$

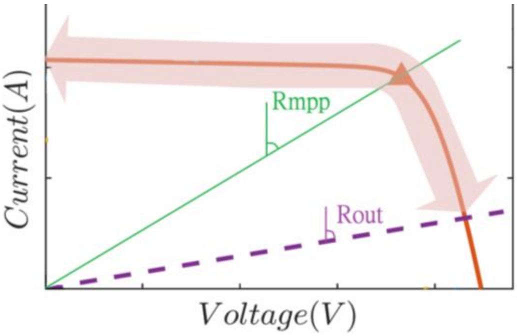

Figure 2. I-V characteristic of a solar panel and the region of the boost converter sweeping.

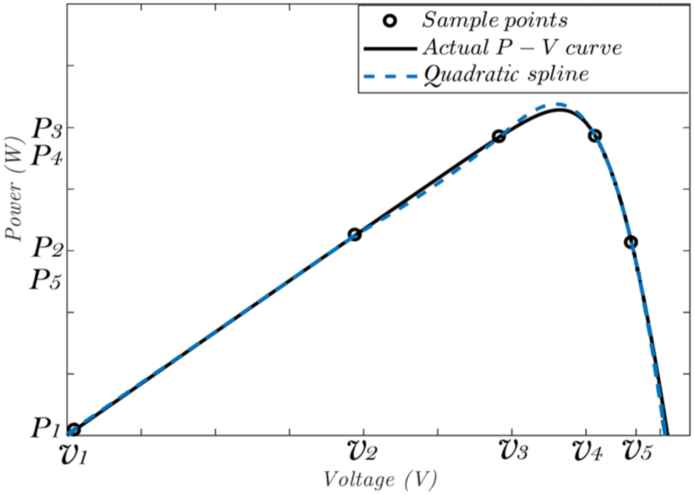

Figure 3. Hypothetical P-V characteristic and fitted quadratic spline with 5 sample points [20].

Equations (6) and (7) indicate that:

$$P(v_i) = C_i(v_i) = P_i = \alpha_i \quad ; \; i = 1,2,3,4 \tag{8}$$

On the whole interval $[v_1, v_5]$, $P(v)$ is continuous, so as shown in Figure 3, we have Equation (9):

$$C_i(v_{i+1}) = P_{i+1} = \gamma_i(v_{i+1} - v_i)^2 + \beta_i(v_{i+1} - v_i) + \alpha_i \quad ; \; i = 1,2,3,4 \tag{9}$$

By substituting $h_i = v_{i+1} - v_i$, Equation (10) is given:

$$\alpha_i + \beta_i h_i + \gamma_i h_i^2 = P_{i+1} \quad ; \; i = 1,2,3,4 \tag{10}$$

Since $P(v)$ has a continuous first derivative on the interval. Therefore, the continuity of the first derivation gives:

$$C_i'(v_{i+1}) = C_{i+1}'(v_{i+1}) \rightarrow \beta_{i+1} + 2\gamma_i h_i = \beta_{i+1}$$

$$\gamma_i = \frac{\beta_{i+1} - \beta_i}{2h_i} \quad ; \; i = 1,2,3,4 \tag{11}$$

By some manipulation in above equations, we have

$$\alpha_i + \beta_i h_i + \left(\frac{\beta_{i+1} - \beta_i}{2h_i}\right) h_i^2 = P_{i+1} \rightarrow \alpha_i + \beta_i h_i + (\frac{\beta_{i+1} - \beta_i}{2}) h_i = P_{i+1} \rightarrow 2\beta_i h_i + \beta_{i+1} h_i - \beta_i h_i = 2(P_{i+1} - P_i)$$

Thus, Equation (12) gives

$$\beta_i h_i + \beta_{i+1} h_i = 2(P_{i+1} - P_i) \; ; \; i = 1,2,3,4 \tag{12}$$

For simplicity, the curve $C_1(v)$ is fitted to a line in the interval $[v_1, v_2]$. This approximation is a proper approximation given that $C_1(v)$ lies in the linear region to the left of the peak of the P-V curve. So, we have Equation (13):

$$\gamma_1 = 0 \tag{13}$$

By substituting Equation (13) into Equation (11), we have Equation (14):

$$\beta_1 = \beta_2 \tag{14}$$

Now all other unknown coefficients in the quadratic spline functions in the interval $[v_1, v_5]$ are obtained from Equations (15)-(18):

$$\beta_1 h_1 + \beta_2 h_1 = 2(P_2 - P_1) \tag{15}$$

$$\beta_2 h_2 + \beta_3 h_2 = 2(P_3 - P_2) \tag{16}$$

$$\beta_3 h_3 + \beta_4 h_3 = 2(P_4 - P_3) \tag{17}$$

$$\beta_4 h_4 + \beta_5 h_4 = 2(P_5 - P_4) \tag{18}$$

From Equations (12) and (13):

$$\beta_1 h_1 + \beta_1 h_1 = 2(P_2 - P_1) \rightarrow \beta_1 = \beta_2 = \frac{P_2 - P_1}{h_1} \tag{19}$$

According to Equations (16)-(18), respectively, Equations (20)-(22) are deduced:

$$\beta_3 = \frac{2(P_3 - P_2)}{h_2} - \beta_2 \tag{20}$$

$$\beta_4 = \frac{2(P_4 - P_3)}{h_3} - \beta_3 \tag{21}$$

$$\beta_5 = \frac{2(P_5 - P_4)}{h_4} - \beta_4 \tag{22}$$

According to the above equations, it can be seen that the alpha values are the same as the power, and by obtaining the beta coefficients from Equations (19)-(22), the gamma coefficients can also be calculated from Equation (11). Now, by having the coefficients of the quadratic equations, namely alpha, beta, and gamma, the equations between each interval $[v_i, v_{i+1}]$, which are all quadratic, can be easily obtained with a suitable approximation. It is clear that with 5 sample points, four quadratic equations with specific coefficients will be extracted, from which the maximum value of each equation can be found.

3.2. *MPPT Method Based on Quadratic-Spline under Partial Shading Conditions*

In this section, first, the method of tracking the maximum power point using the quadratic spline-based MPPT method in atmospheric conditions with uniform radiation is explained, and then it is extended to the maximum power tracking algorithm in partial shading conditions.

A) MPPT under Uniform Irradiation

Suppose the P-V characteristic be same as that shown in Figure 3. In this case, the DC converter transfers the power generated by a single module (or a series of modules that have the same irradiations and environmental conditions) to the load. In this algorithm, only the voltage and current of the PV module are used, and no other quantities are used, which is a simple and less expensive structure. Several duty cycles (for example, 5 duty cycles) are applied to the switch by the QS-MPPT, and module current and voltage are measured to obtain the required samples and calculate their power. After collecting the required samples, the P-V curve function is approximated using the quadratic spline interpolation method to find V_{mpp} and $P_{mpp,}$ and using Equation (23), D is calculated.

$$D = 1 - \frac{V_{mpp}}{\sqrt{R_{out} * P_{mpp}}} \tag{23}$$

To further refine the outcome, an additional step involves correcting the *D* using a P&O algorithm with a small voltage perturbation (Δv). This crucial correction process not only enhances the accuracy of the *D* but also effectively mitigates the adverse effects of system non-idealities, such as parasitic resistance and forward voltage drop across diodes [20]. The algorithm operates by first identifying the optimal *D* and then maintaining it as long as atmospheric conditions remain stable. Should atmospheric changes disrupt the system's operating point, the PV output power will fluctuate. Consequently, the algorithm will reactivate to pinpoint a new MPP.

B) MPPT under Partial Shading Conditions

When partial shading occurs, the solar irradiation received by individual modules differs significantly. The module exposed to the most intense sunlight generates the highest current. This strong current subsequently compels modules receiving less irradiation to operate in a reverse bias state. Operating in the reverse bias region not only leads to substantial power losses but also has a detrimental impact on the PV module. Therefore, to reduce the harmful consequences of partial shading, bypass diodes are installed (Figure 4) to limit the reverse voltage across the PV modules [23].

Figure 5 illustrates an example of the characteristic curve for this PV module string under partial shading conditions, where PV_1 and PV_3 receive the highest and lowest irradiation, respectively. The activation of bypass diodes under non-uniform illumination conditions segments the P-V curve of a string into N regions, corresponding to the number of diodes. Each of these regions is characterized by a local maximum, creating a challenging multimodal optimization landscape for MPPT controllers. With only one of these points representing the global maximum (GMPP) and the other N-1 being local maxima (LMPPs), conventional tracking methods are prone to suboptimal operation. Therefore, a more sophisticated approach, like a QS-MPPT, is required to model the complex curve and precisely locate the GMPP. As illustrated in Figure 5, the P-V characteristic of a photovoltaic string comprising three modules exhibits the anticipated segmentation under varying irradiance levels, indicative of partial shading. The corresponding performance of the QS-MPPT operating under these conditions is outlined in the pseudo code presented in Figure 6. The system's electrical load is implemented via a resistive element connected to an inverter output terminal (Figure 1). During the initialization phase, the algorithm executes a sampling routine by commanding six discrete duty cycles to the power converter. It acquires the current and voltage measurements at each operating point, derives the power values, and determines the coordinates of the maximum power point (d_{max}, P_{max}). This extremum is assigned as point 4 per the reference diagram. Furthermore, the algorithm defines two auxiliary points (2' and 4') adjacent to the MPP. These are positioned along the power curve between points 3 and 4 and points 4 and 5, respectively, to refine the search domain in the subsequent iteration. The algorithm now possesses five point coordinates (1' to 5', Figure 5) and applies the QS-MPPT method. The maximum point of the approximated function is extracted, and an approximate duty cycle (*D*) is computed using Equation (23). A P&O algorithm (Figure 6) with a reduced step size then converges onto the exact MPP. Index $|P_{mpp}–P_{pv}|$ is defined for the final step; the algorithm continues operating at the identified D_{MPP} while this index remains below its threshold. If the index exceeds its threshold, the process re-initiates to locate a new GMPP. Continuous monitoring of photovoltaic current and voltage detects both sudden and gradual atmospheric transients that impact system performance.

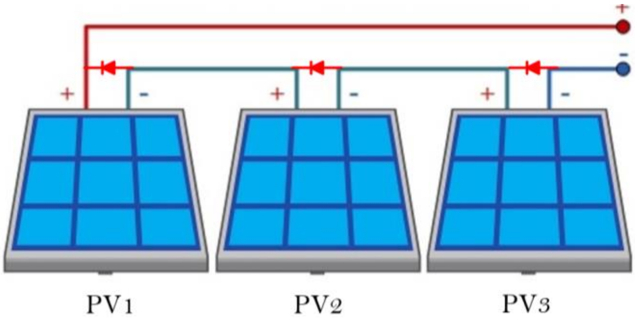

Figure 4. Three modules PV string with bypass diodes.

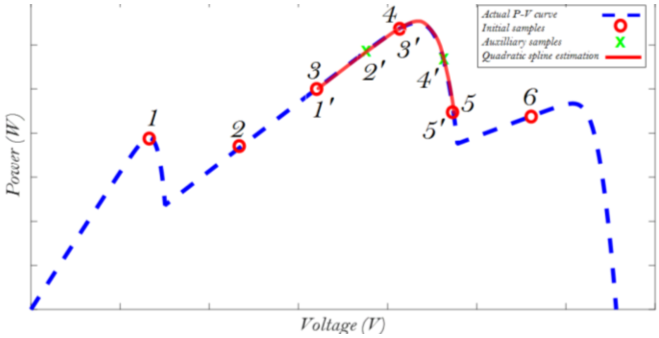

Figure 5. Curve fitting method and MPP estimation based on QS-MPPT method [20].

```
QS-MPPT Pseudo Code
Start
Step 1: Initial Sampling
        1: create an empty set Sprimary
        2: select array Dprimary with six elements
        3: for (each Di in Dprimary) do
        4:     Apply Di to the converter and wait for steady-state.
        5:     Measure corresponding PV voltage Vi and current Ii.
        6:     Calculate power Pi = Vi × Ii.
        7:     Sprimary ⟵ Sprimary ∪ (Di, Vi, Ii, Pi)
        8: end for
– – – – – – – – – – – – – – – – – – – – – – – – – – – – – – – – – – – – – – – – – – – – – – –
Step 2: Identify Initial Maximum Power Point (MPP)
        9: Find the sample with maximum power: (Dmax, Vmax, Imax, Pmax) ⟵ Sprimary(max(P))
– – – – – – – – – – – – – – – – – – – – – – – – – – – – – – – – – – – – – – – – – – – – – –
Step 3: Auxiliary Sampling
        10: Identify the two neighboring duty cycles of Dmax in Sprimary.
        11: create an empty set Sauxiliary
        12: for (each neighbor Dneighbor) do
        13:     Apply a secondary duty cycle D′ (slightly offset from Dneighbor).
        14:     Measure (V ′, I′) and compute P′.
        15:     Sauxiliary ⟵ Sauxiliary ∪ (D′, V ′, I′, P′)
        16: end for
        17: Stotal ⟵ Sprimary ∪ Sauxiliary
        18: Sort Stotal by voltage: Ssorted ⟵ sortV (Stotal)
– – – – – – – – – – – – – – – – – – – – – – – – – – – – – – – – – – – – – – – – – – – – – –
Step 4: Spline Interpolation MPP Estimation
        19: Extract voltage and power arrays: V ⟵ V (Ssorted), P ⟵ P(Ssorted)
        20: Construct a quadratic spline function fspline(V ) interpolating the points (Vj,Pj).
        21: Find the voltage at which fspline(V ) is maximized: V mpp ⟵ V (max(fspline(V )))
        22: Estimate the corresponding power: Pmpp ⟵ fspline(V)
        23: Interpolate to find the duty cycle for Vmpp: Dmpp ⟵ interpolate(Vmpp, Ssorted)
– – – – – – – – – – – – – – – – – – – – – – – – – – – – – – – – – – – – – – – – – – – – – –
Step 5: Local Refinement: Apply a fine-step P&O algorithm
        24: Drefined ⟵ P&O(Dmpp, δ)
– – – – – – – – – – – – – – – – – – – – – – – – – – – – – – – – – – – – – – – – – – – – – –
Step 6: Stability Check & Decision Logic
        25: Apply Drefined to the converter.
        26: Measure new operating point: (Vpv, Ipv), Ppv = Vpv × Ipv
        27: if (|Pmpp − Ppv | < K) then
        28:     Apply Dmpp to the converter.
        29: else if
        30:     Break to top of code in line 1, restarting global search
        31: end if
End
```

Figure 6. QS-MPPT Pseudo Code.

3.3. *Analytical Selection of Sampling Points*

The selection of sampling points is designed to be systematic, rather than based on a pre-known curve. The six initial duty cycles are distributed across a wide, pre-defined range (e.g., from a minimum D_{min} to a maximum D_{max}). This ensures a coarse but comprehensive scan of the entire P-V curve. The goal is not to achieve a specific mathematical condition for the spline at this stage, but to guarantee that at least one sample lies on the curve segment containing the Global Maximum Power Point (GMPP). The auxiliary duty cycles are selected "slightly offset" from the neighbors of the D_{max} point. This densifies the sampling in the most promising region. The Quadratic Spline formulation itself inherently guarantees continuity (continuous first derivative) at the sample points through the enforcement of Equation (9) $\gamma_i = (\beta_{i+1} - \beta_i)/(2h_i)$.

This condition is built into the algorithm's core derivation and is automatically satisfied for any set of sampled points, meaning continuity and differentiability are structural features, not dependent on specific sample positions. Also, over-fitting is typically a concern with high-order polynomials. Use of low-order (quadratic) piecewise polynomials is intrinsically resistant to over-fitting. Each segment only has three coefficients and is defined by local data, preventing it from developing spurious oscillations across the entire curve. The system of equations for solving the coefficients (β_i) is a forward substitution process, Equations (19-22). It does not involve the matrix inversions of higher-order splines, which are prone to ill-conditioning.

3.4. *Sensitivity Analysis ($\partial V_{mpp}/\partial Sample_i$)*

In order to investigate the sensitivity $\partial V_{mpp}/\partial \mathrm{Sample}_i$, the empirical sensitivity of the algorithm is analyzed. The extremum of a quadratic function $C_i(v) = \gamma_i(v - v_i)^2 + \beta_i(v - v_i) + \alpha_i$ is at $v_{extremum} = -\beta_i/(2\gamma_i)$.

The coefficients β_i and γ_i are linear functions of the sampled powers P_i and voltages v_i (from Equations 11, 12, 19-22). Therefore, a perturbation in a sample point will propagate linearly through the coefficient calculations, resulting in a smooth, bounded shift in $v_{extremum}$. The algorithm's robustness to this sensitivity is demonstrated in two ways:

1) Minor errors in the estimated extremum of one quadratic piece are mitigated because the algorithm selects the maximum among all quadratic pieces. An error in a non-global peak is irrelevant.

2) The final fine-step P&O stage acts as a robust corrector, locating the true physical maximum even if the spline-estimated V_{mpp} is slightly off due to sample perturbations or noise.

3.5. *Guarantee of Convergence to the Global Maximum and Robustness to Real-World Imperfections*

The proposed QS-MPPT method does not provide a strict mathematical guarantee of global convergence. Instead, its reliability is derived from a strategic sampling and robust curve-fitting strategy. The algorithm begins by sampling the entire operating range (the PV curve) with a set of six initial duty cycles. This wide-net approach is designed to ensure that at least one sample point lies on or near the curve segment containing the GMPP. The identification of the sample with the highest measured power (P_{max}) anchors the subsequent search in the most promising region. Also, the algorithm then performs auxiliary sampling around the neighbors of P_{max}. This step densifies the data points in the critical region, allowing the quadratic spline to better capture the shape of the most significant peak, including the GMPP. The impact of measurement noise, ADC quantization, and switching ripple is a crucial practical consideration. While the QS-MPPT is not immune to noise, its hybrid structure, combining a robust global estimator (spline) with a precise local tracker (P&O), makes it highly resilient. The spline provides a fast and accurate starting point very near the GMPP, and the P&O compensates for residual errors, ensuring stable and near-optimal operation even in the presence of real-world non-idealities.

3.6. *Stability Management*

The used approach to ensuring stability is based on a time-scale separation and a non-continuous operating mode. The core of stability management lies in the distinct separation between the MPPT decision-making process and the converter's steady-state operation. The QS-MPPT algorithm is not a continuous, high-frequency loop. It is an event-driven process activated only when a significant change in operating conditions is detected (i.e., when $|P_{mpp} - P_{pv}|$ exceeds a threshold K). Between these events, the converter operates at a fixed, steady duty cycle (D_{MPP}).

When holding a constant D, the boost converter with its inner inductor current loop operates as a standard, well-defined system. The stability of this mode is governed by the classic design of the converter's passive components (L, C_{in}, C_{out}) and its feedback compensator. During this prolonged steady state, the system is decoupled from the MPPT logic and is inherently stable. The sampling and proposed quadratic spline-fitting process, while more complex than P&O, is executed only during the brief MPPT event. The STM32 microcontroller has sufficient processing power to complete this calculation within a few switching cycles. This short burst of computation is treated as a transient event, not a continuous delay in a feedback loop.

Parasitic Effects (ESR, Dead Time) are non-idealities that are effectively accounted for by the hybrid P&O refinement step. The spline provides a very accurate voltage reference (V_{mpp}), and the subsequent fine-step P&O adjusts the duty cycle to achieve this voltage on the real converter, automatically compensating for parasitic voltage drops, ESR, and other non-idealities. The P&O step size is chosen to be small enough to converge without causing instability. The stability check in Step 6 of the pseudo-code ($|P_{mpp} - P_{pv}| < K$) acts as a hysteresis band. Once a new D_{MPP} is found and applied, the algorithm will not re-trigger the global search unless the power drift is significant and persistent. This prevents the algorithm from continuously resampling due to minor noise or ripple. The threshold K is set to be substantially larger than the peak-to-peak power ripple caused by switching and noise. Therefore, normal converter operation does not falsely trigger a full MPPT cycle. A resampling event only occurs due to a genuine change in irradiance. Because the system settles into a steady state for long periods, there is no continuous "reset" of the duty cycle. The transition from a fixed D to the sampling sequence and back to a new fixed D is a controlled, discrete event, not a limit cycle.

4. Simulation and PIL Results

In this section, the proposed method is applied to a photovoltaic system (Figure 7) simulated in MATLAB/SIMULINK environment.

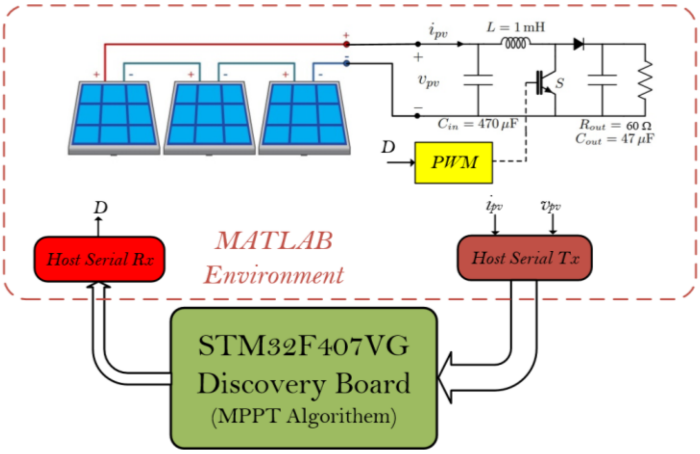

Figure 7. Power circuit and PIL implementation.

In order to investigate the feasibility of laboratory implementation of the proposed power tracking algorithm, it was built on the STM32F407VG Discovery board, which is a widely used microprocessor board [22]. Using the serial communication between this board and the MATLAB/SIMULINK environment in which the power circuit of the solar system is implemented, simulation was performed using the PIL method. As seen in Figure 7, the v_{PV} and i_{PV} quantities are sent as inputs to the processor through the serial port, and after processing these input quantities by the proposed MPPT algorithm implemented on the microprocessor, the duty cycle signal D is generated as an output and sent through the serial port to the power circuit in the MATLAB/SIMULINK environment. The parameters of the circuit are given in Table 1.

The total time required for one full MPPT cycle ($\mathrm{T}_{\mathrm{MPPT}}$) is equal to $\mathrm{T}_{\mathrm{settle}} + \mathrm{T}_{\mathrm{sample}} + \mathrm{T}_{\mathrm{comput}}$. Where:

1. $\mathrm{T}_{\mathrm{settle}}$ (Settling Time): The time for the converter's current/voltage to stabilize after each duty cycle change. This is dictated by the converter dynamics (L, C, load).
2. $\mathrm{T}_{\mathrm{sample}}$ (Sampling Time): $\mathrm{T}_{\mathrm{sample}}$ = (Number of Samples) × $\mathrm{T}_{\mathrm{settle}}$.
3. $\mathrm{T}_{\mathrm{comput}}$ (Computation Time): The time for the microcontroller to execute the spline fitting and maximization. This is negligible relative to $\mathrm{T}_{\mathrm{settle}}$.

The algorithm's "sampling frequency" is the inverse of the $\mathrm{T}_{\mathrm{MPPT}}$ window and not periodic. To accurately track a transient, this $\mathrm{T}_{\mathrm{MPPT}}$ must be shorter than the time constant of the irradiance change. In simulations and PIL tests, with a converter settling time up to ~30ms, a full MPPT cycle with 6 samples completes within 180ms. This is sufficient to track most realistic partial shading transients caused by moving clouds, which typically occur over hundreds of milliseconds to seconds. The algorithm is not designed for sub-cycle transients but for the slower, dominant shifts in the P-V curve's multi-peak structure.

In summary, the sampling strategy is robust by design, leveraging the inherent properties of quadratic splines. While formal sensitivity is a future task, the algorithm demonstrates empirical robustness. The tracking speed is practically sufficient for its intended application, as validated by simulation results.

A detailed switched model consists of three or four series solar cells. Cells are under different irradiation levels. Performance of the proposed method has been assessed in four case studies. At first, the performance of the photovoltaic system under the proposed method was evaluated when three series cell used, and these cells are under different irradiations where the irradiation also has been changed during the system operation. The second case study considered the effectiveness of the proposed method when the converter is supplied with four series solar cells with different irradiation levels. Comparison between the performance of the proposed QS-MPPT with the famous PSO, FPA-based MPPT methods, and P&O is done in the third case study done. Finally PIL implementation results are considered in forth case study.

4.1. *Case study 1: Performance of the PV system supplied with three series cells under different irradiations*

We perform the simulated scenario for two different irradiation patterns. In the first pattern, from time $t=$ 0 to $t=$ 2s, the irradiation levels for PV_1, PV_2, and PV_3 will be 1000, 800, and 600 $[\frac{W}{m^2}]$, respectively at 25 °C. In the next pattern, from time $t=$2s to $t=$4s, the irradiation intensity for PV_3 has been changed from 600 to 400 $[\frac{W}{m^2}]$ while temperature is increased to 45 °C. According to Figure 8, it can be seen that in the first stage, the power 118.87 $[W]$ is accurately tracked with $D=$ %35.06, and at time $t=$ 2s, by changing the irradiation intensity of one of the cells and increasing temperature, the proposed method accurately tracks the power and at time $t=$ 2.24s with $D=$ %57.38, it tracks the final value of 90.21 (Figure 9) $[W]$.

Table 1. Parameters of the power circuit.

Parameter	Value	Description
V_{mp}	17.145 V	For each panel
I_{mp}	3.5 A	
V_{oc}	21.1 V	
I_{sc}	3.8 A	
R_{out}	60 Ω	
L	1 mH	
C_{in}	470 μF	
C_{out}	47 μF	
Switching frequency	20kH	

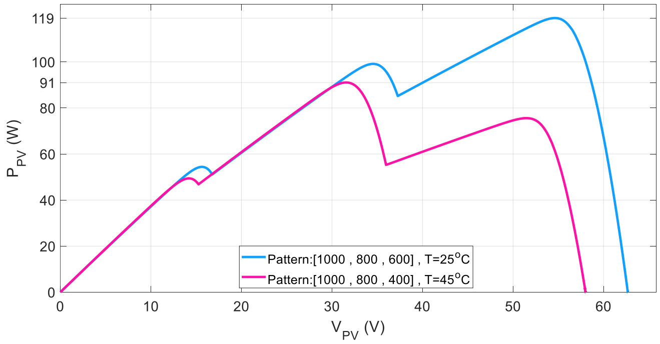

Figure 8. P-V diagram with three different radiations.

4.2. *Case study 2: Performance of the PV system supplied with four series cells under different irradiations*

In the first pattern, from time $t = 0$ to $t = 2s$, the irradiation levels for PV_1, PV_2, PV_3 and PV_4 will be 1000, 800, 600 and 400 $[\frac{W}{m^2}]$, respectively at 25 °C. In the next pattern, from $t = 2s$ to $t = 4s$, the irradiation intensity for PV_4 has been changed from 400 to 700 $[\frac{W}{m^2}]$. Figure 10 gives the P-V curves for both patterns, where for the first pattern $P_{mpp} = 117.543$ $[W]$, and for the second one, the peak is shifted to $P_{mpp} = 159.22$ $[W]$. According to the simulation results in Figure 10 for the first pattern of irradiation at time $t = 0.24s$, the system continues to operate without oscillation with $D_{mpp} = \%35.47$. In this case, $P_{mpp} = 117.13$ $[W]$ at $V_{mpp} = 53.62$ [V] and $I_{mpp} = 2.184$ [A]. At time $t = 2s$, the irradiation pattern changed to the second. In this case, the system follows the maximum power $P_{mpp} = 158.81$ $[W]$, with voltage $V_{mpp} = 72.44$ $[V]$ and current $I_{mpp} = 2.192$ $[A]$, and the duty cycle also continues without oscillation with a constant value of %25.25 at t = 2.24 s (Figure 11).

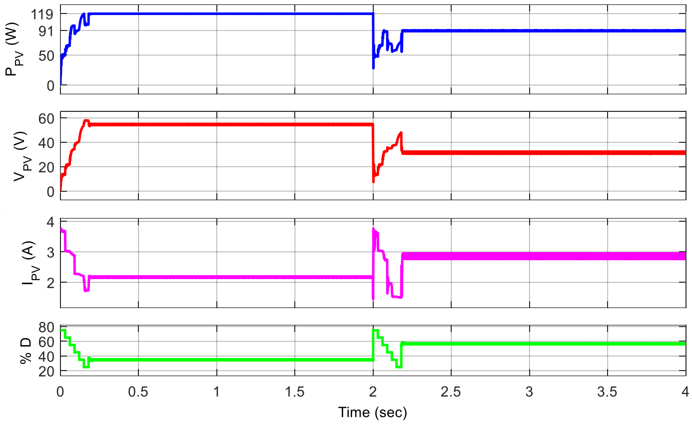

Figure 9. Simulation results under three-cell configuration.

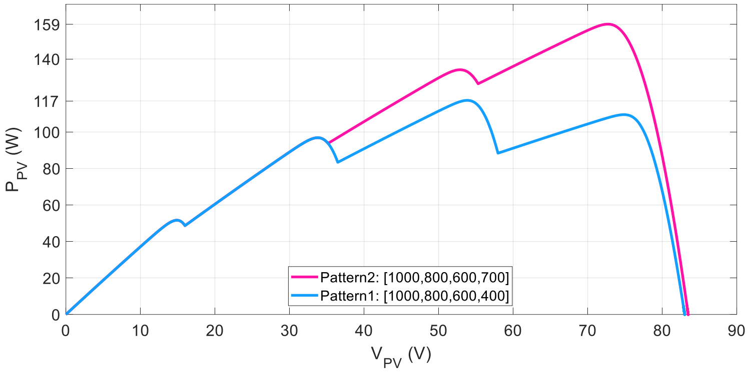

Figure 10. P-V diagram of the four-peak pattern.

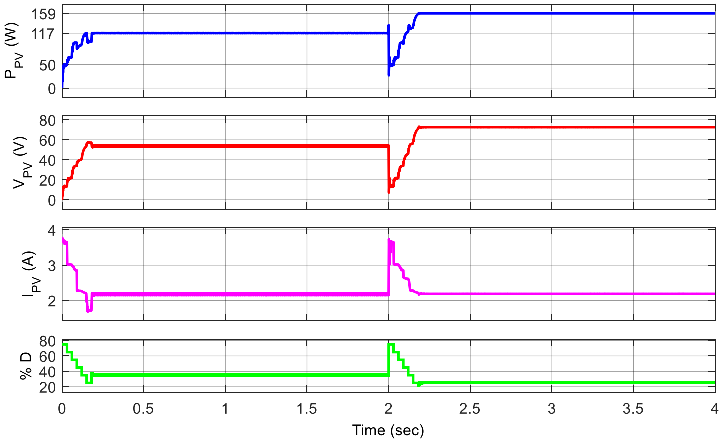

Figure 11. Simulation results under a four-cell configuration.

4.3. Case study 3: Comparing the quadratic-spline method with P&O, FPA, and PSO-based MPPT methods

Proposed QS-MPPT is compared with other MPPT methods, such as FPA, PSO, and P&O, in terms of accuracy and speed of convergence. All algorithms operated on the identical MATLAB/Simulink model of the PV system and power converter. The physical voltage and current bounds were the same for everyone, defined by the PV array's characteristics. In the simulation environment, all methods were subject to the same system dynamics.

Simulation results for the P-V curve shown in Figure 12 are given in Figure 13. Four series modules with irradiation intensities of 1000, 800, 600, and 400 $[\frac{W}{m^2}]$ at 25 °C are connected. As is clear from the P-V curve, the power values at higher peaks are close to each other, and this proximity makes the tracking task difficult. For better comparison, simulation results for all four QS-MPPT, FPA, PSO, and P&O are presented in Table 2. It can be seen that the proposed method performs better than the other methods in terms of accuracy and speed.

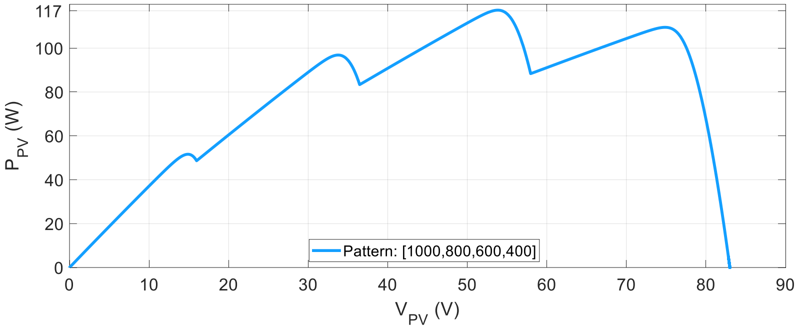

Figure 12. Four-peak diagram under partial irradiation.

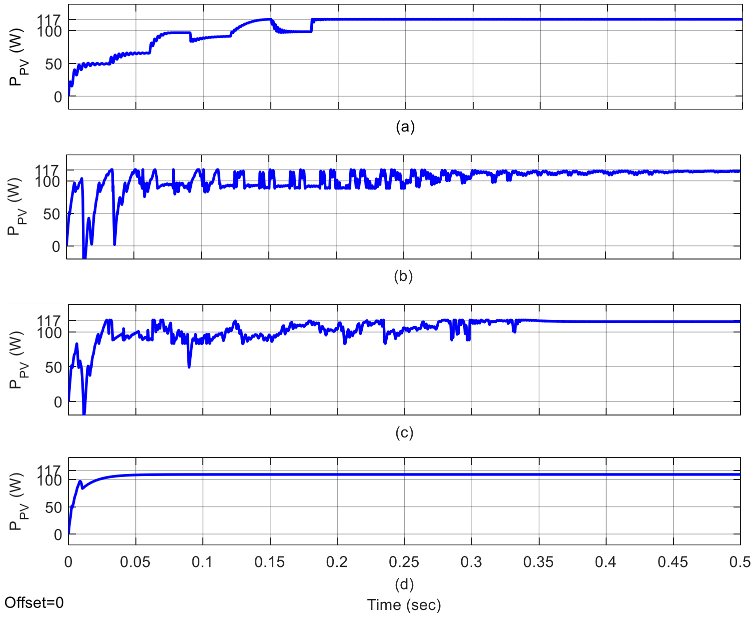

Figure 13. Power, voltage, current, and duty cycle tracking for a four-peak diagram: (a) QS-MPPT, (b) FPA, (c) PSO, and (d) P&O.

Table 2. Simulation results of QS-MPPT, FPA, PSO, and P&O methods.

	GMPP [W]	V_{mpp} [V]	I_{mpp} [A]	d_{mpp}	Tracking time [s]
Actual values	117.558	53.89	2.181	0.358	-
QS-MPPT	117.13	53.65	2.184	0.356	0.16
FPA	115.1	53.62	2.185	0.355	0.45
PSO	114.88	51.82	2.22	0.334	0.35
P&O	109.32	48.94	2.23	0.390	-

4.4. Case study 4: PIL implementation results

To assess the feasibility of implementing the proposed QS-MPPT in a laboratory setting, a PIL simulation was conducted (as shown in Figure 6). The algorithm was deployed on an STM32F407VG Discovery board microcontroller. A serial communication link was established between this hardware target and a MATLAB/Simulink software model, which contained the photovoltaic system's power circuit simulation. Within this PIL framework, the v_{PV} and i_{PV} measurements were transmitted as input parameters to the microprocessor via the serial interface. The embedded MPPT algorithm processed these inputs and computed the corresponding D. This output control signal was then returned serially to the Simulink environment to modulate the simulated power converter. The irradiation patterns at the surface of four series-connected solar cells and their parameters are respectively given in Table 3 and Table 4. Figure 14 shows the P-V curve corresponding to these patterns.

According to Figure 15, it is observed that at time 0.3 seconds, the proposed method tracks the value of 420.17 $[W]$. By changing the irradiation according to the pattern 2 of Table 3, the peak of the maximum power changes, but the algorithm tracks the value 566.237 $[W]$ correctly at $t = 0.6\ s$. Also, the irradiation intensity is changed according to the third pattern of Table 3, and it is observed that the proposed QS-MPPT method has reached the value of 270.208 $[W]$ correctly at $t = 1.2\ s$.

Table 3. Three different patterns for a four-peak photovoltaic system.

	Pattern 1 t=0 to 0.3 s	Pattern 2 t=0.3 to 0.9 s	Pattern 3 t=0.9 to 1.2 s
PV1	1000	1000	1000
PV2	800	800	300
PV3	600	600	600
PV4	400	700	200
P_{max} [W]	421	567	271

Table 4. Parameters of the solar cell used in the PIL implementation.

Parameter	Value	Description
V_{mp}	29 V	For each panel
I_{mp}	7.35 A	
V_{oc}	36.3 V	
I_{sc}	7.84 A	

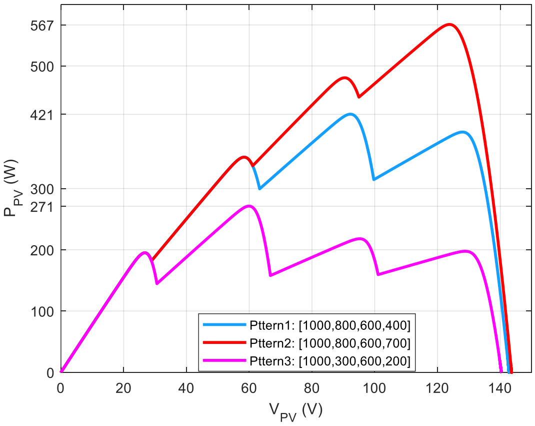

Figure 14. Four-peaked characteristics: pattern 1, pattern 2, and pattern 3.

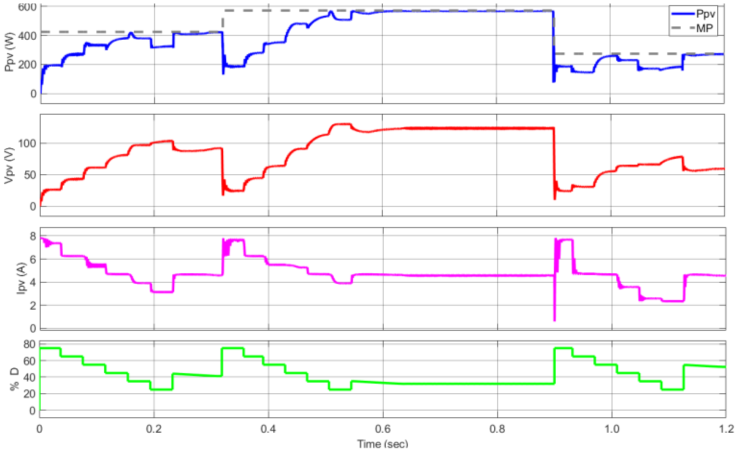

Figure 15. PIL implementation results.

5. Conclusion

In this paper, a novel QS-MPPT technique was introduced to optimize the trade-off between simplicity, accuracy, and processing efficiency. The method utilizes quadratic spline interpolation to generate a simplified, piecewise-representation of the P-V characteristic from a few measurement points, facilitating accurate GMPP estimation without the computational burden of meta-heuristic or cubic-spline alternatives. The technique's efficacy is validated through MATLAB simulations and comparative study against P&O, PSO, and FPA-based MPPT methods, and its hardware implementation viability is proven via PIL testing on an STM32 microcontroller. The results showed that this proposed method, while using simple mathematical relations to process information and find the maximum power point, tracks this point with better speed and accuracy than several other methods.

References

[1] N. D'Souza, L. Lopes, and XueJun Liu, "An Intelligent Maximum Power Point Tracker Using Peak Current Control," *IEEE 36th Conference on Power Electronics Specialists, 2005.*, 172, n.d.

[2] Weidong Xiao, and W. Dunford, "A Modified Adaptive Hill Climbing MPPT Method for Photovoltaic Power Systems," *2004 IEEE 35th Annual Power Electronics Specialists Conference (IEEE Cat. No.04CH37551)*, n.d.

[3] Y. Kim, H. Jo, and D. Kim, "A New Peak Power Tracker for Cost-Effective Photovoltaic Power System," *IECEC 96. Proceedings of the 31st Intersociety Energy Conversion Engineering Conference*, vol. 3, pp. 1673–1678, n.d.

[4] F. Ansari, S. Chatterji, A. Iqbal, and A. Afzal, "Control of MPPT for Photovoltaic Systems Using Advanced Algorithm EPP," *2009 International Conference on Power Systems*, pp. 1–6, 2009.

[5] A. Shemshadi, and H. Haghighi, "Optimal Novel Fuzzy Control Design Method for Efficient Grid-Connected Photovoltaic System," *Journal of Green Energy Research and Innovation*, vol. 2, no. 3, 2025.

[6] M. Mohseni, A. Niknam Kumleh, M. Alibakhshi, and M. Sheikhi Abou Masoudi, "Improving the Maximum Power Point Tracking in a Photovoltaic System Based on the Resistance-Predictive Method," *Journal of Green Energy Research and Innovation*, vol. 1, no. 2, pp. 81–102, 2024.

[7] P. K. Pathak, S. Padmanaban, A. K. Yadav, P. A. Alvi, and B. Khan, "Modified Incremental Conductance MPPT Algorithm for SPV-based Grid-tied and Stand-alone Systems," *IET Generation, Transmission & Distribution*, vol. 16, no. 4, pp. 776–791, 2021.

[8] R. Celikel, M. Yilmaz, and A. Gundogdu, "A Voltage Scanning-Based MPPT Method for PV Power Systems Under Complex Partial Shading Conditions," *Renewable Energy*, vol. 184, pp. 361–373, 2022.

[9] J. P. Ram, D. S. Pillai, A. M. Ghias, and N. Rajasekar, "Performance Enhancement of Solar PV Systems Applying P&O Assisted Flower Pollination Algorithm (FPA)," *Solar Energy*, vol. 199, pp. 214–229, 2020.

[10] S. R. Kiran, C. H. H. Basha, et al., "Reduced Simulative Performance Analysis of Variable Step Size ANN Based MPPT Techniques for Partially Shaded Solar PV Systems," *IEEE Access*, vol. 10, pp. 48875–48889, 2022.

[11] A. R. Nansur, F. D. Murdianto, and A. S. Laili Hermawan, "Improving the Performance of MPPT Coupled Inductor SEPIC Converter Using Flower Pollination Algorithm (FPA) Under Partial Shading Condition," *2018 International Electronics Symposium on Engineering Technology and Applications (IES-ETA)*, pp. 1–7, 2018.

[12] N. Li, M. Mingxuan, et al., "Maximum Power Point Tracking Control Based on Modified ABC Algorithm for Shaded PV System," *2019 AEIT International Conference of Electrical and Electronic Technologies for Automotive (AEIT AUTOMOTIVE)*, pp. 1–5, 2019.

[13] T. Hiyama, and K. Kitabayashi, "Neural Network Based Estimation of Maximum Power Generation from PV Module Using Environmental Information," *IEEE Transactions on Energy Conversion*, vol. 12, no. 3, pp. 241–247, 1997.

[14] K. Sakthivel, R. Krishnasamy, K. Balasubramanian, V. Krishnakumar, and M. Ganesan, "A Revolutionary Partial Resonant Inverter and Doubler Rectifier with MPPT Based on Sliding Mode Controller for Harvesting Solar Photovoltaic Sources," *Sustainable Computing: Informatics and Systems*, vol. 36, 100811, 2022.

[15] B. Yang, S. Wu, et al., "Salp Swarm Optimization Algorithm Based MPPT Design for PV-TEG Hybrid System Under Partial Shading Conditions," *Energy Conversion and Management*, vol. 292, 117410, 2023.

[16] P. K. Pathak, S. Padmanaban, A. K. Yadav, P. A. Alvi, and B. Khan, "Modified Incremental Conductance MPPT Algorithm for SPV-based Grid-tied and Stand-alone Systems," *IET Generation, Transmission & Distribution*, vol. 16, no. 4, pp. 776–791, 2021.

[17] N. R, and G. Sheela K, "Metaheuristic Algorithm Based Maximum Power Point Tracking Technique Combined with One Cycle Control for Solar Photovoltaic Water Pumping Systems," *Frontiers in Energy Research*, vol. 10, 2022.

[18] Anonymous, "A Golden Section Search Assisted Incremental Conductance MPPT Control for PV Fed Water Pump," *International Journal of Renewable Energy Research*, no. Vol12i3, 2022.

[19] T. Noguchi, and H. Matsumoto, "Maximum-Power-Point Tracking Method of Photovoltaic Power System Using Single Transducer," *IECON'03. 29th Annual Conference of the IEEE Industrial Electronics Society (IEEE Cat. No.03CH37468)*, vol. 3, pp. 2350–2355, 2003.

[20] A. Ostadrahimi, and Y. Mahmoud, "Novel Spline-MPPT Technique for Photovoltaic Systems Under Uniform Irradiance and Partial Shading Conditions," *IEEE Transactions on Sustainable Energy*, vol. 12, no. 1, pp. 524–532, 2021.

[21] C. Huang, L. Wang, et al., "A Novel Spline Model Guided Maximum Power Point Tracking Method for Photovoltaic Systems," *IEEE Transactions on Sustainable Energy*, vol. 11, no. 3, pp. 1309–1322, 2020.

[22] L. Yu, H. Wu, F. Yang, J. Jiang, and B. Deng, "Maximum Power Point Tracking (MPPT) Techniques Using Cubic Spline Interpolation – Perturb and Observe (P&O) for Partial Shading Conditions," *2024 International Symposium on Electrical, Electronics and Information Engineering (ISEEIE)*, pp. 500–506, 2024.

[23] M. Seyedmahmoudian, B. Horan, et al., "State of the Art Artificial Intelligence-Based MPPT Techniques for Mitigating Partial Shading Effects on PV Systems – A Review," *Renewable and Sustainable Energy Reviews*, vol. 64, pp. 435–455, 2016.

Declaration of competing interest

The authors declare that they have no known competing financial interests or personal relationships that could have appeared to influence the work reported in this paper. The ethical issues, including plagiarism, informed consent, misconduct, data fabrication and/or falsification, double publication and/or submission, redundancy, have been completely observed by the authors.

Bibliography

Behrooz Shaban was born in Brujerd, Lorestan, Iran. He received the Msc. degree in electrical engineering from Malayer University, Hamedan. He is currently Phd candidate at Tafresh University, Tafresh, Markazi. His research interests include switching power converters, distributed generation, and control.

Email: be.shaban66@gmail.com

ORCID: 0009-0009-8368-1430

Contribution Statement: Conceptualization, Data curation, Formal analysis, Investigation, Methodology, Software, Validation, Roles/Writing - original draft.

Abdolhossein Saleh was born in Nahavand, Hamedan, Iran, in December, 1987. He received the Ph.D. degree in electrical engineering from Bu-Ali Sina University, Hamedan, in 2019. He is currently an Assistant Professor with Malayer University, Malayer, Hamedan. His research interests include power quality, switching power converters, distributed generation, and microgrids and their control.

Email: Hosein.saleh@malayeru.ac.ir

ORCID: 0000-0002-2425-6655

Contribution Statement: Conceptualization, Data curation, Formal analysis, Investigation, Methodology, Resources, Software, Supervision, Validation, Visualization, Roles/Writing-original draft, Writing-review & editing.